Nano-chemo-mechanics of Advanced Materials for Hydrogen Storage and Lithium Battery Applications

A Dissertation

Presented to

The Academic Faculty

By

Shan Huang

In Partial Fulfillment

Of the Requirements for the Degree

Doctor of Philosophy in Mechanical Engineering

Georgia Institute of Technology

December, 2011

Nano-chemo-mechanics of Advanced Materials for Hydrogen Storage and Lithium Battery Applications

Approved by:

Dr. Ting Zhu
G.W.W. School of Mechanical Engineering
Georgia Institute of Technology

Dr. David L. McDowell
G.W.W. School of Mechanical Engineering
School of Material Science and Engineering
Georgia Institute of Technology

Dr. Ken Gall
School of Material Science and Engineering
G.W.W. School of Mechanical Engineering
Georgia Institute of Technology

Dr. Oliver Pierron
G.W.W. School of Mechanical Engineering
Georgia Institute of Technology

Dr. Seung Soon Jang
School of Material Science and Engineering
Georgia Institute of Technology

Date Approved: May 4th, 2011

To my parents,

ACKNOWLEDGEMENTS

First of all, I would like to thank my advisor, Dr. Ting Zhu for his support and guidance during the course of my research at Georgia Tech, and for his tremendous amount of time to shape me as a researcher. He has been a marvelous source of inspiration not only in the academic research but also in discipline of life. I have relished my life and study at Tech., as he gave me complete freedom to carry out my own interests.

I would like to thank Dr. Oliver Pierron and Dr. David L. McDowell for their mentorship in this field of study. I wish to gratefully acknowledge Dr. Seung Soon Jang and Dr. Ken Gall for serving on the reading committee.

I am thankful to Dr. Sulin Zhang at Pennsylvania State University for constantly close collaboration in past four years. I do appreciate the opportunities of working together and having many co-authored papers, from my first publication about silicon nano-fracture to the most recent one about lithiated carbon nanotube. At same time, thanks to Dr. Jianyu Huang at Sandia National Laboratory, and Dr. Ju Li at University of Pennsylvania, for close collaborations and support. Your ideas, experiment results, theoretical analysis and technical support are very important for me to finish this study. I also learned a lot about programming from Dr. Li Ju's masterpieces of codes. Additionally, I would also like to thank Dr. Sachin Terdalkar, whose implementation of reactive field potential enables my MD study on graphene systems.

Special thanks go to my colleagues and friends. Mr. Yuan Zhong, Dr. Honggang Zhou and Dr. Lei Wang helped me a lot since the very beginning of my PhD study. I am also thankful to Mr. Yifan Gao and Ms. Yan Li for selfless sharing of their knowledge about continuum modeling. The daily discussions with Mr. Yifan Gao clarified the puzzles and motivated my studies in anode materials of lithium-ion battery. Additionally, I would like to thank Mr. Sankar Narayanan, Mr. Xu Huang at Pennsylvania State University and Mr. Kejie Zhao at Harvard University, for working together at so many detailed problems. Thanks to Mr. Jin er Song for continuous help in the research and in my personal life. All of you are wonderful friends. I do appreciate the happy time and what I learned from you all.

Last but not least, I am thankful to my parents, Dajian Huang and Shaowei Yao, to my aunt's family, Dr. Shell Huang, Dr. Weiching Yu, for their unconditional love and support. Moreover, thanks to my fiancée, Rulan Gong, she is the constant source of strength to me.

TABLE OF CONTENTS

LIST OF FIGURES

LIST OF TABLES

ABSTRACT

Chemo-mechanics studies the material behavior and phenomena at the interface of mechanics and chemistry. Material failures due to coupled chemo-mechanical effects are serious roadblocks in the development of renewable energy technologies. Among the sources of renewable energies for the mass market, hydrogen and lithium-ion battery are promising candidates due to their high efficiency and easiness of conversion into other types of energy. However, hydrogen will degrade material mechanical properties and lithium insertion can cause electrode failures in battery owing to their high mobilities and strong chemo-mechanical coupling effects. These problems seriously prevent the large-scale applications of these renewable energy sources. In this thesis, the atomistic and continuum modeling are performed to study the chemical-mechanical failures. The objective is to understand the hydrogen embrittlement of grain boundary engineered metals and the lithium insertion-induced fracture in alloy electrodes for lithium-ion batteries.

Hydrogen in metallic containment systems such as high-pressure vessels and pipelines causes the degradation of their mechanical properties that can result in sudden catastrophic fracture. A wide range of hydrogen embrittlement phenomena was attributed to the loss of cohesion of interfaces (between grains, inclusion and matrix, or phases) due to interstitially dissolved hydrogen. Our modeling and simulation of hydrogen embrittlement will address the question of why susceptibility to hydrogen embrittlement in metallic materials can be markedly reduced by grain boundary engineering. Implications of our results for efficient hydrogen storage and transport at high pressures are discussed.

Silicon is one of the most promising anode materials for Li-ion batteries (LIB) because of the highest known theoretical charge capacity. However, Si anodes often suffer from pulverization and capacity fading. This is caused by the large volume changes of Si (~300%) upon Li insertion/extraction close to the theoretical charging/discharging limit. In particular, large incompatible deformation between areas of different Li contents tends to initiate fracture, leading to electro-chemical-mechanical failures of Si electrodes. In order to understand the chemo-mechanical mechanisms, we

begin with the study of basic fracture modes in pure silicon, and then study the diffusion induced deformation and fracture in lithiated Si. Results have implications for increasing battery capacity and reliability.

To improve mechanical stability of LIB anode, failure mechanisms of silicon and coated tin-oxide nanowires have been studied at continuum level. It's shown that anisotropic diffusivity and anisotropic deformation play vital roles in lithiation process. Our predictions of fracture initiation and evolution are verified by *in situ* experiment observations. Due to the mechanical confinement of the coating layers, our study demonstrates that it is possible to simultaneously control the electrochemical reaction rate and the mechanical strain of the electrode materials through carbon or aluminum coating, which opens new avenues of designing better lithium ion batteries.

This thesis addresses the nano-chemo-mechanical failure problems in two green energy-carrier systems toward improving the performance of Li-ion battery anode and hydrogen storage system. It provides an atomistic and continuum modeling framework for the study of chemo-mechanics of advanced materials such as nano-structured metals and alloys. The results help understand the chemical effects of impurities on the mechanical properties of host materials with different metallic and covalent bonding characteristics.

1. INTRODUCTION

Energy is the lifeblood of modern society. Today, the lifestyles of mobility, comfort and prosperity heavily depend on a steady and reliable energy supply from fossil fuel. As the fire marks the dawn of humanity, fossil fuel combustion has been the engine of technological improvement and revolution in the past few centuries. But the price comes along. The excessive emissions of carbon dioxide have driven global climate change. City pollution, finite supplies and global warming conspire to the use of renewable/green energy for the sake of our future generations. Meanwhile, by no means people should take energy security as granted. Manageable risk on reliable energy sources and secured supplement is essential for maintaining stability and prosperity of modern society.

1.1 Energy consumption and sources

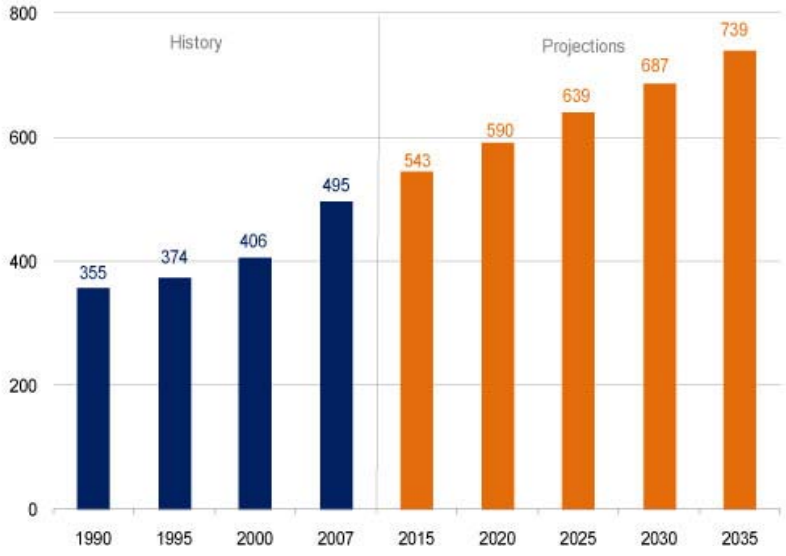

Figure 1. World total energy demand in history and projections (in the unit of quadrillion Btu, and 1 Btu=1055 J). Data source: U.S. Energy Information Administration, international energy outlook 2010.

The consumption of energy had doubled in past 30 years and it would be doubled again in the next 30 years (figure 1) according to the projections from the U.S. Energy Information Administration

(EIA). Meanwhile, the newly advanced economic development in the countries out of Organization for Economic Co-operation and Development (OECD), such as China, Russia and India, will increase the competition in energy sources. Hence, the distribution and classification of energy sources are important.

There are three categories of energy sources. The first one is chemical energy which could be released by chemical reactions. Burning of fossil fuel in internal combustion engine or alcohol burner is the good example of releasing it. The second one is nuclear energy from nuclear reaction, such as fission of heavy nuclei or fusion of light nuclei, where the energy amount is at the level of MeV. The third category is thermal/geological energy, for example, solar energy, wind energy and geothermal energy. Generally, they are renewable and called "green energy". Such green energy sources will meet our future demands for clean, sustainable energy, while they are also limited in time and space.

The green energy sources are widely distributed and plentiful but also diffuse in space and vary in time. There is no solar radiation at night, no wind at certain seasons and no geothermal energy in most areas. To manage energy sources and maintain stable energy supply, efficient energy storage and transportation are necessary to overcome these limits in time and space. By far, hydrogen and lithium-ion battery are two ideal energy carriers with a wide range of perspective applications.

1.2 Hydrogen as renewable, clean and efficient energy carrier

Figure 2. Hydrogen vehicle and hydrogen station on the road.

Hydrogen is a renewable and clean energy carrier, and a promising candidate in future applications. The energy stored in H_2 is chemical energy. Chemical energy is contained in chemical bonds and comes from the bonding effects of valence electrons (i.e., unpaired outer elections). A hydrogen atom, which contains one electron and one proton, has the best ratio of valance electrons

to protons in the whole periodic table. At the same time, the energy gain per election is very high for hydrogen, which leads to a very high energy storage density in unit mass. The energy density of hydrogen, which is 142MJ/kg, is about three times of auto-gas (46 MJ/kg, 60% Propane +40% Butane), and seven times of ethanol/methanol (around 21 MJ/kg) [1]. In addition, hydrogen is one of the most abundant elements on Earth and water is the product of releasing chemical energy in hydrogen through oxidation.

In practice, hydrogen is considered as the ideal fuel to replace gasoline in automobiles. It is lightweight, abundant and oxidized into H_2O, benign to environment. In internal combustion engine, the efficiency of energy transformation for hydrogen-air mixture (~25%) is slightly higher than that of petroleum-air mixture [1]. For a modern commercialized car, it needs to burn 24kg petrol to cover 400km distance but only 8kg pure hydrogen. As a matter of fact, many companies, including BMW, Audi, Ford and Honda, are working to develop and test cars which are powered with hydrogen based fuels (figure 2) [1]. In addition, hydrogen has already been widely used in space technology. Liquid hydrogen is a fuel in the launching process of the Space Shuttle. Both Lockheed military-type aircraft and Tupolev supersonic aircraft have flown with engines fuelled by liquid hydrogen.

1.3 Scientific challenges of hydrogen storage from chemo-mechanics perspective

Along with the promising features of hydrogen in perspective applications, there are many challenges. In real-life applications, efficient hydrogen storage and transportation require pressures under 20~100MPa. Consider hydrogen fuel based vehicle as an example. Eight kilogram hydrogen is about 45m^3 under room temperature and ambient pressure. To compress it to be suitable for a vehicle, with a twenty-gallon tank, the pressure should be above 100MPa. Alternatively, cryotechniques are required for cooling and superinsulated low temperature storage.

Under such high pressure, hydrogen embrittlement becomes a problem. Hydrogen in metallic containment systems such as high-pressure vessels and pipelines causes the degradation of their mechanical properties that can result in sudden catastrophic fracture [2-4]. A wide range of hydrogen embrittlement phenomena is attributed to the loss of cohesion of interfaces (between grains, inclusion and matrix, or phases) due to interstitially dissolved hydrogen [5]. The cohesive strength of

metals could be decreased by hydrogen absorption [6-12]. Besides the effect on decohesion, the change of failure mode may reduce material strength severely. For example, the change from intergranular into transgranular fracture has been observed after charging with hydrogen at high pressures about 20~100MPa [4]. However, due to a lack of fundamental understanding of the chemo-mechanical processes of embrittlement, the hydrogen embrittlement models have not been sufficiently predictive.

Basic research in hydrogen embrittlement needs to focus on understanding the fundamental principles governing bond strength due to hydrogen absorption and migration. The nanostructures of material govern its performance under hydrogen embrittlement. It is necessary to apply these principles to tailor the performance of known storage materials and to identify new materials, which are more suitable for hydrogen transportation and storage under high pressure.

More specifically, the embrittlement effect of hydrogen at interstitial sites has been studied in this research. A method for determining decohesion of grain boundaries by impurities is developed to address two questions: (i) Under given experimental conditions, what is the weakening/strengthening effect of impurities on a given grain boundary? (ii) How does decohesion of grain boundaries cause the change of fracture mode and how to predict it quantitatively? We consider hydrogen in face-centered-cubic (FCC) Ni as a model system, while the approach developed is also applicable to other impurity embrittlement effects, such as carbon in iron.

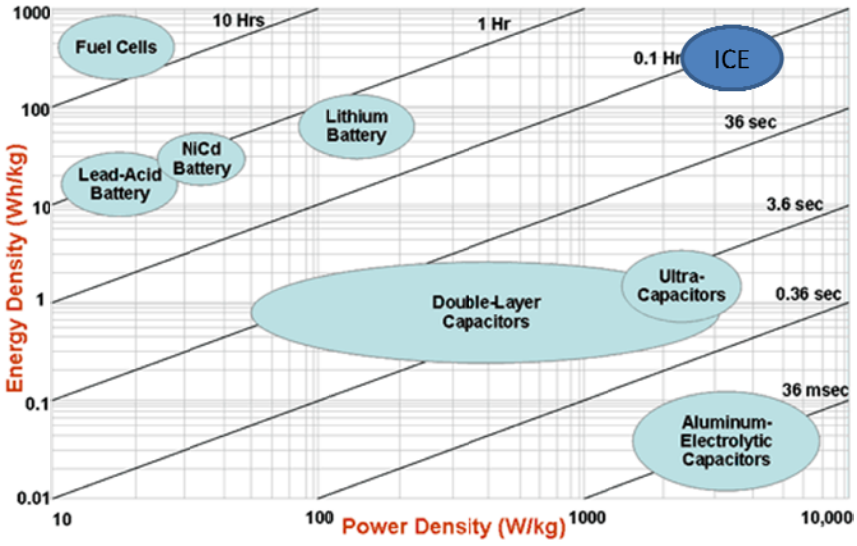

Figure 3. Plot for various energy storage and conversion devices. Source: US Defense Logistics Agency

1.4 Lithium-ion battery with silicon or tin-based anode

Battery can enable efficient energy storage and transportation. Its energy density could be as high as internal combustion engine (ICE) as shown in figure 3. The energy stored in battery is also chemical by nature. Different from burning in ICE, the chemical energy in battery is released electro-chemically. By the second principle of thermodynamics, the efficiency of energy transformation in internal combustion engine is limited by Carnot efficiency. In contrast, by direct transfer of electrons, the efficiency of battery can reach above 50%, which is twice as much as that in thermal processes of ICE.

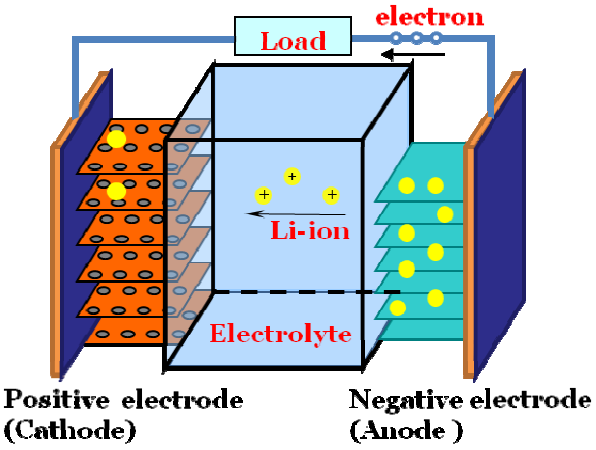

Figure 4. Illustrative structure of lithium-ion battery.

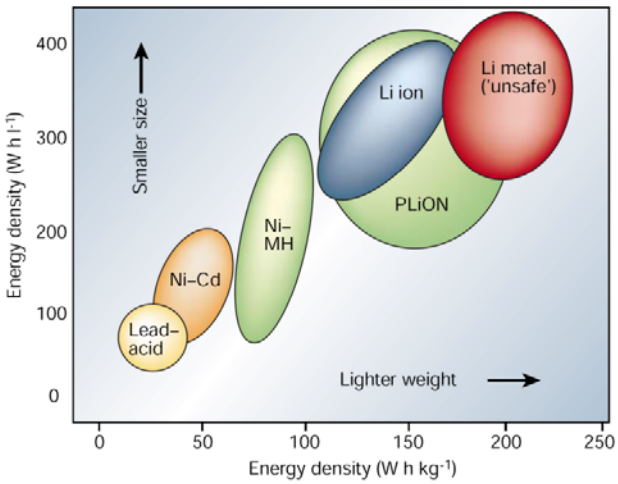

Figure 5. Comparison of different battery technologies [13].

All batteries are composed of two electrodes: positive and negative electrode (cathode and anode) (figure 4). They are connected by electrolyte, which is an ionically conductive material. The chemical potentials of conducting species at two electrodes are different. A circuit forms once the two electrodes are connected by an external electronic conductor. It follows that electrons flow from high potential to low potential for doing work in the external device spontaneously. In rechargeable/secondary batteries, electrons can move in the opposite direction to recharge the battery when a large external voltage is applied to reverse the electron flow.

Lithium-ion battery is a promising candidate in secondary batteries. It has high energy density in term of both unit mass and unit volume (figure 5) [13]. And it has better efficiency, less than half self-discharge compared with nickel-cadmium, and no memory effect. With these advantages, lithium-ion batteries are the most preferred form of electrical energy storage for portable devices. And if the power density could be increased to be comparable with ICE (figure 3), it will be a promising candidate for the potential utilization in all-electric vehicles (EV), while it is being increasingly used for hybrid electric vehicles (HEV) and plug-in HEV (PHEV).

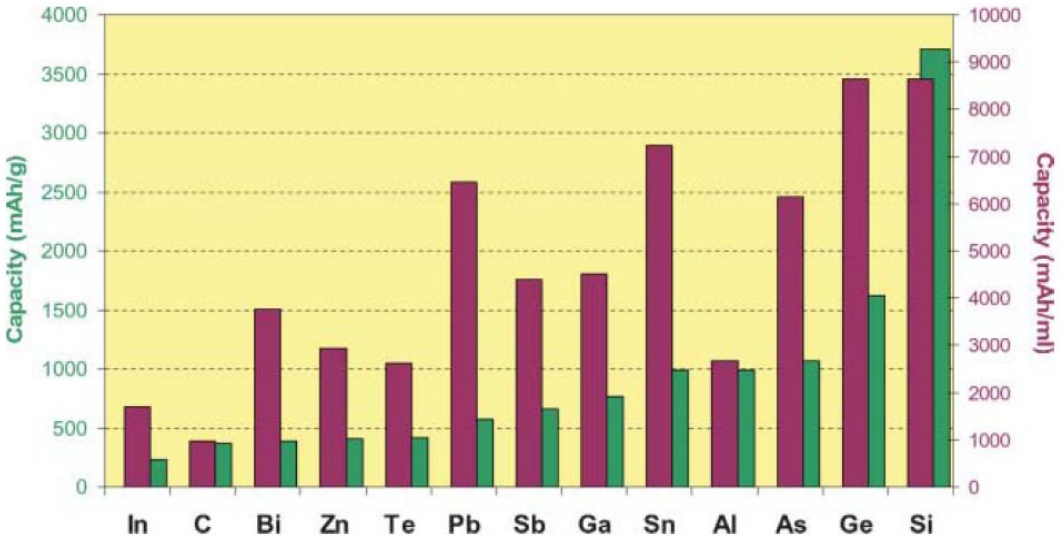

Figure 6. Comparison of capacities of different candidate anode materials [14].

In practice, lithium-ion battery has been widely used in portable electronic devices. Sony has successfully introduced a product called "Nexelion" using a tin-based nano-sized anode material. Panasonic also announced their next generation lithium-ion battery with silicon alloy anode in March 2010. Both of them are using IV element-based material, silicon and tin, as anode in a new generation of Li-ion battery [14]. This is because IV elements have a large capacity in the terms of unit volume and unit mass (figure 6). A significant amount of research has been focusing on graphene, silicon and tin-based material to replace the currently used graphite as negative electrode materials [15]. This thesis research concentrates on these promising materials.

1.5 Scientific challenges of silicon and tin-oxide anode from chemo-mechanics perspective

In recent years, silicon is being intensively studied as a candidate anode material due to its excellent theoretical specific capacity (4200 $mAhg^{-1}$) and volumetric energy density, which are about ten times and twice of corresponding value of graphite respectively. Meanwhile, its structure is amorphous at room temperature. This can efficiently reduce the phase grain boundary strain, which presents a serious problem for crystalline candidates [16], e.g. aluminum and tin. Silicon is less expensive on the molar basis.

During cycles of charging and discharging, silicon and tin-based anodes often suffer from pulverization and capacity fading. This is caused by the large volume changes of material (300% for silicon and 240% for tin-oxide) upon Li insertion/extraction close to the theoretical charging/discharging limit. In particular, large incompatible deformation between areas of different Li contents tends to initiate fracture, leading to electro-chemical-mechanical failures of electrodes.

Improvement is shown by the utilization of nanostructured materials [17-19] in experiments. It has been demonstrated that nanostructured materials could effectively reduce incompatible chemical deformation. Experiments on coated nanowires (NW) show that the coating can increase the mechanical stability of NW, such as carbon NW coated with silicon, tin-oxide NW coated with carbon. Modeling studies are also performed by the density function theory (DFT) method [20-22]. In the case of amorphous nanostructured silicon, since its behavior is the average of all the nanostructures and due to the properties of amorphous states, statistical sampling of structures is required. Due to the time- and length-scale limitations of DFT, intensive calculations for structure sampling are not affordable. The structural revolution during lithiation process is not well understood yet.

More specifically, the task in this part of research is to identify the failure mechanisms of nano-scale anode materials during lithiation. And questions below are answered in this thesis. (i) In the anode materials without lithiation, such as silicon crystal and graphene, what kind of nanoscale fracture mechanisms are involved? What is the thermodynamic and kinetic basis of these mechanisms? (ii) For lithiated material, such as silicon, what are the atomic structure, formation energy and specific volume as a function of lithium concentration? And what is the connection between them? (iii) Basing on the information from atomistic modeling and observations from experiments, how to develop a continuum model to explain experimental observations and to predict when, where and how fracture occurs?

1.6 Objectives

The main goal of the thesis is to quantitatively study nano-chemo-mechanical failure problems in two green energy-carrier systems. They are: (a) hydrogen embrittlement in metals for hydrogen container under high pressures and (b) lithiation induced stress and fracture in anode materials of lithium-ion battery, such as silicon, graphene and tin-oxide. To answer the questions in sections 1.3

and 1.5, multiscale modeling and analysis are performed for both systems. Our results are closely connected with experimental observations. Predictions are given and methods of improvement to avert fracture are discussed.

For hydrogen embrittlement, a continuum thermodynamics formulation of concentration and temperature dependent work of separation is employed. It is the foundation of our study in hydrogen embrittlement. Two thermodynamic limits are considered: fast fracture and slow fracture. The fast fracture limit means that the fracture process is so fast that there is no impurity coming in or going out. The slow fracture limit means that the fracture is so slow that during the fracture, the chemical potential is always in equilibrium with surrounding environments. Then an atomistic characterization method is applied to analyze the hydrogen segregation sites and associated absorption energies at grain boundaries. With atomistically determined structures and energetics, we can evaluate the embrittlement effect of hydrogen on the cohesive strength of grain boundaries under given loading conditions. Finally, a continuum-level analysis is performed to determine the embrittlement effect, such as changing of failure mode from transgranular fracture to intergranular fracture. Hence, all the questions listed in section 1.3 are addressed.

In the problem of Li-ion battery anode failure, we start with pure anode material without charging with lithium. As the first step, we studied the nanoscale fracture process of pristine anode materials, such as silicon crystal and graphene. Then, the lithiation response is modeled by the Molecular Orbital PACkage (MOPAC 2009) with the AM1 method. We calculated the lithium insertion- induced strain using the ring-topological and statistical methods. Properties of amorphous Li_xSi system, such as structure, formation energy and specific volume, and their connections are determined in our atomistic study. This atomistic information can provide a basis of continuum modeling of large incompatible deformation between areas of different Li contents, which tends to initiate fracture, leading to electro-chemical-mechanical failures of electrodes. Finally, continuum models are developed to predict concentration distribution, stress/strain evolution, and fracture of anode materials during lithiation. The combined effect of plastic deformation and two-phase coexistence are studied for the first time, and results provide critical mechanistic insights into the failure mechanisms of large capacity anode materials. Furthermore, coated anode structures, such as tin-oxide coated with carbon and aluminum, are tested and modeled. It has been shown that coated nanowires can enhance electrode conductivity and control radial deformation simultaneously.

1.7 Significant contributions in this research

This thesis research enables the improved understanding of failure mechanisms in two green energy-carrier systems: metallic containment and storage systems for hydrogen and anode materials for lithium-ion battery. The predictive model developed could help the material design and increase the mechanical reliability of systems that may fail due to the coupled chemical-mechanical effects. A deeper understanding of the relationship between material structures and properties could help better utilize advanced materials and avoid their shortcomings in future applications. For example, we could utilize the large capacity of silicon and avert its failure at the same time in lithium ion batteries.

From theoretical perspectives, both covalent and metallic materials are studied in this research. There are treated in a unified theme of the chemo-mechanical effect on material failure mechanisms under either soft or hard chemistry [23]. Hard chemistry refers to the impurity insertion causing dramatic changes in structures and bonding types. It can alter material behaviors significantly. Hence, drastic changes in failure mechanisms are expected, such as the problem of silicon anode failures studied in this thesis. In contrast, soft chemistry refers to the insertion of interstitial impurities with an limited impact on material properties. However, the initial soft-chemistry type of responses may still evolve into catastrophic fracture due to self-catalytic reactions and failures, such as the hydrogen embrittlement problem studied here.

Additionally, our study of hydrogen embrittlement for metallic materials and the failures of lithiated silicon will lay out a framework of linking atomic structure to material property accounting for the coupled chemical and mechanical effects, and explore a less explored interdisciplinary area of chemo-mechanics. In particular, the analysis of electrochemically induced deformation and fracture mechanisms in silicon will be performed through both atomistic and finite element modeling, tightly coupled with experimental measurements. It will present a new paradigm of chemo-mechanical modeling of the advanced materials for energy applications.

1.8 Organization of the thesis

Chapter 2 discusses modeling methods. It includes embedded atom method (EAM) and molecular orbital theory for atomistic modeling, and user controlled diffusion for finite element method (FEM) modeling. A hyperspace exploration method, called activation-relaxation technique (ART), is described and explained by an example. After that a method of characterizing the structure of covalent and metallic materials is discussed. These methods are applied in this thesis research and play a foundational role in the thesis development.

Chapter 3 to chapter 9 can be divided into two parts. The study of two different green energy-carrier systems is presented, respectively. Part one focuses on the metallic containment systems for hydrogen and hydrogen embrittlement effect. Part two focuses on the failure mechanisms of lithiated anode materials, including silicon, graphene and tin oxide. The failure mechanisms of lithiated anode are modeled at both the atomistic and continuum levels.

In chapter 3, an atomistic study is first presented for decohesion of grain boundaries in metals by hydrogen. Then a multi-scale analysis is performed for decohesion induced fractures. After a brief introduction to the thermodynamic framework, the calculation results from molecular statics simulations are presented. Information of electron density is also provided to shed light into the electronic basis of embrittlement. Combining the well-established valve effect and our analysis of local geometry of grains, the transition from transgranular to intergranular fracture is discussed. Our modeling approach is also applicable for impurities in other host systems, such as carbon in iron.

Part two involves chapter 4 to chapter 9. Chapter 4 presents the nanoscale fracture study in pristine silicon and graphene by atomistic modeling. Chapter 5 demonstrates how to tailor system size to avert fracture. Chapter 6 presents the effect of lithiation on amorphous silicon, and discuss properties of amorphous Li_xSi system, including structure, formation energy and specific volume, and their connections. A framework of finite element modeling on lithiated anode material is provided in chapter 7. Two geometries are considered: nano-particle and nano-wire. The application of this framework to silicon nanowires and coated tin-oxide nanowires are given in chapter 8 and 9, respectively. Our model successfully matches experimental results and predicts how fracture initiates and evolves.

Finally, a summary of results and contributions of this thesis are given in chapter 10. It also discusses both the state-of-the-art and future research with regard to new material system and new modeling development.

References

1. **Schlapbach, L. and A. Zuttel, *Hydrogen-storage materials for mobile applications.* Nature, 2001. 414(6861): p. 353-358.**
2. **Myers, S.M., et al., *Hydrogen Interactions with Defects in Crystalline Solids.* Reviews of Modern Physics, 1992. 64(2): p. 559-617.**
3. **Birnbaum, H.K., et al., *Mechanisms of hydrogen related fracture-a review* in *Corrosion Deformation Interactions CDI'96* T. Magnin, Editor. 1997, The Institute of Materials: UK. p. 172-195.**
4. **Bechtle, S., et al., *Grain-boundary engineering markedly reduces susceptibility to intergranular hydrogen embrittlement in metallic materials.* Acta Materialia, 2009. 57(14): p. 4148-4157.**
5. **Rice, J.R., *Hydrogen and Interfacial Cohesion*, in *Effect of Hydrogen on Behavior of Materials*, A.W. Thompson and I.M. Bernstein, Editors. 1976, The Metallurgical Society of AIME: New York. p. 455-466.**
6. **Baskes, M.I. and V. Vitek, *Trapping of Hydrogen and Hellium at Grain-Boundaries in Nickel - An atomistic Study.* Metallurgical Transactions A, 1985. 16(9): p. 1625-1631.**
7. **Mutschele, T. and R. Kirchheim, *SEGREGATION AND DIFFUSION OF HYDROGEN IN GRAIN-BOUNDARIES OF PALLADIUM.* Scripta Metallurgica, 1987. 21(2): p. 135-140.**
8. **Geng, W.T., et al., *Hydrogen-promoted grain boundary embrittlement and vacancy activity in metals: Insights from ab initio total energy calculatons.* Materials Transactions, 2005. 46(4): p. 756-760.**
9. **Van der Ven, A. and G. Ceder, *The thermodynamics of decohesion.* Acta Materialia, 2004. 52(5): p. 1223-1235.**
10. **Jiang, D.E. and E.A. Carter, *First principles assessment of ideal fracture energies of materials with mobile impurities: implications for hydrogen embrittlement of metals.* Acta Materialia, 2004. 52(16): p. 4801-4807.**
11. **Lu, G. and E. Kaxiras, *Hydrogen embrittlement of aluminum: The crucial role of vacancies.* Physical Review Letters, 2005. 94(15): p. 155501.**
12. **Song, J., M. Soare, and W.A. Curtin, *Testing continuum concepts for hydrogen embrittlement in metals using atomistics.* 2009, submitted.**
13. **Tarascon, J.M. and M. Armand, *Issues and challenges facing rechargeable lithium batteries.* Nature, 2001. 414(6861): p. 359-367.**
14. **Larcher, D., et al., *Recent findings and prospects in the field of pure metals as negative electrodes for Li-ion batteries.* Journal of Materials Chemistry, 2007. 17(36): p. 3759-3772.**
15. **Armand, M. and J.M. Tarascon, *Building better batteries.* Nature, 2008. 451(7179): p. 652-657.**
16. **Winter, M. and J.O. Besenhard, *Electrochemical lithiation of tin and tin-based intermetallics and composites.* Electrochimica Acta, 1999. 45(1-2): p. 31-50.**
17. **Magasinski, A., et al., *High-performance lithium-ion anodes using a hierarchical bottom-up approach.* Nature Materials, 2010. 9(4): p. 353-358.**
18. **Cui, L.F., et al., *Crystalline-Amorphous Core-Shell Silicon Nanowires for High Capacity and High Current Battery Electrodes.* Nano Letters, 2009. 9(1): p. 491-495.**
19. **Chan, C.K., et al., *High-performance lithium battery anodes using silicon nanowires.* Nature Nanotechnology, 2008. 3(1): p. 31-35.**
20. **Chevrier, V.L. and J.R. Dahn, *First Principles Studies of Disordered Lithiated Silicon.* Journal of the Electrochemical Society, 2010. 157(4): p. A392-A398.**

21. **Chevrier, V.L., J.W. Zwanziger, and J.R. Dahn, *First principles studies of silicon as a negative electrode material for lithium-ion batteries.* Canadian Journal of Physics, 2009. 87(6): p. 625-632.**
22. **Shenoy, V.B., P. Johari, and Y. Qi, *Elastic softening of amorphous and crystalline Li-Si Phases with increasing Li concentration: A first-principles study.* Journal of Power Sources, 2010. 195(19): p. 6825-6830.**
23. **Huggins, R.A., *Advanced Batteries: Materials Science Aspects.* 2008.**

2. THEORETICAL AND MODELING METHODS

2.1 Molecular dynamics simulation

Molecular dynamics can be classified by the way of describing the interactions between atoms, which is called interatomic potential, or just potential. There are three types of inter-atomic potentials: (a) Empirical potential, such as embedded atom model (EAM); (b) Semi-empirical potential, such as potentials derived from the tight-bonding or molecular orbital theory; and (c) Quantum calculation, such as density functional theory (DFT). The first two are intensively used in this work. Empirical potential is used in the computation of hydrogen embrittlement and simulations of competing fracture mechanisms at crack-tip in silicon and graphene, while lithiation of silicon is modeled by the Molecular Orbital PACkage (MOPAC 2009). Because of the limitation of computational capability, quantum calculation is employed as a method with high accuracy to verify results in this research.

In addition to choices of potentials, two relaxation techniques are available to achieve the objective of simulation: molecular statics (MS) and molecular dynamics (MD). MS merely uses energy minimization principles, such as steepest descent or conjugate gradient, to find the equilibrium state of system. This technique does not simulate the vibration of atoms to characterize the temperature of system. Hence, it is in the energy/enthalpy space and represents the system of interest at 0K. It could not reveal the information that is covered by the noise of temperature. In contrast, MD uses classical mechanics to determine the state of system and the velocities of atoms with finite temperature. The simulation explores in the free energy space and could provide temperature-related information, such as entropy. The limitation of MD on system size is around 100nm and on simulation time is around 100ns. Larger size and/or longer time may not be affordable in terms of computational cost. Because of these limitations, justifications of simulation method and result are necessary, such as diffusivity of heavy atoms, which are usually inferred from energy barriers by transition state theory (TST) instead of evaluating from brutal-force calculation.

To achieve a reasonable balance between the accuracy and efficiency of simulation, a careful selection of interatomic potential and relaxation technique is critical. In this research, embedded

atom model and molecular orbital theory are used. To facilitate discussions in later chapters, a brief introduction to those methods is present here.

2.1.1 Embedded atom model

The embedded atom model (EAM) describes the energy and interatomic forces of the system. The energy is a function of interatomic distances. The EAM formalism is closely related the Finnis-Sinclair model [24-25] developed based on the second moment approximation of tight binding theory. The EAM model is particularly appropriate for the metallic system, whose energy can be effectively represented in terms of the local electron density. In equation (2.1), the potential energy of atom *i*, is given by

$$E_i = F_\alpha\left(\sum_{i\neq j}\rho_\beta(r_{ij})\right)+\frac{1}{2}\sum_{i\neq j}\phi_{\alpha\beta}(r_{ij}) \qquad (2.1)$$

where r_{ij} is the distance between atom *i* and *j*, $\phi_{\alpha\beta}$ is a pair-wise potential function, ρ_β is the contribution to the electron charge density from atom *j* of type β at the location of atom *i*, and *F* is the embedding function that represents the energy of embedding atom *i* into the electron cloud at its position. This description of electron cloud is suitable for metallic interactions, as atoms in metals are considered to embed in the sea of electrons. The EAM potential is also widely used for simulation of alloys, and will be used for studying the problem of hydrogen embrittlement in this thesis. Generally, *F* and $\phi_{\alpha\beta}$ are not often provided in a tabulated form and can be interpolated by spline functions.

In this study, the Ni-H-Al potential developed by Baskes and his coworkers [24] is used to study hydrogen embrittlement. The predictions of many fundamental properties by this potential agree well with experimental measurements and DFT results. Some calibration results are shown in table 2.1.

Table 2.1 Surface energy and binding energy from the EAM potential of Ni-H [25]. They are consistent with values from experimental measurements.

	EAM	Experiment
Molecular binding energy	-2.37	-2.4
Bulk: tetrahedron	-1.79	-2.05
octahedron	-2.20	
(111) surface: top	-2.62	-2.70
three-fold	-2.71	

2.1.2 Molecular orbital theory modeling

Molecular orbital theory is a semi-empirical quantum chemistry method for determining the structure and energy of a molecular system. In this theory, each molecule has a set of molecular orbital, and the molecular orbital wave function ψ_j can be written as a simple weighted sum of the n constituent atomic orbitals χ_i, according to the following equation:

$$\psi_j = \sum_{i=1}^{n} c_{ij}\chi_i \qquad (2.2)$$

MOPAC is a commercial software for molecular orbital theory calculation. Its latest potential library includes about 7600 chemical species. MOPAC performs semi-empirical calculations, much faster than their *ab initio* counterparts. It has been shown to have high accuracy in the recent PM6 models [26]. It also supports several input and visualization formats.

MOPAC with the PM6 method is one of the best choices to study the lithiation for battery materials. It enables efficient computation with semi-empirical quantum description of molecular interactions. In the lithiation problem, although atomic species involved are relatively simple (only silicon and lithium), the bonding environment of atoms changes from covalent to ionic as lithium atoms are inserted into silicon. This requires an accurate calculation of electron transfer [20]. MOPAC was developed based on the molecular orbital theory that can provide the required accuracy. Meanwhile, the study of amorphous structures and the associated mechanical properties requires intensive calculations. Namely, statistical sampling of structures is necessary to model the amorphous

state, and the simulated system must be large enough to mitigate the size effect on the predicted mechanical properties. Compared to the *ab initio* approach, MOPAC is more computationally efficient for large systems and intensive calculations. It makes possible the simulations of several hundred silicon-lithium atoms by a single CPU.

2.2 Activation relaxation technique (ART)

In many material systems, the dynamics can be described as transitions across a sequence of meta-stable states and energy barriers in between. These energy barriers can be so high that, in MD simulations, the time required to sample these states is much longer than the time scale of lattice vibration, which is on the order of femto second. In other words, it takes a lot of trials and a long time for the system to jump out of the local minimums. As a result, most of the computational time is spent on atomic vibrations that are of little interest for the long-time dynamics simulations. The accelerated dynamics simulation is, therefore, highly desired. In general, this can be achieved by applying high temperature and/or high stress or strain rate. However, these approaches can drastically change the system responses relative to the slow dynamic processes at long time scales. In this thesis, a highly efficient method, activation-relaxation technique (ART), will be used to generate the amorphous structure structures efficiently.

Implementation of the ART consists of two steps: displacing the system from a local energy minimum to a nearby saddle point (the part of activation), and relaxing it from the saddle point to a new minimum (the part of relaxation) [27]. ART only spends time simulating the activated events of escaping the basins in the energy landscape, i.e., jumping over the barriers that separate different local energy minima. It does not waste time on simulating vibrations of atoms around their local equilibrium positions. Compared with the conventional acceleration method by high temperature, ART can avoid the bias on structural evolution caused by, e.g., fast melt and quench [22, 28].

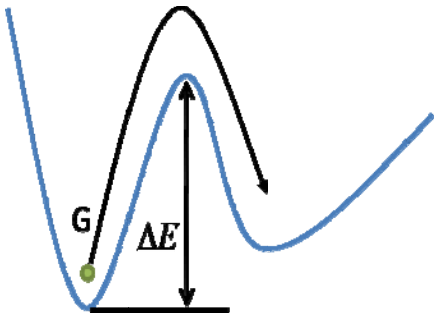

Figure 2.1. Following modified force filed G, system can overcome energy barrier ΔE to achieve a new stable state. The acceptance ratio of such overcoming depends on the energy difference of two states.

The ART relies on one important assumption: the direction of the minimum energy path (MEP) at a saddle point and the direction towards the original local minimum have an overlap, i.e. there exists a non-zero dot product between them. If this assumption holds, a modified force field $\vec{G}$ will lead us to a saddle point:

$$\vec{G} = \vec{F} - \left[1 - \frac{\alpha}{1 + \Delta x}\right](\vec{F} \cdot \overrightarrow{\Delta x})\overrightarrow{\Delta x} \qquad (2.3)$$

In equation (2.3), $\vec{F}$ is a 3*N*-dimensional force vector, *N* is the number of atoms and $\overrightarrow{\Delta x}$ is the displacement vector from the previous minimum. α is a parameter to help the convergence to the saddle point, and it is recommended to be taken as 0.15 in producing structures of amorphous silicon. As soon as the component of $\vec{F}$ in the direction of $\overrightarrow{\Delta x}$ changes sign, we know that the saddle point is just passed and an event has happened. Then one can turn off $\vec{G}$ and use $\vec{F}$ to perform energy minimization or MD for achieving a new energy-minimum state.

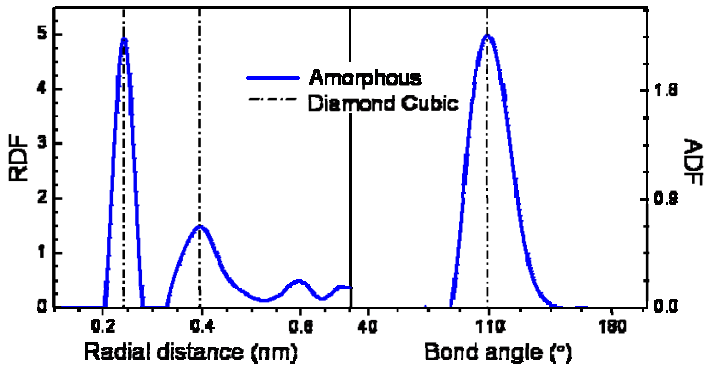

Figure 2.2. Smoothed radial distribution function and angular distribution function of ART-generated amorphous silicon structures. They are the same as those obtained from the melt-and-quench methods from previous work [29].

After a new stable state is achieved, the energy of this state is calculated. If ΔF is the energy difference between the new state and the old state, the probability of accepting the new stable state is $\min\left(\exp\left(-\frac{\Delta F}{k_B T}\right), 1\right)$. This step is equivalent to a step in Markov chain Monte Carlo (MCMC), where aperiodicity, irreducibility and reversibility are embedded automatically according to the ergodic theory. Therefore, ART inherits the properties of MCMC, such as initial state independence and fast convergence to target distribution. In the practical use of Markov chain methods, the standard simulation methodology provides several variance reduction techniques and also gives guidance on the choice of sample size and allocation.

The amorphous silicon structures are needed for the study of lithiated silicon in this research. They are generated by activation-relaxation technique (ART) [27] with crystal phase as an initial state. To speed up calculations, *a*-Si structures were first created by using the empirical Stillinger-Weber [30] interatomic potential and then further relaxed by MOPAC. Figures 2.2 show the radial distribution function and angle distribution function of amorphous silicon that we created, consistent with previous results [29, 31-32].

2.2 Stress and diffusion coupling

Stress can strongly couple with diffusion, such as stress-mediated defect migration [33-34], oxidation [35-36], and lithiation [37-39]. On one hand, reactions with impurities change the mechanical properties of material, and induce chemical growth strain and mechanical accommodation strain, which cause the buildup of stress. On the other hand, stress can accelerate or decelerate diffusion and reaction of impurities. The stress-diffusion coupling can significantly increase the complexity of the problem.

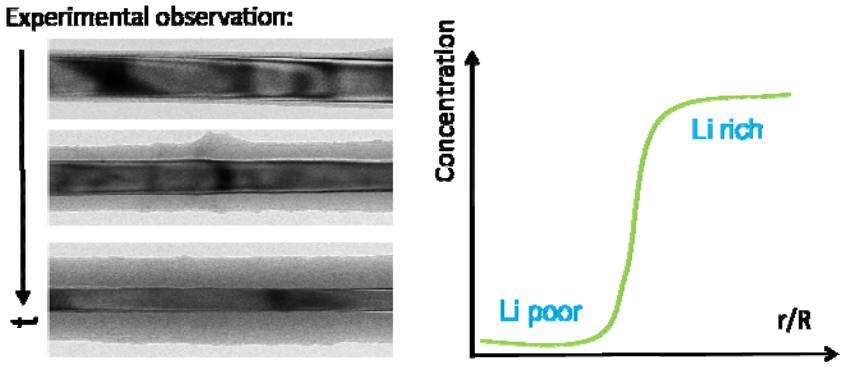

Figure 2.3. Lithium-rich and lithium-poor phases observed in experiments.

Our study of stress–diffusion coupling is motivated by experimental observations. In recent *in-situ* experiments of lithiation of single nanowire electrode, both lithium-rich and lithium-poor phases are observed (figure 2.3). The coexistence of these two phases implies a double-well form of the free energy governing the development of the two phases. To enable a direct appreciation of the key concepts, one may consider the free energy function of the well-known regular solution model:

$$E = (1-c)f^{Si}(T) + cf^{LixSi}(T) + RT[clnc + (1-c)\ln(1-c)] + Wc(1-c) + F\phi \qquad (2.4)$$

$f^{Si}(T)$ and $f^{LixSi}(T)$ are the specific free energy of pure silicon and fully lithiated silicon, respectively, W characterizes the non-ideal interaction of between solute (e.g., lithium) and solvent (e.g, silicon). From the definition of chemical potential

$$\mu = \frac{\partial E}{\partial c} \qquad (2.5)$$

and the conservation law of diffusion

$$\frac{\partial c}{\partial t} = -\frac{\partial \vec{J}}{\partial \vec{x}} \qquad (2.6)$$

one can readily obtain the relationship between flux rate and local concentration

$$\vec{J} = -\frac{CD_0}{RT}\frac{\partial \mu}{\partial \vec{x}}$$

$$= -D_0\left[\frac{1}{1-c} - \frac{2Wc}{RT}\right]\frac{\partial c}{\partial \vec{x}} \qquad (2.7)$$

In equation (2.7), D_0 is a function of local stress states which is caused by deformation, while deformation is proportional to local concentration *c*. This coupled deformation-diffusion relationship significantly increases the complexity of the problem, requiring an effective control on diffusivity in our simulations.

User defined subroutines in ABAQUS provide a handy solution. Basing on the analogy between heat transfer and diffusion, we use heat transfer (UMATHT) to model diffusion. Generally, the UMATHT can be programmed to control diffusivity as a function of local concentration. Combined with the user-defined field subroutine, USLFD, the stress and strain could be passed into UMATHT. As such, the diffusivity can be controlled as a function of stress and strain. Meanwhile, the diffusion induced deformation is also a function of local concentration, which could be controlled in UEXPAN. Hence, with the three user subroutines described above, the diffusion and deformation can be coupled in simulations. This coupling is essential to the continuum modeling of the Lithiation and deformation of electrode materials for lithium ion battery.

2.3 Characterization of grain boundary in metals and atomic structure in amorphous silicon

Characterization of material structure is vital to the understanding of its mechanical behaviors. Different methods need to be used for metallic and covalent materials. Atoms near the grain boundary of metals and those in the amorphous silicon do not have periodic arrangement as in crystals. However, both of them can be viewed as the random packing of spheres, and how they are packed is dependent on the nature of atomic bonding, such as covalent bonding in silicon. Methods of

characterizing the glassy structures of face-centered-cubic (FCC) metal and diamond cubic silicon are presented in following sections.

2.3.1 Deltahedral packing units of grain boundary in metals

In metals, atoms are closely packed for achieving local maximal electron density. The structure of close packed atoms can be characterized by polyhedra [40-41]. For example, one can construct FCC lattice by using tetrahedron and octahedron (figure 2.4). As shown by Ma et al [42], bulk metallic glass (BMG) can be similarly characterized in terms of polyhedron. Because of the similarity between BMG and grain boundary, we use deltahedron [40-41], through Voronoi tessellation [42], as a tool for structural characterization of grain boundaries in metals. A deltahedron is a polyhedron whose faces are all equilateral triangles. As shown in figure 2.5 (left), deltahedra can be classified by the number of its vertices. For example, a Σ5 grain boundary in FCC metal (figure 2.5 right) consists of a combination of bi-tetrahedron, pentagonal bi-pyramid and capped trigonal prism. Different grain boundaries have different combinations of deltahedra. Besides the Σ5 [001], three other grain boundaries are analyzed in chapter 3, including Σ17 [001] , Σ11 [011] and Σ27 [011]. Deltahedra provide an effective means of evaluating the physical properties, such as free volume, adsorption energy and surface energy. The impurities embrittlement effect on grain boundaries can be calculated based on these properties. Analysis of the combined effects of deltahedral units at grain boundaries could directly provide information of impurity effect on cohesive strength relevant to experimental conditions. Characterization of grain boundary structure is an essential part of our hydrogen embrittlement model.

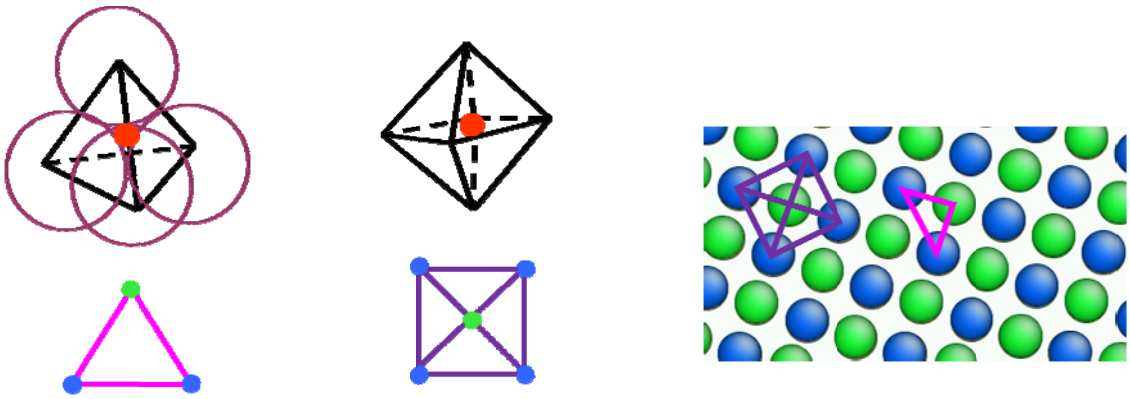

Figure 2.4. The structure of an FCC metal involves the periodic packing of tetrahedron (pink triangle) and octahedron (purple square).

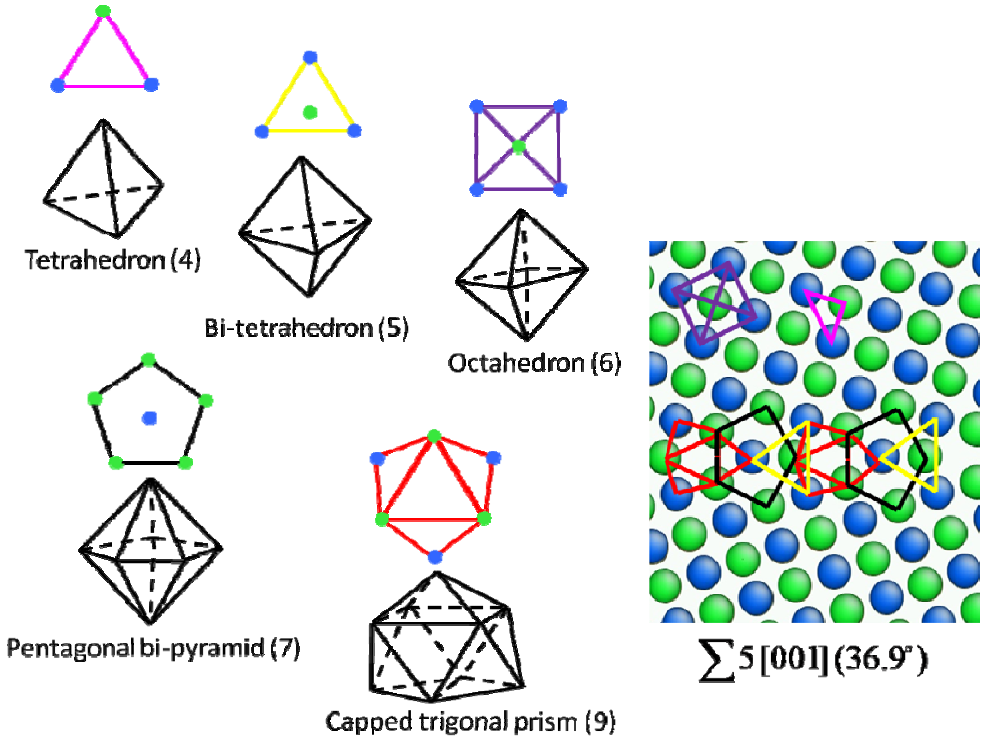

Figure 2.5. (Left) Deltahedra with 4, 5, 6, 7 and 9 vertexes. (Right) the structure of a Σ5 grain boundary can be decomposed as a combination of different deltahedra with a short period (about 1nm).

2.3.2 Shortest-path ring and statistics in amorphous silicon

In contrast to metals, the atoms in silicon are directionally and covalently bonded, forming an open network structure. One unique feature of the network structure is the ring, which can be considered as the basic structural unit of silicon. A simple and unambiguous definition of the shortest-path (SP) ring has been introduced in a previous study [43]. The statistics of rings [44] is a powerful tool for characterizing the structure of amorphous silicon.

According to [43] and [44], a SP ring is defined as a ring where the path between any two nodes is one of the shortest possible paths in the graph. More specifically, a SP ring can be defined as follows: Define a measure Dist(x,y) in a graph, which measures the shortest distance from node x to node y. Hence, we have Dist(x,y)= Dist(y,x) in a two-way graph. Then we call a ring R is a SP ring in graph G, if and only if any two nodes x and y in R satisfy equation (2.8).

$$Dist_R(x, y) = Dist_G(x, y) \qquad (2.8).$$

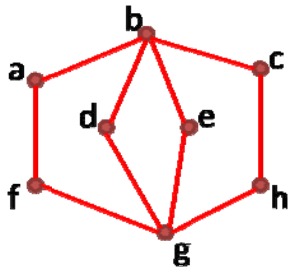

Figure 2.6. An illustrative 2D graph with 3 SP rings, which are *a-b-d-g-f-a (or a-b-e-g-f-a), b-e-g-d-b, and b-c-h-g-e-b*. A 3D graph will be more complicated but the definition and algorithm of identify SP ring are the same.

Three challenges exist in evaluating the ring statistics: (i) recognize a ring structure; (ii) distinguish SP rings; and (iii) record replicas. For example, in figure 2.6, there are three SP rings: *a-b-d-g-f-a, b-e-g-d-b, and b-c-h-g-e-b*. All other rings are not SP rings, while SP ring *a-b-e-g-f-a* is a replica of *a-b-d-g-f-a*. They have the same length, which is 5 and satisfies equation (2.8). To overcome these challenges, we implement Dijkstra's shortest path algorithm [45], which is more efficient than the stacking method introduced in ref [43]. The main procedures are as follows:

1. **Select an (arbitrary) vertex *x***

2. **Generate each ring containing *x***

   2a) Select a pair of neighbors of x: (*y, z*)

   2b) Find the shortest path from *y* to *z* (Using Dijkstra's Shortest Path Algorithm)

   2c) Check alternative shortest path

   2d) Verify the ring is SP ring

3. **Delete vertex *x* from the graph**

4. **Repeat 1-3 until only 2 vertices left**

More specifically, in the previous example, the program follows 4 steps: Step1. Select a vertex *a*; Step2. 2a) Select a pair of neighbors (*b,f*), 2b) Find the shortest path *b-d-g-f*, 2c) Find alternative path *b-e-g-f*, 2d) Verify the rings are SP ring; Step3. Delete vertex *a* from the graph; Step4. Repeat 1-3 until only 2 vertices left, which will be *h* and *g*.

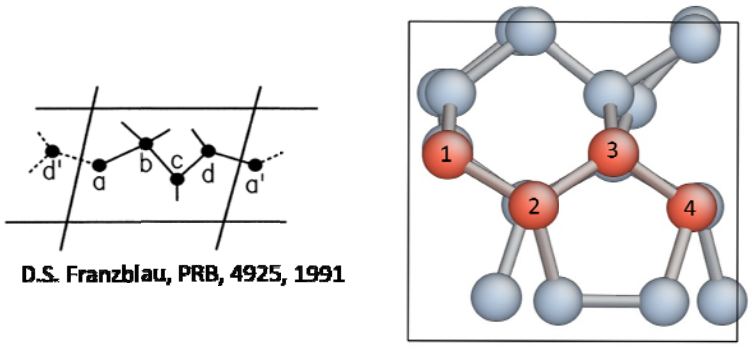

Figure 2.7. Chain problem conceptually proposed by Franzblau (1991) [43] (left) and in a real amorphous silicon structure (right).

Find a "chain" problem during the application of ring statistics in the case study. When the periodic boundary condition is used and if the system is too small, the program may mistakenly treat a chain of atoms as a ring. For example, in the left part of figure 2.7, due to periodic boundary conditions, atom *a* is the same as atom *a'* and atom *d* is the same as atom *d'*. Atom *a* is connected with atom *d*. Hence,

the program may consider a-b-c-d-a as a SP ring. In a real silicon structure (figure 2.7 right), the program may consider 1-2-3-4-1 as a SP ring. A simple solution to this "chain" problem is to increase the system size. In our analysis of amorphous silicon, duplicated super-cells are used so that each side is larger than 30 Å. Additionally, the upper-limit of ring size is set as 10 in protocol step 2. These two numbers (30 Å and 10) are adopted basing on a simple analysis of amorphous silicon: Firstly, we never identify a ring whose size is bigger than 9, because its formation energy will be so high that it is unlikely to exist. Secondly, the distance between two bonded silicon atoms is always smaller than 2.8Å. Hence in silicon, the path length of a SP ring is always smaller than 30 Å. Therefore, we can essentially prevent the "chain" problem if the size of the supercell is larger than the path length of the largest ring.

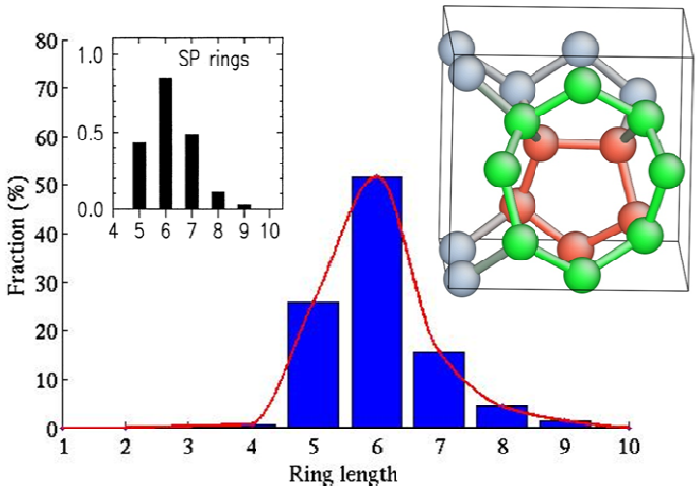

Figure 2.8. Atomic structure of amorphous silicon is characterized by the shortest-path rings (SP rings). The rings are defined by the number of bonds involved and these bonds are shared by adjacent rings.

The change in the ring statistics during structural evolution implies a variation in the material properties [43-44]. The SP rings in amorphous silicon are counted and shown in figure 2.8. The more the small rings, the less open the network structure. In contrast, the more the large rings, the less dense the silicon atoms are packed. In figure 2.8, there is a single peak in the distribution of ring

statistics, corroding to a ring size of 6. This is consistent with that of the silicon crystal, where the ring distribution is a delta function, as shown in [43] (black-white sub-figure in the top left). As will be described in chapter 6, counting the ring sizes enable the tracking of the evolution of amorphous structures, and the open space in silicon decreases significantly along with the insertion of lithium atom.

References

1. **Baskes, M.I., *MODIFIED EMBEDDED-ATOM POTENTIALS FOR CUBIC MATERIALS AND IMPURITIES.* Physical Review B, 1992. 46(5): p. 2727-2742.**
2. **Daw, M.S. and M.I. Baskes, *EMBEDDED-ATOM METHOD - DERIVATION AND APPLICATION TO IMPURITIES, SURFACES, AND OTHER DEFECTS IN METALS.* Physical Review B, 1984. 29(12): p. 6443-6453.**
3. **Stewart, J.J.P., *Optimization of parameters for semiempirical methods V: Modification of NDDO approximations and application to 70 elements.* Journal of Molecular Modeling, 2007. 13(12): p. 1173-1213.**
4. **Chevrier, V.L. and J.R. Dahn, *First Principles Studies of Disordered Lithiated Silicon.* Journal of the Electrochemical Society, 2010. 157(4): p. A392-A398.**
5. **Barkema, G.T. and N. Mousseau, *Event-based relaxation of continuous disordered systems.* Physical Review Letters, 1996. 77(21): p. 4358-4361.**
6. **Vanderbilt, D., X.Y. Zhao, and D. Ceresoli, *Structural and dielectric properties of crystalline and amorphous ZrO2.* Thin Solid Films, 2005. 486(1-2): p. 125-128.**
7. **Shenoy, V.B., P. Johari, and Y. Qi, *Elastic softening of amorphous and crystalline Li-Si Phases with increasing Li concentration: A first-principles study.* Journal of Power Sources, 2010. 195(19): p. 6825-6830.**
8. **Stillinger, F.H. and T.A. Weber, *Computer-simulation of local order in condensed phases of silicon.* Physical Review B, 1985. 31(8): p. 5262-5271.**
9. **Demkowicz, M.J. and A.S. Argon, *High-density liquidlike component facilitates plastic flow in a model amorphous silicon system.* Physical Review Letters, 2004. 93(2): p. 4.**
10. **Demkowicz, M.J. and A.S. Argon, *Liquidlike atomic environments act as plasticity carriers in amorphous silicon.* Physical Review B, 2005. 72(24).**
11. **Demkowicz, M.J. and A.S. Argon, *Autocatalytic avalanches of unit inelastic shearing events are the mechanism of plastic deformation in amorphous silicon.* Physical Review B, 2005. 72(24).**
12. **Swaminathan, N. and J. Qu, *Interactions between non-stoichiometric stresses and defect transport in a tubular electrolyte.* Fuel Cells, 2007. 7(6): p. 453-462.**
13. **Swaminathan, N. and J. Qu, *Evaluation of thermomechanical properties of non-stoichiometric gadolinium doped ceria using atomistic simulations.* Modelling and Simulation in Materials Science and Engineering, 2009. 17(4).**
14. **Zhou, H.G., J.M. Qu, and M. Cherkaoui, *Finite element analysis of oxidation induced metal depletion at oxide-metal interface.* Computational Materials Science, 2010. 48(4): p. 842-847.**
15. **Zhou, H.G., J.M. Qu, and M. Cherkaoui, *Stress-oxidation interaction in selective oxidation of Cr-Fe alloys.* Mechanics of Materials, 2010. 42(1): p. 63-71.**
16. **Gao, Y.F. and M. Zhou, *Strong stress-enhanced diffusion in amorphous lithium alloy nanowire electrodes.* Journal of Applied Physics, 2011. 109(1).**
17. **Christensen, J. and J. Newman, *Stress generation and fracture in lithium insertion materials.* Journal of Solid State Electrochemistry, 2006. 10(5): p. 293-319.**
18. **Cheng, Y.-T. and M.W. Verbrugge, *The influence of surface mechanics on diffusion induced stresses within spherical nanoparticles.* Journal of Applied Physics, 2008. 104(8): p. 083521.**
19. **Ashby, M.F. and F. Spaepen, *NEW MODEL FOR STRUCTURE OF GRAIN-BOUNDARIES - PACKING OF POLYHEDRA.* Scripta Metallurgica, 1978. 12(2): p. 193-195.**
20. **Ashby, M.F., F. Spaepen, and S. Williams, *Structure of Grain-Boundaries Described as a Packing of Polyhedra.* Acta Metallurgica, 1978. 26(11): p. 1647-1663.**

21. **Sheng, H.W., et al.,** ***Atomic packing and short-to-medium-range order in metallic glasses.*** **Nature, 2006. 439(7075): p. 419-425.**
22. **Franzblau, D.S.,** ***COMPUTATION OF RING STATISTICS FOR NETWORK MODELS OF SOLIDS.*** **Physical Review B, 1991. 44(10): p. 4925-4930.**
23. **Huang, S. and T. Zhu,** ***Atomistic mechanisms of lithium insertion in amorphous silicon.*** **Journal of Power Sources, 2011. 196(7): p. 3664-3668.**
24. **Dijkstra, E.W.,** ***A note on two problems in connexion with graphs.*** **Numerische Mathematik, 1959. 1: p. 269-271.**

3. HYDROGEN EMBRITTLEMENT IN METALS

3.1 Introduction

Challenges associated with a hydrogen economy are substantial, ranging from hydrogen generation, storage, and transportation [1]. Hydrogen in metallic containment systems such as high-pressure vessels and pipelines can cause the degradation of their mechanical properties that can further result in the sudden and unexpected catastrophic fracture [2-4]. A wide range of hydrogen embrittlement phenomena was attributed to the loss of cohesion of interfaces (between grains, inclusion and matrix, or phases) due to interstitially dissolved hydrogen [5]. This concept and related models [6-8], however, have not been made sufficiently predictive, due to a lack of fundamental understanding of the chemo-mechanical mechanisms of embrittlement, despite considerable research efforts [9-15]. One challenge towards such an understanding is to establish the mechanistic connections between the mechanochemistry of hydrogen adsorption and the strength reduction of interface with realistic atomic geometry and under loading conditions pertinent to applications.

The ability of hydrogen to alter the mechanical properties of metals to the point of rendering them unreliable is an outstanding technological problem. The production of blisters by hydrogen put into steel is widely observed in early experiments. In the late 1970s, progress in technical efficiencies for hydrogen vessels came to a sudden halt. The problem was the hydrogen embrittlement mechanism, which has been observed earlier in other applications. Zapffe and Sims [16] developed the pressure-expansion theory of hydrogen embrittlement. This idea in its further developments [17-18] is that large pressure of hydrogen gas generated in internal voids or cracks will lead the coalescence of micro- voids or cracks. The coalescence of micro- voids and cracks will cause the sudden catastrophic fracture.

Metallic materials can often be described by arrays of polyhedra consisting of closely packed clusters of atoms. These space-filling polyhedra result from the competition of maximizing the coordination number of metallic atoms, minimizing the local free volume, and avoiding repulsive atomic overlap [19]. They can effectively serve as the basic structural units with which to analyze interstices for H absorption. In this letter, by combining the geometrical analysis of polyhedral interstitial sites of hydrogen [20-22], atomistic calculations, and thermodynamic theory of interfacial

embrittlement [5-8], we analyze how the structure of grain boundaries influences the propensity of chemisorption of hydrogen. The consequent embrittlement effects on grain boundary are then determined in the limits of separation at the fixed hydrogen concentration and fixed chemical potential. The results reveal the collective embrittling effects of surface adsorption and interfacial segregation of hydrogen at multiple trapping sites when the material is subjected to high charging pressures pertinent to efficient hydrogen storage and transportation. Implications on the transition between the transgranular and intergranular fracture are discussed by linking to a recent experiment showing that susceptibility to intergranular hydrogen embrittlement in metallic materials can be markedly reduced by grain boundary engineering [4].

3.2 Theoretical framework

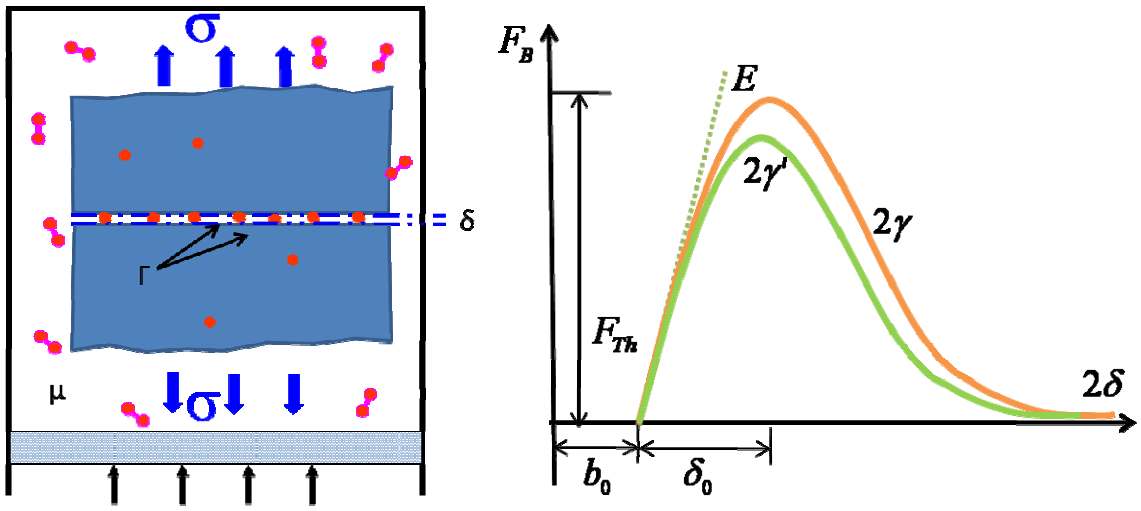

Figure 1. A illustritive figure of failure under hydrogen embrittlement. δ is the distance between the separated two layers of atoms at the interface, which have an equlibrium distance b_0. If the seperation is larger then δ0, the attractive forece between those two layers decrease and dimishies at certain distance. Under stress σ and chemical effect of hydrogen (red dimers), force-displacement curve of metal (orange → green) moves downward and work of seperation decreases (2γ>2 γ').

The idea of weakening by the hydrogen pressure-induced expansion is intuitive. But there are several phenomena that cannot be explained by this idea. First, the loss of ductility is often observed [23]. This seems to be a consequence of lowering the stress intensity factor, K, by hydrogen adsorption. But the decrease of dimple sizes in the samples charged with hydrogen is also observed.

The great loss of ductility at the diminished dimple size can be understood in terms of enhanced nucleation of voids at inclusions. In recent study of grain boundary engineering, the transition from dimple-mediated trans-granular fracture to cleavage and inter-granular fracture is reported by Ritchie and his coworkers [4]. In addition, the log *v*(K) curve is found to exhibit three stages [24]. There is a threshold value of K, below which the crack is immobile and above which *v* increases very rapidly with K (stage I). At a larger value of K, the crack velocity is independent of K (stage II). With increasing K, the crack velocity increases rapidly, which is considered as a unstable crack propagation. A decohesion model for hydrogen embrittlement can be developed to correlate with these results.

A decohesion model [25] supposes that dissolved hydrogen lowers the maximum cohesive force between the atoms of the metal at grain boundaries and at interfaces (Figure 3). It has a physical origin from the thermodynamic relations between the surface energy, segregation energy and stress state. Rice and Wang [26] develop this model and make a connection to Griffith's thermodynamic criterion of fracture. The surface free energy, γ, can be lowered by adsorption of hydrogen. The difference of adsorption energy between hydrogen in the bulk and hydrogen at surface/interface is defined as segregation energy. The energy lowered by hydrogen adsorption is the reduction of work of separation (the area between green and orange curves). In addition, hydrogen adsorption will reduce the maximum cohesive force and alter the cohesive stress-separation function.

If we assume that at an adsorption site i, the equilibrium chemical potential is μ^i with the corresponding concentration Γ^i. For a reversible change of state,

$$du = Tds + \sigma d\delta + \sum_i \mu^i \, d\Gamma^i \qquad (1)$$

The key assumption in equation (1) is that all thermodynamic functions referring to the interface could be determined by the values of T, δ, and Γ^i, regardless of the solute concentrations. Since the Helmholtz free energy $f = u - Ts = f(T, \delta, \Gamma^i)$, with fixed T, $df = \sigma d\delta + \sum_i \mu^i \, d\Gamma^i$. Hence, using a single variable pair of segregation concentration Γ and equilibrating chemical potential μ, the work of separation reduction can be related to the system energy reduction due to impurities absorption onto surface. One can consider two thermodynamic limits here. If the crack velocity is slow, fracture is quasi-static. Since the chemical potential of impurity at interface/surface is always equal to that in the surrounding environment, fracture proceeds under constant chemical potential. If

the crack velocity is fast, the concentration of impurity at interface/surface remain constant. One can derive the following two formulas associated with the aforementioned limits [26]

$$(2\gamma_{int})_{\Gamma=\text{const}} = \int_{\delta}^{\infty} \sigma d\delta = (2\gamma_{int})_{\Gamma=0} - \int_{0}^{\Gamma} \{\mu_b(\Gamma) - \mu_s(\Gamma/2)\} d\Gamma \qquad (2)$$

$$(2\gamma_{int})_{\mu=\text{const}} = \int_{\delta}^{\infty} \sigma d\delta = (2\gamma_{int})_{\Gamma=0} - \int_{-\infty}^{\mu} \{2\Gamma_s(\mu) - \Gamma_b(\mu)\} d\mu \qquad (3)$$

The impurity weakening effects on both the fast and slow fracture limits are evaluated in our atomistic models. We quantitatively studied the embrittling effect of hydrogen on Σ5[100], Σ17[100], Σ11[110] and Σ27[110] grain boundaries. Through analysis of these grain boundaries, connections are made between the hydrogen embrittlement effects with corresponding structural responses.

3.3 Simulation setup

We study the face-centered-cubic (fcc) Ni as a model system. The embedded atom method (EAM) potential [27-28] is used to describe the atomic interactions of Ni and H atoms. This potential has been well benchmarked by the bulk, surface, and defect properties measured from experiments (Table 1). Notably, the fitting data includes the zero-point energy which is important for hydrogen. Our simulation cell consists of a bicrystal slab with periodic boundary conditions in the grain boundary plane. It is known that hydrogen embedded in the transition metal such as Ni behavior chemically rather like He atom; namely, interstitially dissolved hydrogen in Ni generally exists in the form of atoms instead of H_2 molecules. The interstitial trapping sites in the bulk and at grain boundaries are characterized in terms of the polyhedral packing units of host Ni atoms [20]. Specifically, in a geometrical description of close packing of hard spheres of equal radii, the polyhedral hole refers to the void within the convex deltahedra, i.e, polyhedra, the vertices of which are the centers of neighboring atoms, and the faces of which are equilateral triangles. Suppose the deltahedra is not further divisible in the sense that it is too small to accommodate another host atom. The number of distinguishable and indivisible deltahedra is limited to nine in three dimensions. Because of the large free volume, the central hole of deltahedra is an energetically favorable interstitial site for trapping the small H atom [9]. Various deltahedral sites can be uniquely identified in atomistic calculations by

using the H atom as a probe of finding the interstitial position of local energy minimum, as detailed in Supplementary Materials.

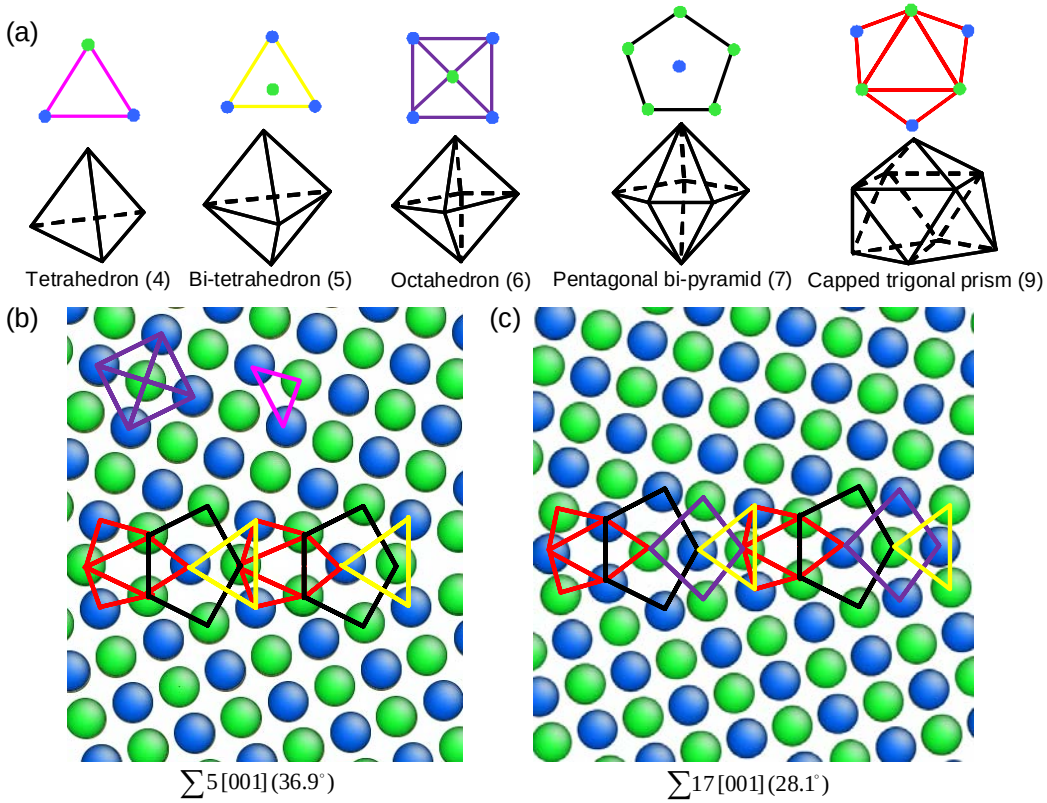

Figure 2. Symmetrical tilt grain boundaries with [001] tilt axis in the fcc Ni. (a) Projected and perspective views of packing units of deltahedron, the number of vertices is given in the bracket. (b) A $\sum 5\,(36.9^{\circ})$ boundary is composed of stacks of bi-tetrahedron, pentagonal bi-pyramid, capped trigonal prism; the latter two units form a compound hole. (c) A $\sum 17\,(28.1^{\circ})$ boundary is composed of stacks of the above three holes plus an octahedral hole. Green and blue atoms belong to adjacent (001) planes.

Figure 2 shows the relaxed atomic structures near two grain boundaries with the same [001] tilt axis, but different tilt angles, representing the typical boundaries that we have studied. It is seen that the bulk fcc lattice is simply composed of a periodic array of tetrahedra and octahedra units. In

contrast, the $\sum 5(36.9^{\circ})$ boundary is made up of three types of polyhedral holes: bi-tetrahedron, pentagonal bi-pyramid, capped trigonal prism, and the $\sum 17(28.1^{\circ})$ boundary is composed of an additional octahedral hole. In both boundaries, a capped trigonal prism always nests with a pentagonal bi-pyramid, forming a compound hole. The arrangement of these deltahedral units is periodic on grain boundaries as dictated by the periodicity of adjoining crystals. The center of these polyhedral holes is the metastable interstitial site for trapping the hydrogen atom.

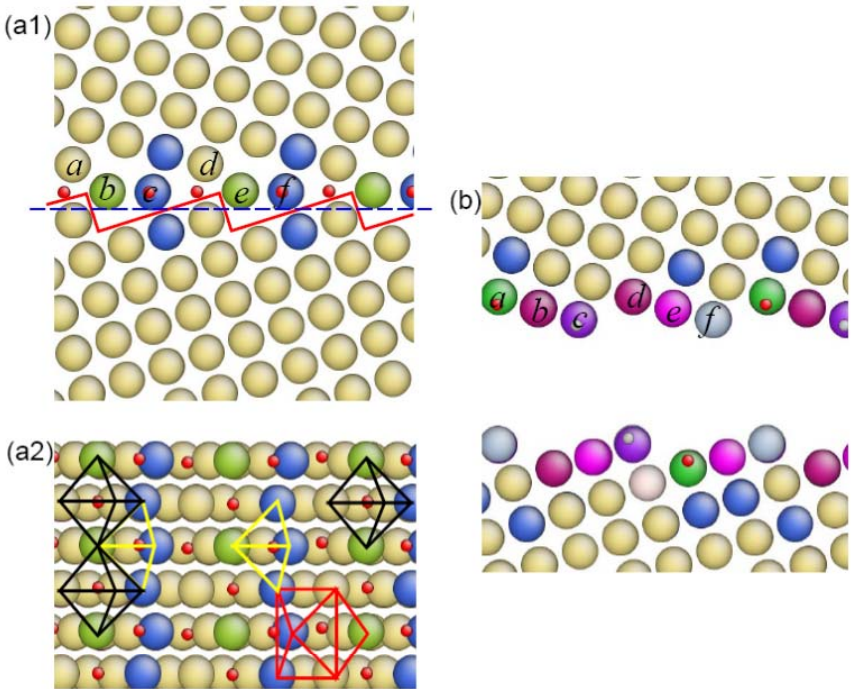

Figure 3. $\sum 5\ (36.9^{\circ})$ grain boundary with a full coverage of all the deltahedral interstitial sties by H atoms, from our preliminary study. (a1) and (a2) show the side and cross-sectional (cut through the blue dashed line) views of relaxed grain boundary, respectively; colored lines in (a2) indicate the deltahedral interstitial sites (see definitions in *Figure* 1). (b) The relaxed structure of fractured grain boundary; the cleavage plane is indicated by the red solid line in (a1); surface atoms are marked by *a-f* for finding the counterparts in (a1). Atoms are colored by the coordination number [62].

Figure 3 shows the atomic structures of a hydrogen-segregated grain boundary of $\sum 5(36.9^\circ)$ before and after fracture. In *Figure* 3(a), the boundary corresponds to the full coverage limit with a monolayer of H occupying all the boundary interstitial sites. The separated surface is shown in *Figure* 3(b), where the cleavage boundary plane (as indicated by the red solid line in *Figure* 3(a)) is obtained by energy minimization through direct displacement loadings at the top and bottom surface of the slab. Notice that the upper and lower separated surfaces in *Figure* 3(b) maintain the mirror symmetry with a relative in-plane shift, and H atoms are equally partitioned between the two surfaces, such that the surface concentration is reduced to one half of that of the intact, fully covered grain boundary.

3.4 Results and discussion

Table 1 presents the calculated hydrogen binding energy in vacuum and at various bulk or surface interstitial sites, as compared with available experimental values. Let us denote the molecular binding energy of H_2 as E_H per atom. It is computed by the EAM potential as -2.37eV, close to -2.4eV from experiment. This energy serves as a References to determine whether the atomic adsorption of hydrogen to various interstitial sites is endothermic or endothermic. Define the hydrogen binding energy in the bulk, ΔE_b, as the difference between the energy of the system with and without one H atom at a trapping site. Table 1 shows that the hydrogen binding to a octahedral site in the bulk ($\Delta E_b^{octa} = -2.20$ eV) is more energetically favorable than to a tetrahedral site ($\Delta E_b^{tetra} = -1.79$ eV) [27]. These results indicate that the H_2 dissolution in the bulk is endothermic, since its heat of solution at a favorable octahedral site is positive, i.e., $\Delta E_b^{octa} - E_{\mathrm{H}} = 0.17$ eV. In contrast, the adsorption of H at various sites of the low energy surface is exothermic. For example, the binding energy at the top and three-fold sites of the (111) surface are, respectively, -2.62eV and -2.71eV, both of which are less than E_H.

Likewise, we define the hydrogen binding energy at the grain boundary, ΔE_g^{ad}, and the fracture surface, ΔE_s^{ad}, as the difference between the energy of the system with and without one H atom at the respective trapping site. Table 2 lists the atomistically calculated ΔE_g^{ad} and ΔE_s^{ad}. It is seen that for both $\sum 5\ (36.9^\circ)$ and $\sum 17\ (28.1^\circ)$ boundaries, the most energetically favorable

binding site is the pentagonal bi-pyramidal hole. In contrast, the binding energies in the bi-tetrahedral hole are significantly different for two boundaries. At the fracture surface, the binding energies for the same type of binding sites are very close for the two boundaries.

Table 1. Trapping sites and binding energy of hydrogen (eV per atom).

	EAM potential	Experiment [61]
Molecular binding energy E_H	-2.37	-2.4
Bulk: tetrahedron	-1.79	-2.05
octahedron	-2.20	
(111) surface: top	-2.62	-2.70
three-fold	-2.71	

3.4.1 Adsorption energy, segregation energy and decohesion effect

Table 2. Trapping sites, H adsorption energies (eV per atom) at grain boundaries and fracture surfaces; segregation energies from the bulk lattice to grain boundaries and fracture surfaces, $\Delta E_g^{seg} = \Delta E_g^{ad} - \Delta E_b$ **and** $\Delta E_s^{seg} = \Delta E_s^{ad} - \Delta E_b$ **.**

Interstitial site	$\sum 5\,(36.9^\circ)$				$\sum 17\,(28.1^\circ)$			
	ΔE_g^{ad}	ΔE_s^{ad}	ΔE_g^{seg}	ΔE_s^{seg}	ΔE_g^{ad}	ΔE_s^{ad}	ΔE_g^{seg}	ΔE_s^{seg}
Pentagonal bi-pyramid	-2.52	-2.83	-0.32	-0.63	-2.54	-2.80	-0.34	-0.60
Octahedron	–	–	–	–	-2.45	-2.85	-0.25	-0.65
Capped trigonal prism	-2.42	-2.66	-0.22	-0.46	-2.42	-2.68	-0.22	-0.48
Bi-tetrahedron	-2.34	-2.82	-0.14	-0.62	-2.18	-2.82	+0.22	-0.62

Overall, Table 2 shows that the hydrogen binding energy at the surface ΔE_s^{ad} is lower than that at the corresponding site of grain boundary ΔE_g^{ad}, such that $\Delta E_g^{ad} - \Delta E_s^{ad}$ is inherently positive. To understand this trend from the perspective of chemo-mechanical coupling, we calculated the "chemical" energy change of embedding H into a rigid atomic network of host atoms of Ni, and the "mechanical" energy change due to the elastic relaxation associated with Ni-H bonding. As shown in Table S1 of Supplementary Materials, the former dominates the latter, confirming the previous quantum mechanical analysis. This result indicates that the positivity of $\Delta E_g^{ad} - \Delta E_s^{ad}$ can be mainly attributed to the chemical (electronic) effect of binding H to Ni; namely, the electron density at the Ni surface is lower than that of the grain boundary, enabling the lower embedding energy of H to the surface [30]. In contrast, the elastic relaxation caused by the size mismatch between the small H atom and the interstice of polyhedral holes plays a minor role [11].

The binding energies in Table 2 can be directly converted to the segregation energies that are often used in the thermodynamic theory of interfacial embrittlement [48]. Table 2 also presents the segregation energies of H atom from the bulk octahedral site to various interstitial sites at grain boundaries and corresponding fracture surfaces, denoted by ΔE_g^{seg} and ΔE_s^{seg}, respectively. It can be readily verified that $\Delta E_g^{seg} - \Delta E_s^{seg} = \Delta E_g^{ad} - \Delta E_s^{ad}$. These energies control how hydrogen affects the work of separation of grain boundaries, as discussed next. Note that the results in Tables 1 and 2 correspond to the dilute limit of low hydrogen concentration at the grain boundary and fracture surface. Our calculations also show that those binding energies are nearly identical to the corresponding values in the limit of high hydrogen concentration, with differences less than 2%. These results indicate that the interaction energies between different hydrogen atoms at the same and different types of deltahedral sites are negligibly small.

Based on the calculated binding energies, we have quantitatively evaluated the hydrogen embrittlement effects. We first studied the limit of fast separation of grain boundary with fixed hydrogen concentration. According to the thermodynamic theory of embrittlement of an interface with *n* types of segregation sites [7], the work of separation at fixed solute concentrations, W_Γ, valid at low temperatures is $W_\Gamma = W_0 - \sum_i \int_0^{\Gamma^i} \left[\mu_g^i(\Gamma^i) - \mu_s^i(\Gamma^i/2)\right] d\Gamma^i$. Here W_0 is the work of

separation of a clean boundary, Γ^i is the solute concentration at the *i*-th type interstitial site of the boundary, μ_g^i and μ_s^i are the chemical potential of solute at the grain boundary and separated surface, respectively. For fracture at low temperatures, one can justifiably neglect the entropic contributions to the chemical potentials [48] (as verified by our numerical calculations), so that $W_\Gamma \approx W_0 - \sum_i \int_0^{\Gamma^i} \left[\Delta E_g^{seg,i}(\Gamma^i) - \Delta E_s^{seg,i}(\Gamma^i/2)\right] d\Gamma^i$. As discussed earlier, the interactions between different hydrogen atoms at the same and different types of deltahedral sites are negligibly small, such that both $\Delta E_g^{seg,i}(\Gamma^i)$ and $\Delta E_g^{seg,i}(\Gamma^i)$ can be approximated as a constant, as assumed in the Langmuir-McLean adsorption isotherm [48]. It follows that

$$W_\Gamma \approx W_0 - \sum_i (\Delta E_g^{seg,i} - \Delta E_s^{seg,i})\Gamma^i \qquad \textbf{(1)}$$

In Eq. (1), the hydrogen concentration at the grain boundary Γ^i can be estimated by

$$\frac{\Gamma^i}{\Gamma_g^{\max,i} - \Gamma^i} = x \exp\left(-\frac{\Delta E_g^{seg,i}}{kT}\right) \qquad \textbf{(2)}$$

where $\Gamma_g^{\max,i}$ is the maximum concentration of *i*-th type of the polyhedral hole at the grain boundary and x is the fraction of occupied octahedral sites in the bulk. An order-of-magnitude estimate of $\Gamma_g^{\max,i}$ can be made by considering a square network of possible adsorption sites, spaced 0.5nm from one another, giving $\Gamma_g^{\max,i} \approx 4\times10^{18}$ m^{-2} $\approx 7\times10^{-6}$ mol m^{-2}.

It should be noted that the embrittlement effect can be drastically increased in the limit of slow separation at fixed hydrogen chemical potential. The work of separation at fixed chemical potential, W_μ, valid at high temperatures is $W_\mu = W_0 - \sum_i \int_{-\infty}^{\mu} \left[2\Gamma_s^i(\mu) - \Gamma_g^i(\mu)\right] d\mu$ [48], where the upper integration limit is taken as the chemical potential of H in the bulk $\mu = kT\ln x$. It can be shown that the work of separation in the slow and fast separation limits can be related according to $W_\Gamma - W_\mu = \sum_i \int_{\Gamma_0^i}^{2\Gamma_s^i(\mu_0)} \left[\mu_0 - \mu_s^i(\Gamma^i/2)\right] d\Gamma^i$, where μ_0 is the solute chemical potential in the bulk

leading to a equilibrium solute concentration of Γ_0^i at the grain boundary, and $\Gamma_s^i(\mu_0)$ in the integration limit is the solute concentration of the separated surface with the surface chemical potential equal to that in the bulk μ_0. To a first approximation, the work of separation between the two limits can be estimated by

$$W_\Gamma - W_\mu = \sum_i (\Delta E_g^{seg,i} - \Delta E_s^{seg,i})(2\Gamma_s^i - \Gamma_0^i), \quad \textbf{(3)}$$

where the hydrogen concentration at the fracture surface Γ_s^i is determined by condition of chemical potential equilibrium between the bulk and surface,

$$\frac{\Gamma_s^i}{\Gamma_s^{\max,i} - \Gamma_s^i} = x \exp\left(-\frac{\Delta E_s^{seg,i}}{kT}\right), \quad \textbf{(4)}$$

Note that Γ_s^i in Eq. (4) is governed by $\Delta E_s^{seg,i}$ for separation at the fixed chemical potential, as opposed to Γ_s^i in Eq. (2) controlled by $\Delta E_b^{seg,i}$ for separation at the fixed concentration. To test the validity of our first order approximations, we provides table 4. It's convincing that approximations in equation (1) are (3) are good enough for the calculation of hydrogen embrittlement effect.

Based on Eqs. (1) and (2), we evaluated the equilibrium hydrogen concentrations and associated embrittlement effects at hydrogen charging pressures pertinent to the efficient transmission of hydrogen gas, e.g., 20-100 MPa in pipelines [31]. In a recent experiment by Bechtle et al. [4], hydrogen embrittlement was studied with the hydrogen charging pressures between 50-140 MPa and temperatures between $150 - 200^\circ$C. The corresponding equilibrium H lattice concentration x was estimated from Sievert's law, giving a range of 1000-3000 atomic parts per million (appm) that was consistent with experimental measurements [4]. Taking a representative high concentration in experiment, e.g., $x = 3000$ appm when $T = 200^\circ$C, we estimated the H concentrations at grain boundaries using Eqs. (1) and (2) with atomistic calculation results of segregation energies (Table 2). For the $\sum 5\,(36.9^\circ)$ boundary with $\Gamma_g^{\max,i} = 0.85\times10^{-5}$ mol/m², Γ^i is 0.75×10^{-5} mol/m² in the most energetically favorable site of the pentagonal bi-pyramidal hole, giving 88% coverage of this type of site; in the capped trigonal prism, $\Gamma^i = 0.34\times10^{-5}$ mol/m², giving 40% coverage; in the bi-

tetrahedron, $\Gamma^i = 0.07\times10^{-5}$ mol/m², giving 8% coverage. Clearly, these high, but different coverages manifest the segregation equilibrium of H at multiple polyhedral sites as controlled by Eq. (2) [7].

Using the above estimated H concentrations, together with the separation energy of clean boundaries given in Supplementary Materials (Table S2), we calculated the work of separation, W_Γ, of the $\sum 5\,(36.9^\circ)$ grain boundary based on Eq. (1), and obtained $W_\Gamma = 3.26$ J/m² for a H-adsorbed boundary, as opposed to $W_0 = 3.60$ J/m² for a clean boundary. This is the first key result of this work.

Along the same line, we evaluated the hydrogen embrittlement effects on different types of high-angle and low-angle grain boundaries with either the [100] or [110] tilt axis. The results given in Table 3 shows that the reduction of the separation energy is more or less around 10% under fast fracture limit, despite the fact that different boundaries consist of various combinations of deltahedral holes with different spatial arrangements. In contrary, the reduction of the separation energy under slow fracture limit is about 50%. A simple kinetic analysis shows us that in reality, most fractures are close to the fast fracture limit.

$$\boldsymbol{Diffusion\ velocity\ of\ hydrogen = a_0\nu_0 e^{-\frac{\Delta E}{kT}} \approx 2\times10^{-10}m\times10^{13}s^{-1}\times e^{-\frac{0.2eV}{0.04eV}} \approx 10m/s \ll 1000m/s = Speed\ of\ slow\ fracture}$$

Table 3. Interface decohesion by hydrogen under fast and slow fracture limits. The simulated experimental temperature is 473.1K, pressure is 100MPa and concentration in crystal Ni is 3000 appm.

	Σ5[100]	Σ17[100]	Σ11[110]	Σ27[110]
γ_{gb} (J/m²)	1.01	1.04	0.28	0.62
$2\gamma_s$ (J/m²)	4.61	4.50	4.57	4.55
W (J/m²)	3.60	3.46	4.29	3.93
Fast limit:				
ΔW (J/m²)	0.413	0.450	0.329	0.593
Percentage	-10%	-12%	-7%	-13%
Slow limit:				
ΔW^a (J/m²)	1.659	1.824	2.025	2.487
Percentage	-46%	-52%	-47%	-63%

Table 4. Interface decohesion by hydrogen calculated by approximation as equation (1) and (3), compared with Rice and Wang's theoretical integration formula [59].

	Σ5[100]	Σ17[100]	Σ11[110]	Σ27[110]
Fast limit ΔW (J/m^2):				
Approximation	0.413	0.450	0.329	0.593
Integration	0.365	0.399	0.297	0.500
Slow limit ΔW^a (J/m^2):				
Approximation	1.659	1.824	2.025	2.487
Integraton	1.703	1.865	2.068	2.849

Hence, we conclude that the reduction of the interfacial strength by hydrogen is limited; the embrittlement effect is more significant during a slow fracture than a fast fracture. However, under similar fracture speed, the weakening effect is nearly identical for different grain boundaries.

In order to understand the limited reduction of the interfacial strength, we compared the adsorption energies at various segregation sites. Figure 4 shows a collection of calculated $\Delta E_g^{ad,i}$ and $\Delta E_s^{ad,i}$ at various sites for different (001) and (011) tilt boundaries; these values are plotted as a function the corresponding electron density at the adsorption site. One notable feature is that there exists a finite energy gap (no less than 0.2eV) between $\Delta E_g^{ad,i}$ and $\Delta E_s^{ad,i}$, irrespective of the type of segregation sites. Also note that compared to the relatively large scattering of adsorption energies at various grain boundary sites $\Delta E_g^{ad,i}$ (circles), $\Delta E_s^{ad,i}$ for different types of surface trapping sites (stars) are much closer to each other. Both features can be rationalized in terms of the hydrogen alloying behaviors in metals. Namely, the energy of interaction between hydrogen and the host transition metal such as Ni is mainly governed by the embedding energy which is a function of the electron density at the adsorption site determined by the host metal [32]. The nearly constant value of $\Delta E_s^{ad,i}$ arises mainly because of the gradual attenuation of the electron density in the free space outside the surface, enabling a hydrogen atom to find an optimum (minimum) embedding energy. In contrast, the

range of variation of the electron density at an internal interstitial site in the grain boundary is limited due to the geometrical constraint of surrounding atoms. As a result, the corresponding embedding energy cannot be optimized to the minimum, giving various values of $\Delta E_g^{ad,i}$ governed by the local atomic geometry of polyhedral holes.

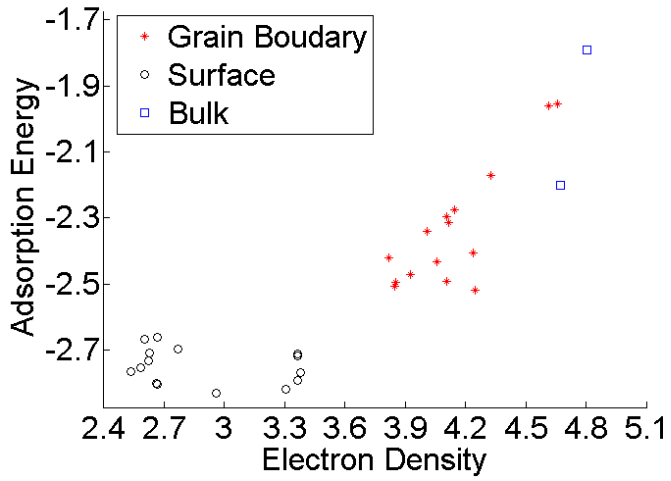

Figure 4. Adsorption energies are plotted as a function the corresponding electron density at the adsorption site. This provides the electron density basis of hydrogen decohesion effect.

Based on the foregoing analysis of local electron density-governed adsorption energies, we can further rationalize the limited reduction of the interfacial strength. Let us recall from Eq. (1) that the embrittlement is controlled by the collective effect of multiple segregation sites. For each type of site, the extent of embrittlement is determined by the product between the segregation energy difference of $\Delta E_g^{seg,i} - \Delta E_s^{seg,i}$ and the H concentration at the grain boundary Γ^i. The former is equal to the adsorption energy difference of $\Delta E_g^{ad,i} - \Delta E_s^{ad,i}$, while according to Eq. (2), the latter is governed by $\Delta E_g^{seg,i}$, or equivalently $\Delta E_g^{ad,i}$ for a given lattice concentration. Since the variation of $\Delta E_s^{ad,i}$ is relatively small compared to $\Delta E_g^{ad,i}$, the extent of embrittlement should be mainly controlled by $\Delta E_g^{ad,i}$. We note that $\Delta E_g^{ad,i}$ is intrinsically negative and it appears in the exponential of Eq. (2). As a result, for different segregation sites, if the magnitude of $\Delta E_g^{ad,i}$ is large, Γ^i will be high, and the induced decrease of the work of separation will be significant. However, the variation of

$\Delta E_g^{ad,i}$ is limited because of the geometrical constraints on the allowable electron densities within the polyhedral hole at the grain boundary as discussed earlier. It follows that the most embrittling site is the one with a minimum (negative) value of $\Delta E_g^{ad,i}$, giving a minimum $\Delta E_g^{seg,i} - \Delta E_s^{seg,i} \approx 0.25$ eV per H atom. On the other hand, under the high charging loading pertinent to efficient hydrogen transmission, Γ^i at the site with the minimum $\Delta E_g^{ad,i}$ approaches the saturation limit of $\Gamma_g^{\max,i} \approx 4\times10^{18}$ m^{-2}, which is also intrinsically determined by the atomic geometry of grain boundary or simply the lattice constant. It follows that the product between $\Delta E_g^{ad,i} - \Delta E_s^{ad,i}$ and $\Gamma_g^{\max,i}$ is approximately 0.16 J/m^{-2}, which corresponds to about 5% reduction of work of separation of pure grain boundaries (taking a representative value of $W_0 = 3$ J/m^{-2}). This value gives an order-of-magnitude estimate to the decrease of W_0 due to hydrogen segregation. Because of the high charging load, the weakening effects due to hydrogen adsorbed at other types of sites can make comparable contributions with detailed example given earlier, so that the total weakening amounts to about 10% reduction of W_0.

3.4.2 Hydrogen embrittlement induced change of fracture mode

The above results of hydrogen-mediated interfacial embrittlement can be correlated to the recent experiment of intergranular hydrogen embrittlement of polycrystalline Ni by Bechtle et al. [4]. They found that (i) for tensile testing in uncharged conditions, ductile transgranular fracture dominates; (ii) after hydrogen charging at $x = 3400$ appm, fracture surfaces show exclusively intergranular fracture; (iii) under the same charging load, increasing the fraction of "special" grain boundaries (low sigma number) by the thermo-mechanical treatment (so-called grain boundary engineering) lowers the fraction of intergranular fracture significantly.

To rationalize the above experimental observations, we note that the selection of fracture path in polycrystalline samples is governed by the orientation of the plane with maximum normal stress relative to (i) the weak crystal plane (i.e., the $\{111\}$ plane for an fcc metal of Ni) for transgranular fracture, and (ii) the weak grain boundary for intergranular fracture, as well as connectivity of "weak" grain boundary planes. Table 2 lists the calculated separation energy of crystallographic planes and grain boundaries. It is seen that without hydrogen charging, the

separation energy of the $\{111\}$ plane is similar to that of grain boundaries, such that the transgranular fracture is expected to dominate over the intergranular fracture because of the additional resistances cause by the typically larger misalignment of weak grain boundaries in different grains. With hydrogen charging at $x = 3000$ appm, the separation energy of various grain boundaries is lowered by more or less 10%, so that the fracture of relatively weak grain boundaries with high sigma number can dominate over that of the crystallographic plane of e.g., $\{111\}$.

There are two factors underlying the fracture mode transition. The first one is the valve effect [12, 66-69]. The 10% reduction of work of separation in Table 2 is only for cleavage separation of a grain boundary. In metals, such separation typically involves plastic behaviors. It is known that the plastic work depends exponentially on the local stress at a crack tip. From a previous study by McMahon [69], it is argued that "*The segregation of impurities to grain boundaries of steel can result in reductions of fracture toughness of the order of 95%, which can be caused by reduction in the work of ideally brittle fracture of the order of 10%*". The second factor is related to the decrease of separation energy that could offset the unfavorable geometrical effects (figure 4). Figure 4 is an illustration of the transition from the intergranular to transgranular fracture. When such transition happens, inequality (3) should be satisfied:

$$\frac{G_{gb}(\varphi)}{G_{\{111\}}(\theta)} > \frac{W_{gb}(\Gamma)}{W_{\{111\}}}, \qquad (3)$$

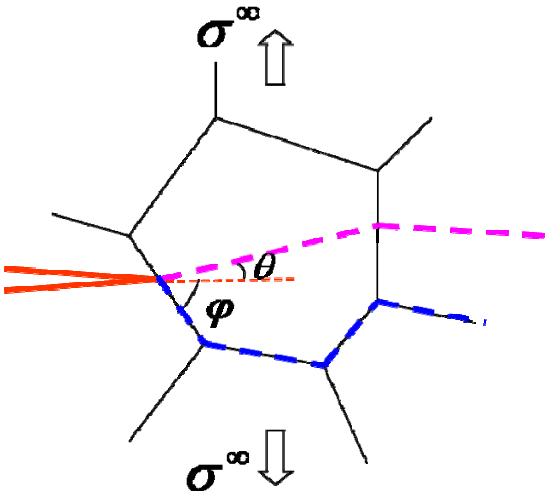

Figure 5. Illustration of fracture mode transition. The change from the transgranular fracture to intergranular fracture results from the competition between the fracture driving force and resistance due to a geometrical effect. System will naturally select the fracture path with the largest energy release.

In inequality (3), the left hand side is the ratio of driving force of fracture while the right hand side is the ratio of resistance. $G_{gb}(\varphi)$ and $G_{\{111\}}(\theta)$ are the energy release rate of separating grain boundary and {111} planes. They both depend on the angles between the direction of crack extension and the plane of maximum normal stress, which are φ and θ here as shown in figure 4. $W_{gb}(\Gamma)$ and $W_{\{111\}}$ are the corresponding work of separations. $W_{gb}(\Gamma)$ depends on the local concentration Γ. To achieve inequality (3), the key is to reduce the separation energy of grain boundary by increasing Γ. Accounting for the valve effect, a transition from the intergranular to transgranular fracture will happen automatically, when inequality (3) is satisfied. Furthermore, since the strength reduction is insensitive to the sigma number of grain boundaries, it is understandable that increasing the fraction of grain boundaries with low sigma number (equivalently reducing the fraction of weak grain boundaries) can lower the fraction of intergranular fracture. Therefore, the experimental observation by Bechtle et al. [4] regarding the increase of material strength by grain boundary engineering is explained by combining the valve effect and geometrical effect.

3.5 Conclusion

This chapter presents a comprehensive model of hydrogen embrittlement. It quantitatively bridges the atomic structures with the weakening effect of hydrogen segregation on grain boundaries. It connects experimental measurements with the atomistic modeling and thermodynamic theory [59]. We study the embrittlement effect of hydrogen in an FCC metal of Ni. The thermodynamic limits of fast and slow fractures are considered. The reduction of work of separation for different grain boundaries due to hydrogen segregation is systematically evaluated. It is shown that the embrittlement effect by hydrogen on grain boundaries is limited; the slower the fracture process, the more significant the embrittlement effect will be. A simple kinetic analysis of hydrogen diffusion versus crack velocity shows that most fractures in reality should be close to the fast fracture limit.

It is shown that the reduction of work of separation is respectively about 10% and 50% under the fast and slow fracture limits when T=473k and P=100MPa. This implies that the strength reduction of grain boundary by hydrogen adsorption is limited; the slower the process is, the more significant the embrittlement effect will be. A simple kinetic analysis of hydrogen diffusion indicates that in reality, most fractures should be close to the fast fracture limit under typical experimental conditions.

We use the deltahedral packing units to characterize the atomic structures of grain boundaries. The center of each deltahedron is considered as a stable interstitial site for hydrogen adsorption. Basing on the local electron density approximation, we assume that the same deltahedron always has similar adsorption and segregation energies, no matter what type of grain boundary it belongs to. Hence, one can calculate the reduction of separation energy of a grain boundary by a simple analysis of its constitute deltahedrons and their accumulative weakening effects associated with hydrogen adsorption. The accuracy of such approximation has been verified.

The hydrogen embrittlement of grain boundaries may cause the transition of the failure mode from the ductile intergranular to brittle transgranular fracture. Such transition has been observed in experiments by Bechtle et al. [4]. The fracture mode is known to be governed by the competitions between the energy release rates and associated resistance (e.g., work of separation). Our study reveals the controlling factors of the fracture mode transition: the first is the valve effect of the plastic work on fracture that depends exponentially on the local stress at a crack tip, and the second is the geometric effect on the driving force of fracture that depends largely on the local geometry of the crack tip. In short, the first effect changes the work of separation, while the second influences the energy release rate.

Lastly, to confirm the efficacy of this valve effect, it is necessary to extend the present coupled atomistic and thermodynamic model to address the kinetic aspects, as well as the coupling effects of H-affected plasticity and decohesion for realistic 3D crack geometries on the time scale relevant to laboratory experiments [15, 33-35].

References

1. **Service, R.F., *The hydrogen backlash.* Science, 2004. 305(5686): p. 958-961.**
2. **Myers, S.M., et al., *Hydrogen Interactions with Defects in Crystalline Solids.* Reviews of Modern Physics, 1992. 64(2): p. 559-617.**
3. **Birnbaum, H.K., et al., *Mechanisms of hydrogen related fracture-a review* in *Corrosion Deformation Interactions CDI'96* T. Magnin, Editor. 1997, The Institute of Materials: UK. p. 172-195.**
4. **Bechtle, S., et al., *Grain-boundary engineering markedly reduces susceptibility to intergranular hydrogen embrittlement in metallic materials.* Acta Materialia, 2009. 57(14): p. 4148-4157.**
5. **Rice, J.R., *Hydrogen and Interfacial Cohesion*, in *Effect of Hydrogen on Behavior of Materials*, A.W. Thompson and I.M. Bernstein, Editors. 1976, The Metallurgical Society of AIME: New York. p. 455-466.**
6. **Hirth, J.P. and J.R. Rice, *On the Thermodynamics of Adsorption at Interfaces as It Influences Decohesion.* Metallurgical Transactions A, 1980. 11(9): p. 1501-1511.**
7. **Rice, J.R. and J.S. Wang, *Embrittlement of Interfaces by Solute Segregation.* Materials Science and Engineering A, 1989. 107: p. 23-40.**
8. **Mishin, Y., P. Sofronis, and J.L. Bassani, *Thermodynamic and kinetic aspects of interfacial decohesion.* Acta Materialia, 2002. 50(14): p. 3609-3622.**
9. **Baskes, M.I. and V. Vitek, *Trapping of Hydrogen and Hellium at Grain-Boundaries in Nickel - An atomistic Study.* Metallurgical Transactions A, 1985. 16(9): p. 1625-1631.**
10. **Mutschele, T. and R. Kirchheim, *SEGREGATION AND DIFFUSION OF HYDROGEN IN GRAIN-BOUNDARIES OF PALLADIUM.* Scripta Metallurgica, 1987. 21(2): p. 135-140.**
11. **Geng, W.T., et al., *Hydrogen-promoted grain boundary embrittlement and vacancy activity in metals: Insights from ab initio total energy calculatons.* Materials Transactions, 2005. 46(4): p. 756-760.**
12. **Van der Ven, A. and G. Ceder, *The thermodynamics of decohesion.* Acta Materialia, 2004. 52(5): p. 1223-1235.**
13. **Jiang, D.E. and E.A. Carter, *First principles assessment of ideal fracture energies of materials with mobile impurities: implications for hydrogen embrittlement of metals.* Acta Materialia, 2004. 52(16): p. 4801-4807.**
14. **Lu, G. and E. Kaxiras, *Hydrogen embrittlement of aluminum: The crucial role of vacancies.* Physical Review Letters, 2005. 94(15): p. 155501.**
15. **Song, J., M. Soare, and W.A. Curtin, *Testing continuum concepts for hydrogen embrittlement in metals using atomistics.* 2009, submitted.**
16. **Zapffe, C.A. and C.E. Sims, *Hydrogen embrittlement, internal stress and defects in steel.* Transactions of the American Institute of Mining and Metallurgical Engineers, 1941. 145: p. 225-261.**
17. **Brown, J.T. and W.M. Baldwin, *HYDROGEN EMBRITTLEMENT OF STEELS.* Journal of Metals, 1954. 6(2): p. 298-303.**
18. **Tetelman, A.S. and W.D. Robertson, *DIRECT OBSERVATION AND ANALYSIS OF CRACK PROPAGATION IN IRON-3 PERCENT SILICON SINGLE CRYSTALS.* Acta Metallurgica, 1963. 11(4): p. 415-&.**
19. **Sutton, A.P. and R.W. Balluffi, *Interfaces in Crystalline Materials* 1995, Oxford, UK: Oxford University Press.**

20. **Ashby, M.F., F. Spaepen, and S. Williams, *Structure of Grain-Boundaries Described as a Packing of Polyhedra.* Acta Metallurgica, 1978. 26(11): p. 1647-1663.**
21. **Pond, R.C., V. Vitek, and D.A. Smith, *Grain-Boundary Structures in FCC and BCC Metals and Sites for Segregated Impurities.* Acta Crystallographica A, 1979. 35(JUL): p. 689-693.**
22. **McDowell, D.L., *Viscoplasticity of heterogeneous metallic materials.* Materials Science & Engineering R-Reports, 2008. 62(3): p. 67-123.**
23. **Garber, R., I.M. Bernstein, and A.W. Thompson, *EFFECT OF HYDROGEN ON DUCTILE FRACTURE OF SPHEROIDIZED STEEL.* Scripta Metallurgica, 1976. 10(4): p. 341-345.**
24. **Briant, C.L., H.C. Feng, and C.J. McMahon, *EMBRITTLEMENT OF A 5 PCT NICKEL HIGH-STRENGTH STEEL BY IMPURITIES AND THEIR EFFECTS ON HYDROGEN-INDUCED CRACKING.* Metallurgical Transactions a-Physical Metallurgy and Materials Science, 1978. 9(5): p. 625-633.**
25. **Oriani, R.A. and P.H. Josephic, *EQUILIBRIUM ASPECTS OF HYDROGEN-INDUCED CRACKING OF STEELS.* Acta Metallurgica, 1974. 22(9): p. 1065-1074.**
26. **Rice, J.R. and J.S. Wang, *EMBRITTLEMENT OF INTERFACES BY SOLUTE SEGREGATION.* Materials Science and Engineering a-Structural Materials Properties Microstructure and Processing, 1989. 107: p. 23-40.**
27. **Angelo, J.E., N.R. Moody, and M.I. Baskes, *Trapping of Hydrogen to Lattice-Defects in Nickel.* Modelling and Simulation in Materials Science and Engineering, 1995. 3(3): p. 289-307.**
28. **Baskes, M.I., et al., *Trapping of hydrogen to lattice defects in nickel.* Modelling and Simulation in Materials Science and Engineering, 1997. 5(6): p. 651-652.**
29. **Li, J., *AtomEye: an efficient atomistic configuration viewer.* Modelling and Simulation in Materials Science and Engineering, 2003. 11(2): p. 173-177.**
30. **Cottrell, A.H., *Strength of Grain-Boundaries in Impure Metals* Materials Science and Technology, 1990. 6(4): p. 325-329.**
31. **Novak, P., et al., *A statistical, physical-based, micro-mechanical model of hydrogen-induced intergranular fracture in steel.* Journal of the Mechanics and Physics of Solids, 2010. 58(2): p. 206-226.**
32. **Cottrell, A.H., *Concepts of the Electron Theory of Aollys*. 1998, London: IOM Communications Ltd.**
33. **Zhu, T., J. Li, and S. Yip, *Atomistic study of dislocation loop emission from a crack tip.* Physical Review Letters, 2004. 93: p. 025503.**
34. **Zhu, T., J. Li, and S. Yip, *Atomistic configurations and energetics of crack extension in silicon.* Physical Review Letters, 2004. 93: p. 205504.**
35. **Warner, D.H., W.A. Curtin, and S. Qu, *Rate dependence of crack-tip processes predicts twinning trends in f.c.c. metals.* Nature Materials, 2007. 6: p. 876–881.**
36. **McMahon, C.J. and V. Vitek, *EFFECTS OF SEGREGATED IMPURITIES ON INTERGRANULAR FRACTURE ENERGY.* Acta Metallurgica, 1979. 27(4): p. 507-513.**

4. NANOSCALE FRACTURE MECHANISMS OF SILICON

Silicon and graphene are being widely considered as candidate anode materials for lithium-ion battery [1-8]. Improvement of the anode performance has been shown in recent experiments by utilization of nanostructured materials, such as thin films [7], nano-particles [8] and nano-wires [1]. As the first step of understanding the mechanical failure of anode, a study of fracture mechanisms in pristine nanomaterials is necessary, which provides a basis of studying their lithiation/delithation responses. For example, we ask whether it is possible to take advantage of the high capacity of silicon while minimize the diffusion induced deformation mismatch. Chapter 4 and chapter 5 presents: (i) nanoscale fracture mechanisms in silicon and graphene; (ii) tailoring the size to avert fracture in strain-engineered nanomaterials (using graphene as a model material).

In this chapter, an atomistic study is preformed to characterize the formation and extension of nano-sized cracks in silicon. By using atomistic reaction pathway calculations, we determine the energetics governing the brittle and ductile responses of an atomically sharp crack in silicon, involving the competing processes of cleavage bond breaking, dislocation emission, and amorphization by the formation of five- and seven-membered rings. We show that the nanoscale fracture process depends sensitively on the system size and loading method.

A similar study has also been performed for nanoscale fracture of graphene (chapter 5). The extension of nanosized crack in graphene also involves cleavage bond breaking and amorphization. Additionally, based on the study of nanoscale fracture mechanisms of silicon and graphene, we explore whether it is possible to avert the cleavage fracture at nanoscale. The fracture mechanics concept is used to determine the limit of applied strain and system size. Our study reveals that by tailoring the system size, the mode I cleavage fracture could be suppressed. We use graphene as a model material for its application in strain engineering of band gap. More specifically, two experimental methods have been used to control the electronic properties of graphene: applying external strain and tailoring system size. The second part of this chapter describes a model to determine the critical conditions of tuning the band gap of grapheme without fracture.

4.1 Introduction

Nanoscale fracture experiments and simulations demonstrate the potential to probe and exploit the ultimate strength of materials [9-16]. These studies also point to the need for an understanding of the mechanisms governing the formation and extension of nanometer-sized cracks in a broad range of fields and applications [17-21]. Here we present an atomistic study of nanoscale fracture mechanisms under ultra-high stresses, being close to but below the ideal tensile strength, i.e., the athermal limit of instantaneous fracture. Such high stresses can easily arise in materials with nanometer-sized cracks. While the nanocrack response in this sub-critical load range controls the fracture behavior of small-volume materials, only few theoretical studies have emerged in recent years [22-25]. This is largely because from an atomistic-modeling standpoint, the fracture under a sub-critical load is hardly accessible by direct molecular dynamics (MD) simulations due to the time-scale constraint [26]. To overcome the time-scale limitation of MD, we adopt the nudged elastic band (NEB) method [27] to model the sub-critical fracture in terms of the energetics of nanocrack formation and extension.

The quantification of atomic-level energetics clearly reveals an essential feature of fracture in crystals: the lattice discreteness causes the atomic-scale corrugation of the energy landscape, giving rise to the lattice trapping effect [28]. Specifically, under an applied load, a crack can be locally "trapped" in a series of metastable states with different crack lengths and crack-tip atomic structures. The time-dependent kinetic crack extension then corresponds to the transition of the system from one state to the other via thermal activation [29]. This lattice-trapping effect is expected to play an increasingly important role in fracture with reduced system size, though its significance varies for different crystals, depending on the bonding characteristics such as the interaction range and shape of the interatomic force law [25,30-31]. From the atomistic modeling perspective, the existence of lattice-trapped states enables us to capture and examine in detail various brittle and ductile responses, including the competing processes of cleavage fracture, dislocation emission, and amorphization [22, 32-34].

In this section, we examine the thermodynamic driving forces and activation barriers associated with growth of a crack, dislocation emission, and amorphization at a crack tip subjected to either stress or strain loading. We show that for a Stillinger-Weber (SW) potential of silicon [35], amorphization is most favored both thermodynamically and kinetically. Based on this result,

amorphization is expected to be the dominant crack-tip response. This prediction is consistent with direct MD simulations [22,36], but is valid for a much wider range of stresses, temperatures and loading rates. We further investigate the energy landscape beyond the initial formation of dislocations and five/seven-membered rings. Our results exhibit energy barriers that govern the subsequent defect migration and nucleation. The competition of these defect processes dictates stress relaxation at a crack tip, and controls fundamentally the brittle-to-ductile transition of fracture.

4.2. Nanocrack formation and size effect

Consider a central crack in an otherwise perfect crystal of silicon under a uniform far-field load. We use the standard supercell setup with periodic boundary conditions [37]. The silicon atoms form a diamond-cubic crystalline network, characterized by localized and directional covalent bonds that generally enhance the lattice trapping effect [97]. Consider the silicon under a high stress of 10GPa, about 1/4 of the ideal tensile strength in the $\langle 111 \rangle$ direction, 38GPa, as predicted by the SW potential [98]. We determine the atomic geometry and energetics of formation and extension of a nano-sized crack. Here we focus on quasi-2D fracture and ignore the 3D mechanism of crack advancement by double-kink formation and migration along the crack front [31-32,38].

Figure 1(a) shows the system energy per unit cell along the crack front as a function of crack length under both the stress-controlled (red) and strain-controlled (blue) loading conditions. In this calculation, the supercell is 18.3nm wide, 20.1nm high, and 3.8nm thick, with a total of 1680 atoms. In *Figure* 1(a), circles represent the local energy minima at different crack lengths, i.e., different numbers of broken bonds. These metastable states arise because of the lattice trapping effect. They are numerically obtained by using the constrained energy minimization method, as detailed in Appendix A2. The attainment of these states enables us to quantitatively evaluate the applicability of the Griffith theory to nanoscale fracture. According to this theory [39], fracture occurs at a critical crack length when the system energy maximizes. From the envelop curve connecting circles (dashed line), we determine the Griffith crack lengths for stress-controlled and strain-controlled fractures; both are close to $2a_c \approx 2.8\text{nm}$. On the other hand, the critical crack length can be predicted based on the Griffith formula. Namely, the critical energy release rate G_c and the stress intensity factor K_c satisfy

the condition of $G_c = K_c^2 / E' = (\sigma\sqrt{\pi a_c})^2 / E' = 2\gamma_s$; using the surface energy ($\gamma_s = 1.45\text{J/m}^2$) and effective Young's modulus in the $\langle 111 \rangle$ direction ($E' = 148.6\text{GPa}$) given by the SW potential [98], one predicts $2a_c = 2.74\text{nm}$, as indicated by the vertical line in *Figure* 1(a). The agreement between the two methods of predicting the critical crack length, with a difference less than one atomic spacing of 0.33nm, suggests that the Griffith formula is applicable to nanoscale fracture. Note that the above estimate of the stress intensity factor, $K = \sigma\sqrt{\pi a}$, ignores the finite-size effect of the system. We have validated this approximation, as shown later in the study of the image-crack effect.

In Fig.1 (a), each curve connecting two adjacent circles measures the energy variation along the minimum energy path (MEP) [93] for breaking or healing one crack-tip bond, i.e., crack extension or receding by one bond distance. These MEP curves are calculated from the nudged elastic band method, as detailed in Appendix A. Each MEP involves a forward and a backward transition. We extract the energy barriers along the thermodynamically favorable directions of transition. So the activation energies shown in *Figure* 1(b) are the barriers of crack extension when $a > a_c$, and the barriers of crack healing when $a < a_c$.

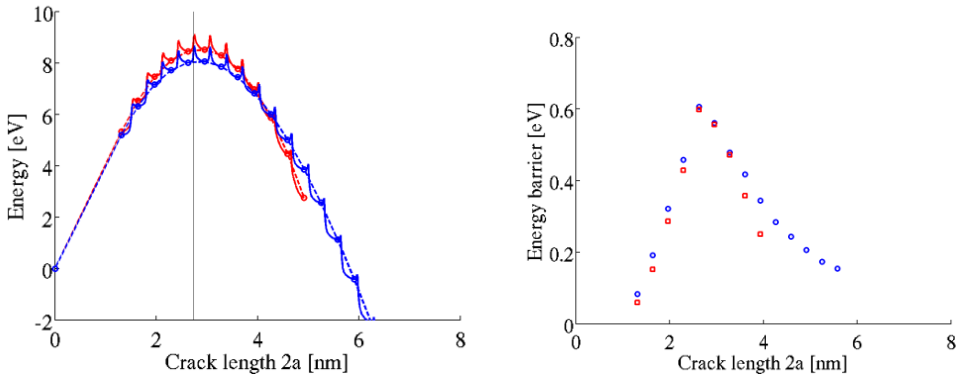

(a) **(b)**

Figure 1. Nanoscale fracture in silicon under the tensile stress of 10GPa. (a) Energetics of nanocrack formation under the stress-controlled (red) and strain-controlled (blue) loading conditions. (b) Energy barriers of crack extension and healing extracted from (b). For (a) and (b), the supercell size is 18.3x20.1x3.8nm

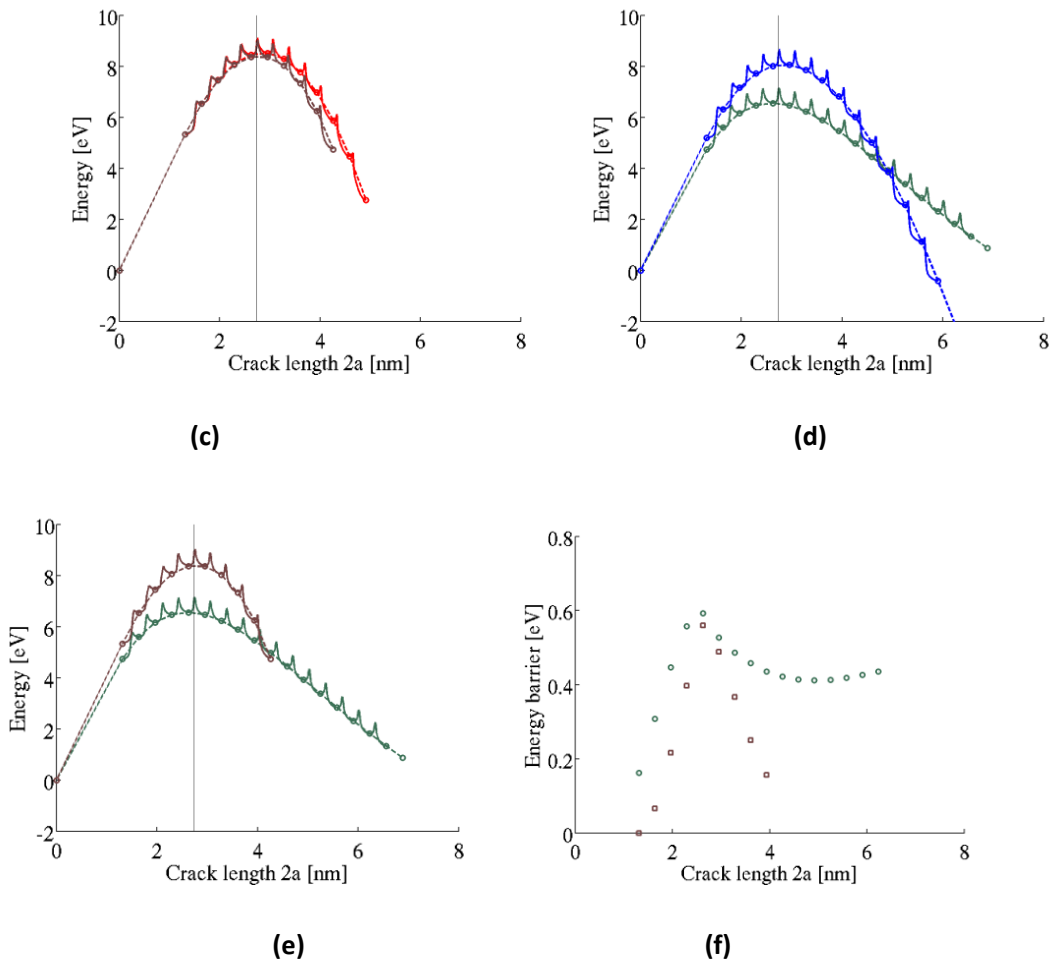

Figure 1. (cont.). (c) Size effect on stress-controlled fracture, showing the energetics of crack in the supercells of 18.3x20.1x3.8nm (red) and 9.1x10.1x3.8nm (brown). (d) Size effect on strain-controlled fracture, showing the energetics of crack in the supercells of 18.3x20.1x3.8nm (blue) and 9.1x10.1x3.8nm (green). (e-f) Same as (a-b) except the supercell is reduced by half in both width and height

Figure 1 also reveals the size effect on nanoscale fracture. In *Figure* 1(c), we compare the energies governing the stress-controlled fracture in two supercells, $18.3\text{nm} \times 20.1\text{nm}$ **(red curve) and** $9.1\text{nm} \times 10\text{nm}$ **(brown curve). *Figure* 1(d) shows the energetics of strain-controlled fracture in two supercells,** $18.3\text{nm} \times 20.1\text{nm}$ **(blue curve) versus** $9.1\text{nm} \times 10\text{nm}$ **(green curve). Comparing *Figure* 1(c) and 1(d), one sees a significant size effect on strain-controlled fracture, whereas stress-controlled fracture is not sensitive to the system size.**

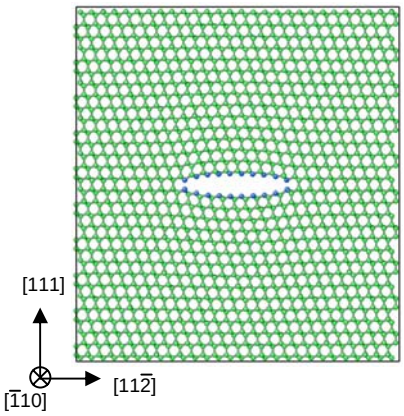

(g)

Figure 1. (cont) (g) Relaxed atomic configuration with a nanocrack at the critical length of Griffith's fracture, $2a_c \approx 3$nm; the supercell size is 9.1x10.1x3.8nm and the corresponding energetics of fracture is shown in (e-f).

To further reveal the effects of loading method and system size, we regroup the curves in Figs. 1(c) and (d), and show in *Figure* 1(e) the energies of stress-controlled (brown) and strain-controlled (green) fracture in the size-reduced system ($9.1\text{nm}\times 10\text{nm}$). In contrast to *Figure* 1(a), the two loading methods lead to considerably different energy curves. This difference arises because the strain-controlled fracture is more sensitive to the system size. *Figure* 1(f) shows the energy barriers of crack extension, extracted from *Figure* 1(e). Particularly, when $a > a_c$, the energy barrier for strain-controlled fracture (green circles) first decreases and then increases as the crack further extends. This trend differs qualitatively from the case when the system size is doubled, see *Figure* (b) (blue circles). This change in energy barriers can be correlated to the thermodynamic driving force of crack extension, i.e., $G(a)-2\gamma_s$ [95], which corresponds to the negative of the slope of the envelope curve in *Figure* 1(e). Specifically, during the strain-controlled fracture and when $a > a_c$, our calculations show that the system stress σ decreases when *a* increases. As the crack extends, the effect of σ on reducing $G=\sigma^2\pi a/E'$ overrides that of crack length *a* on increasing G, causing a net decrease in G and hence an increase in the energy barrier. The implication of this result is that crack extension can be kinetically delayed for a long crack; namely, the kinetic rate of crack growth decreases with the

increasing crack length. Our results demonstrate that such kinetic delay can be enhanced by reducing the system size.

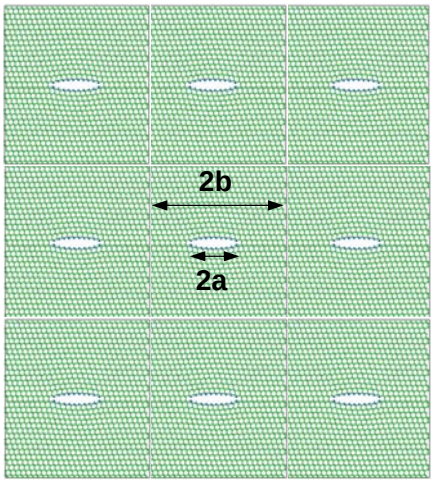

Figure 2. Illustration of the size effect on fracture, which arises because the crack in the central supercell (same as *Figure* 1(f)) interacts with image-cracks in other supercells.

The above size effect can be rationalized in terms of the interactions between the central crack and its images, which arise due to the finite size of the simulation cell and periodic boundary conditions. *Figure* 2 shows the central supercell, with the characteristic size of 2*b*, and eight neighboring cells. When *b* is reduced, the central crack and its image-cracks become closer, causing stronger interactions leading to the observed size effect. To evaluate the extent of size effect, we have further studied larger supercells. For example, in a size-doubled system ($37\text{nm} \times 40\text{nm}$), we find that for both the stress-controlled and strain-controlled fractures, the energy curves are close to those in Fig.1(a-b) with differences less than 1%. This suggests that the size effect on nanoscale fracture should become insignificant when *b*/*a* > 10 (Zhang et al., 2007). In other words, the size effect on the formation of nanocrack becomes increasingly important as the samples size is reduced into the range of tens of nanometers. It should be emphasized that such a nanoscale size effect is sensitive to the loading (boundary) conditions, as shown in *Figure* 1.

From the above image-crack considerations, one may estimate the influence of system size on the stress intensify factor, *K*, which is an effective measure of the thermodynamic driving force of

crack extension. Consider a periodic array of cracks of length 2*a* and spacing 2*b* under a far field stress of σ^{∞} . It can be shown the corresponding $K = \sigma^{\infty}\sqrt{\pi a}\cdot\sqrt{(2b/\pi a)\tan(\pi a/2b)}$ [103]. When $b/a = 10$, $K = 1.004\cdot\sigma^{\infty}\sqrt{\pi a}$. This supports the notation that the size effect on fracture should become insignificant when *b/a* > 10.

We next explain why the strain-controlled fracture has a stronger size effect than the stress-controlled fracture when *b/a* < 10. For a large system subjected to strain loading, the elastic energy release with the introduction of a crack of length 2*a* is $\pi\sigma^{\infty 2}a^2/E'$ per unit thickness of the body [102]. This energy relation is derived by assuming that σ^{∞} is constant when a crack is introduced, a condition that is approximately satisfied for strain-controlled fracture when the system size is much larger than the crack length. Our calculations show that the system stress becomes very sensitive to crack length when *b/a* < 10, so that the elastic energy release should deviate from $\pi\sigma^{\infty 2}a^2/E'$ in small samples, leading to a strong size effect, as shown in *Figure* 1(d). On the other hand, in a large system under stress loading, the introduction of a crack of length 2*a* causes a release of the potential energy (the sum of stored elastic energy and the work of applied stress) by the same amount of $\pi\sigma^{\infty 2}a^2/E'$ as the strain-controlled fracture. In small systems, σ^{∞} remains constant regardless of crack length, so that the energy release is still about $\pi\sigma^{\infty 2}a^2/E'$. This leads to a much weaker size effect, as shown in *Figure* 1(c). While the foregoing analysis of size effects is given based on the continuum theory of elasticity and does not directly involve the atomic-scale effect of lattice, it should be emphasized that the characterization of energy barriers requires the sampling of corrugated atomistic energy landscape, and the detailed atomistic study is therefore needed, as demonstrated in this work.

Finally, we note that the strain-controlled fracture in the present central-crack setting qualitatively differs in the nature of stability from another celebrated case of displacement-controlled fracture: Obreimoff's experiment of inserting a wedge to peel off a surface layer in mica [39]. As shown in *Figure* 1, a central-crack under a uniform far-field load features a concave energy-crack length profile for both the stress-controlled and strain-controlled loadings. Consequently, the crack system is unstable since both the extension and healing of a crack from $a = a_c$ lower the total energy of the system. In contrast, the energy-crack length profile that characterizes Obreimoff's experiment

is convex, much like an invert of what is shown in *Figure* 1(a), so that the crack system is stable. This difference in crack stability can be qualitatively understood as follows: for the central crack setting, the loads are applied by either the far-field stress σ^{∞} or strain $\varepsilon^{\infty} = \sigma^{\infty} / E'$. As detailed earlier, the introduction of a crack of length 2*a* in a large system causes a release of elastic energy or potential energy by the same amount of $\pi\sigma^{\infty 2} a^2 / E'$ for the stress-controlled or strain-controlled fractures. In the meantime, the surface energy is increased by $2a\gamma_s$. As a result, their energy-crack length profiles are both concave, and qualitatively similar even in small systems. On the other hand, the peel-off layer in Obreimoff's experiment can be modeled by one arm of a split strip. The arm can be treated as a beam of length *l* and height *h* cantilevered at the crack tip. Under an end load of imposed displacement δ, the stored elastic energy is about $E' h^3 \delta^2 / 4l^3$ per unit thickness of the beam, which is different from the stored potential energy of $-4l^3 P^2 / E' h^3$ under an end load of imposed force P [41]. As a result of the different roles of crack length *l* in the beam energy, the system energy versus crack length curve changes from the concave to convex shape as the applied load switches from imposed displacement to force, leading to the change of crack stability.

4.3. Competing mechanisms of fracture, dislocation emission, and amorphization

To investigate the atomic mechanisms governing the brittle-to-ductile transition, we have studied several competing unit processes at the crack tip. Consider, as an example, a crack under a strain-controlled load. Suppose the system is subjected to a nominal stress of $\sigma = 10\text{GPa}$ and the crack length is $2a = 2.8\text{nm}$, which satisfies the Griffith condition of fracture. *Figure* 3(a) shows the relaxed structure near the crack tip. Taking this configuration as an initial state, we determine the minimum energy paths of brittle fracture by bond breaking, *Figure* 3(b1), the ductile responses by amorphization, *Figure* 3(b2), and dislocation emission, *Figure* 3(b3). We obtain these local energy minima (Figs. 3(b1-b3)) by using the constrained energy minimization method, as detailed in Appendix A2. Since brittle fracture has been discussed in detail in section 2, we below describe the latter two processes.

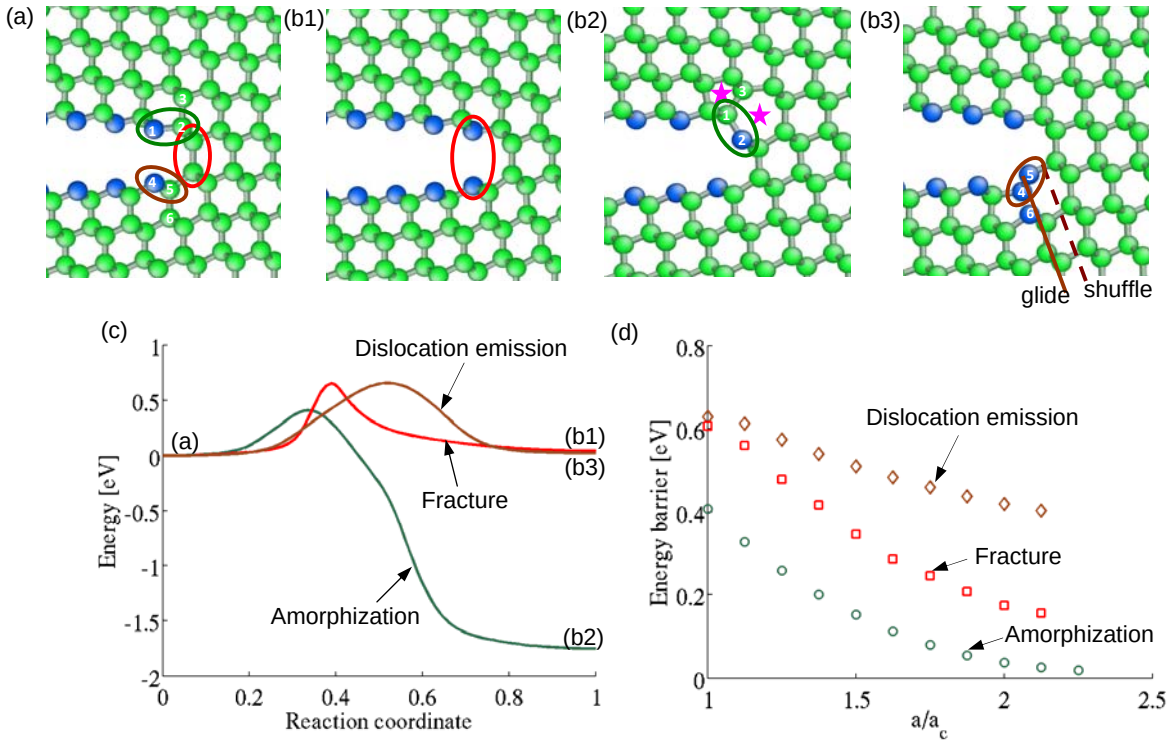

Figure 3. Competing crack-tip processes at the critical condition of Griffith's fracture. (a) The relaxed crack-tip structure before transition. (b1) Relaxed structures after crack-tip bond breaking, (b2) amorphization, (b3) and dislocation emission; atoms are colored by the coordination number: 4 (green) and 3 (blue). (c) Minimum energy paths. (d) Activation energy barrier versus crack length ($a > a_c$).

We next examine the atomic process of crack-tip amorphization. The minimum-energy-path calculation shows that the initiation of amorphization proceeds via the rotation of a single silicon bond, as marked by the green oval in *Figure* 3(a) and (b2), respectively. This bond rotation results in a pair of five- and seven-membered rings (stars in Fig.3 (b2)), in contrast to the six- and eight-membered rings in a perfect diamond-cubic structure. Such single bond rotation mechanism initiates the crack-tip amorphization process, as has been observed in direct MD simulations [36]. This mechanism has an important consequence on the energetics of amorphization to compete against fracture and dislocation emission, as will be discussed later in this article. Parenthetically, the unit process of bond rotation has been previously hypothesized as a fundamental mechanism of amorphization in bulk silicon, and employed to create the continuous random network of amorphous silicon, the so-called

WWW method [105]. It is also noteworthy that a similar bond-rotation mechanism leads to the formation of a Stone-Wales (SW) defect in the hexagonal lattice of carbon nanotubes and graphene sheets [106-108]. The SW defect is a pair of planar rings with five- and seven-members, which is also known as a 5/7 dislocation dipole. The separation of the dipole by dislocation migration is a mechanism underlying the plastic deformation of carbon nanotubes and graphene sheets. However, the SW-like defect in silicon is non-planar; it leads to amorphization rather than dislocation nucleation.

For the diamond-cubic silicon, the crack-tip dislocation nucleation on the $\{111\}$ plane involves two possibilities: dislocation glides on the widely-spaced shuffle plane, which cuts through single covalent bonds along the $\langle 111 \rangle$ direction, or on the narrowly-spaced glide plane, which cuts through the triplets of covalent bonds inclined equally to the $\{111\}$ plane; *Figure* 3(b3) shows the glide and shuffle plane by the solid and dashed line, respectively. As the relative importance of the shuffle and glide dislocations in plasticity has not been fully resolved [109-110], we study in this work the nucleation of a $\{111\}\langle 11\bar{2} \rangle$ glide partial as a representative unit-process to compete against fracture and amorphization. By comparing *Figure* 3(a) and (b3), one sees the bond shearing process (marked by the brown oval) on the $\{111\}$ glide plane (the solid line) in the $\langle 11\bar{2} \rangle$ direction. Note that this partial nucleation process involves not only the bond shearing between atom 4 and 5, but also the bond breaking between atom 5 and 6; the consequent effect on the energetics of nucleation is discussed next.

Figure 3(c) shows the minimum energy paths of the three competing processes. Here we take the energy of the relaxed structure in *Figure* 3(a) as a References of zero energy. It can be seen that the initiation of amorphization is most favored both thermodynamically (with the lowest energy of the final state) and kinetically (with the lowest activation energy barrier). By comparing the structure before transition, *Figure* 3 (a), with those after transition, Figs. 3 (b1-b3), one can rationalize the thermodynamic pReferences to amorphization in terms of the number of silicon bonds, which is conserved after bond rotation (switching). In contrast, both fracture and dislocation emission involves bond breaking, as evidenced by the increased number of under-coordinated (blue) atoms. As a result,

the latter two processes are subjected to a larger energy penalty, raising the energy level of the final states.

Figure 3(d) shows the energy barriers of the three processes at various crack lengths. Generally, the brittle-to-ductile transition of fracture requires the crossover of barrier curves between the competing crack-tip processes. However, for this model of silicon based on the SW potential, it can be seen that amorphization is always the most kinetically favorable mode with the lowest activation energy barrier, until the load is increased to the athermal limit of spontaneous amorphization giving a vanishing energy barrier. According to transition state theory [48] and assuming that the three processes have approximately the same trial frequency (because each process similarly involves the transformation of a single bond), amorphization is expected to be the dominant crack-tip response at various stresses, temperatures and loading rates, as observed in MD simulations using the same potential [22]. Here, it should be pointed out that different interatomic potentials of silicon have been compared for predicting the mechanical properties [33,49-50]. Results showed that whereas these empirical potentials facilitate the simulations in much larger systems with realistic microstructures compared to the *ab initio* method, they all have issues in characterizing the defective states of crystalline and amorphous structures of silicon. The improved fitting formalism and method are needed.

4.4. Evolving processes of amorphization and dislocation emission

We have further investigated the crack-tip amorphization beyond the initial formation of a pair of five- and seven-membered rings. Competing pathways are identified for evolving the crack-tip amorphous structure. Starting from the incipient amorphous state shown in *Figure* 3(b2), but at a slightly increased stress of 12GPa, we find amorphization can proceed through the separation of existing five- and seven-membered rings by migration along the upper crack surface, *Figure* 4(a1) → (a2) → (a3). In addition, we have identified an alternative pathway of amorphization, *Figure* 4(a1) → (a2) → (a4). *Figure* 4(a4) shows that a new pair of five- and seven-membered rings (blue diamonds) forms shortly after the first pair (pink stars) is separated. In *Figure* 4(b), we plot the minimum energy paths of these two competing pathways. Of particular interest is that compared to the transition from (a2) to (a3), going from (a2) to (a4) leads to a larger energy decrease, thus giving a stronger

thermodynamic driving force. But the latter mechanism has a higher energy barrier, so that the kinetic rate could be lower if assuming the trial frequency is approximately the same for the two competing processes.

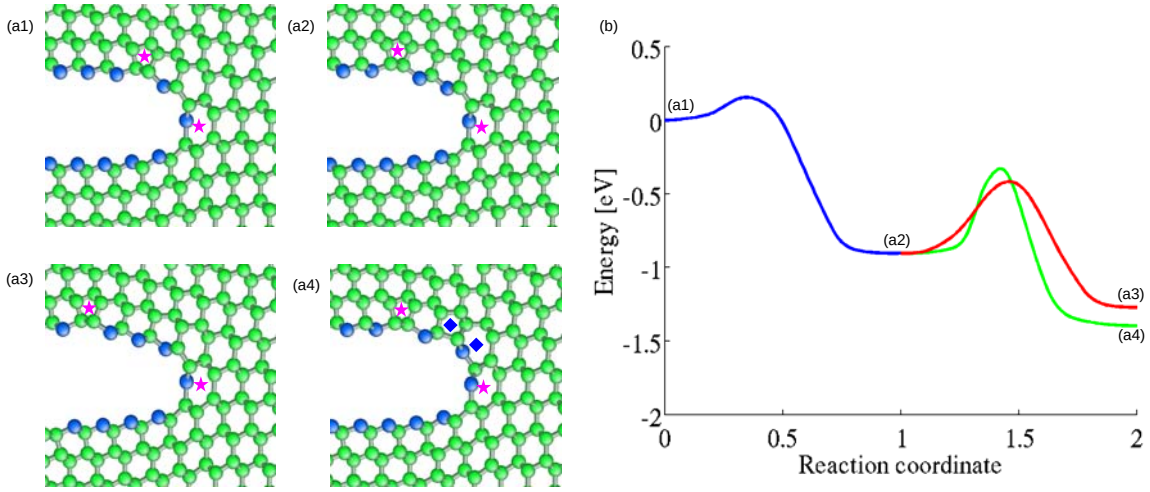

Figure 4. Crack-tip amorphization beyond the first step of formation of a pair of five and seven-membered rings. Two competing pathways are identified. (a1) → (a2) → (a3): separation of a pair of five and seven-membered rings (pink stars). (a1) → (a2) → (a4): formation of a new pair of five and seven-membered rings (blue diamonds). (b) Minimum energy paths of the two pathways.

(a) (b) (c)

(a)

(b)

Figure 5. Dislocation emission beyond the first step of forming a crack-tip glide partial: (a) zoom-out view of *Figure* 2(b3); (b) a partial glides into the crystal along the inclined $\{111\}$ slip plane; the dislocation cores are circled. (c) MEPs from state (a) to (b).

The foregoing two pathways of amorphization demonstrate a general feature of inelastic deformation in silicon: accommodating the applied load through the competing and complementary processes of *migration* of existing topological defects (e.g., the five- and seven-membered rings) and *nucleation* of the new ones. Such competition is expected to be important for most covalent solids such as silicon, where the intrinsic lattice resistance is high, causing the sluggish motion of existing defects whose back stresses promote the nucleation of new defects to sustain large deformation [51]. The sluggish motion of defects can be further demonstrated by finding the non-negligible secondary barriers on the energy landscape. As an example, *Figure* 5 shows the minimum energy paths of nucleation and migration of a glide partial from the crack tip. It is seen that the saddle point of the second step has the highest energy, which should act as the rate-limiting step of crack-tip dislocation nucleation.

Altogether, the present study shows that detailed analyses are further needed to fully understand the competing role of nucleation and migration of defects in silicon in terms of the thermodynamic driving force and kinetic barrier. These competing processes dictate the crack-tip stress relaxation, thereby controlling the brittle-to-ductile transition. A quantitative characterization of these processes is also critical to the coarse-grained modeling of the time-dependent crack growth by e.g., the kinetic Monte Carlo or cohesive finite element method [52].

4.5. Concluding remarks

We have studied the sub-critical fracture at the nanometer scale. As shown in *Figure* 1, the influence of boundary conditions is quantified in terms of both the thermodynamic driving forces (energy difference between adjacent local energy minima (circles)) and kinetic barriers (energy difference between saddle points and neighboring local energy minima). We find the strain-controlled fracture depends sensitively on the system size, leading to an intriguing scenario of kinetically delayed fracture with reduced system size. Moreover, the lattice trapping effect enables us to perform an atomistic analysis of the geometry and energetics of competing crack-tip processes, including cleavage

bond breaking, dislocation emission, and amorphization. We demonstrate that amorphization by single bond rotation is the most favorable atomic process until the athermal limit, making the brittle-to-ductile transition less likely.

Obviously, in view of the imprecision of force-field models, verification via first principles calculations is needed to ascertain the conclusion. However, our studies also reveal the complexity of the energy landscape that is associated with subsequent growth of amorphization. To lay the groundwork for first principles calculations, such molecular mechanics studies are insightful. Further, it should be noted that at elevated temperatures, all the three crack extension mechanisms may be active, leading to a complicated, coupled crack extension process. Nevertheless, the present study represents the first necessary step towards a mechanistic understanding of the brittle-to-ductile transition of fracture. The atomistic modeling along the lines presented here is now feasible for characterizing the brittle versus ductile responses in different material systems, as well as the time-dependent kinetic crack growth caused by, for example, the cyclic-loading [53] or chemical attack of foreign molecules [54-55].

References

1. **Chan, C.K., et al., *High-performance lithium battery anodes using silicon nanowires.* Nature Nanotechnology, 2008. 3(1): p. 31-35.**
2. **Chevrier, V.L. and J.R. Dahn, *First Principles Studies of Disordered Lithiated Silicon.* Journal of the Electrochemical Society, 2010. 157(4): p. A392-A398.**
3. **Cui, L.F., et al., *Crystalline-Amorphous Core-Shell Silicon Nanowires for High Capacity and High Current Battery Electrodes.* Nano Letters, 2009. 9(1): p. 491-495.**
4. **Ishikawa, M., et al., *Pure ionic liquid electrolytes compatible with a graphitized carbon negative electrode in rechargeable lithium-ion batteries.* Journal of Power Sources, 2006. 162(1): p. 658-662.**
5. **Liang, M.H. and L.J. Zhi, *Graphene-based electrode materials for rechargeable lithium batteries.* Journal of Materials Chemistry, 2009. 19(33): p. 5871-5878.**
6. **Wang, D.H., et al., *Self-Assembled TiO2-Graphene Hybrid Nanostructures for Enhanced Li-Ion Insertion.* Acs Nano, 2009. 3(4): p. 907-914.**
7. **Limthongkul, P., et al., *Electrochemically-driven solid-state amorphization in lithium-silicon alloys and implications for lithium storage.* Acta Materialia, 2003. 51(4): p. 1103-1113.**
8. **Graetz, J., et al., *Nanocrystalline and thin film germanium electrodes with high lithium capacity and high rate capabilities.* Journal of the Electrochemical Society, 2004. 151(5): p. A698-A702.**
9. **Yu, M.F., et al., *Strength and breaking mechanism of multiwalled carbon nanotubes under tensile load.* Science, 2000. 287(5453): p. 637-640.**
10. **Belytschko, T., et al., *Atomistic simulations of nanotube fracture.* Physical Review B, 2002. 65(23): p. 235430.**
11. **Peng, B., et al., *Measurements of near-ultimate strength for multiwalled carbon nanotubes and irradiation-induced crosslinking improvements.* Nature Nanotechnology, 2008. 3: p. 626-631.**
12. **Lee, C., et al., *Measurement of the elastic properties and intrinsic strength of monolayer graphene.* Science, 2008. 321(5887): p. 385-388.**
13. **Han, X.D., et al., *Low-temperature in situ large-strain plasticity of silicon nanowires.* Advanced Materials, 2007. 19(16): p. 2112-2118.**
14. **Pugno, N.M. and R.S. Ruoff, *Quantized fracture mechanics.* Philosophical Magazine, 2004. 84(27): p. 2829-2845.**
15. **Khare, R., et al., *Coupled quantum mechanical/molecular mechanical modeling of the fracture of defective carbon nanotubes and graphene sheets.* Physical Review B, 2007. 75(7): p. 075412.**
16. **Zhang, S.L., et al., *Mechanics of defects in carbon nanotubes: Atomistic and multiscale simulations.* Physical Review B, 2005. 71(11): p. 115403.**
17. **Mielke, S.L., T. Belytschko, and G.C. Schatz, *Nanoscale fracture mechanics.* Annual Review of Physical Chemistry, 2007. 58: p. 185-209.**
18. **Ritchie, R.O., et al., *Characteristic dimensions and the micro-mechanisms of fracture and fatigue in 'nano' and 'bio' materials.* International Journal of Fracture, 2004. 128(1-4): p. 1-15.**
19. **Celarie, F., et al., *Glass breaks like metal, but at the nanometer scale.* Physical Review Letters, 2003. 90(7): p. 075504.**

20. **Guin, J.P. and S.M. Wiederhorn, *Fracture of silicate glasses: Ductile or brittle?* Physical Review Letters, 2004. 92(21): p. 215502.**
21. **Gao, H.J., et al., *Materials become insensitive to flaws at nanoscale: Lessons from nature.* Proceedings of the National Academy of Sciences of the United States of America, 2003. 100(10): p. 5597-5600.**
22. **Bernstein, N. and D.W. Hess, *Lattice trapping barriers to brittle fracture.* Physical Review Letters, 2003. 91(2): p. 025501.**
23. **Perez, R. and P. Gumbsch, *An Ab initio study of the cleavage anisotropy in silicon.* Acta Materialia, 2000. 48(18-19): p. 4517-4530.**
24. **Perez, R. and P. Gumbsch, *Directional anisotropy in the cleavage fracture of silicon.* Physical Review Letters, 2000. 84(23): p. 5347-5350.**
25. **Zhang, S.L., T. Zhu, and T. Belytschko, *Atomistic and multiscale analyses of brittle fracture in crystal lattices.* Physical Review B, 2007. 76(9): p. 094114.**
26. **Voter, A.F., F. Montalenti, and T.C. Germann, *Extending the time scale in atomistic simulation of materials.* Annual Review of Materials Research, 2002. 32: p. 321-346.**
27. **Jonsson, H., G. Mills, K. W. Jacobsen, *Nudged elastic band method for finding minimum energy paths of transitions* In B. J. Berne, G. Ciccotti, and D. F. Coker, editors, Classical and Quantum Dynamics in Condensed Phase Simulations, 1998: p. 385–404.**
28. **Thomson, R., C. Hsieh, and V. Rana, *Lattice trapping of fracture cracks.* Journal of Applied Physics, 1971. 42(8): p. 3154-&.**
29. **Rice, J.R., *Thermodynamics of quasi-static growth of Griffith cracks.* Journal of the Mechanics and Physics of Solids, 1978. 26(2): p. 61-78.**
30. **Curtin, W.A., *On Lattice Trapping of Cracks.* Journal of Materials Research, 1990. 5(7): p. 1549-1560.**
31. **Sinclair, J.E., *Influence of interatomic force law and of kinks on propagation of brittle cracks.* Philosophical Magazine, 1975. 31(3): p. 647-671.**
32. **Zhu, T., J. Li, and S. Yip, *Atomistic configurations and energetics of crack extension in silicon.* Physical Review Letters, 2004. 93: p. 205504.**
33. **Zhu, T., J. Li, and S. Yip, *Atomistic characterization of three-dimensional lattice trapping barriers to brittle fracture.* Proceedings of the Royal Society of London, 2006. A462: p. 1741-1761**
34. **Warner, D.H., W.A. Curtin, and S. Qu, *Rate dependence of crack-tip processes predicts twinning trends in f.c.c. metals.* Nature Materials, 2007. 6: p. 876–881.**
35. **Stillinger, F.H. and T.A. Weber, *Computer-simulation of local order in condensed phases of silicon.* Physical Review B, 1985. 31(8): p. 5262-5271.**
36. **Buehler, M.J., et al., *Threshold crack speed controls dynamical fracture of silicon single crystals.* Physical Review Letters, 2007. 99(16): p. 165502.**
37. **Parrinello, M. and A. Rahman, *Polymorphic transitions in single-crystals - A new molecular-dynamics method.* Journal of Applied Physics, 1981. 52(12): p. 7182-7190.**
38. **Marder, M., *Energies of a kinked crack line.* Journal of Statistical Physics, 1998. 93(3-4): p. 511-525.**
39. **Lawn, B., *Fracture of Brittle Solids*. 2nd ed. 1993, Cambridge, UK: Cambridge University Press.**
40. **Rice, J.R., *Mathematical Analysis in the Mechanics of Fracture*, in *Fracture: An Advanced Treatise (Vol. 2, Mathematical Fundamentals)*, H. Liebowitz, Editor. 1968, Academic Press, N.Y. p. 191-311.**
41. **Freund, L.B., *Dynamic Fracture Mechanics*. 1990, Cambridge, UK: Cambridge University Press.**

42. **Wooten, F., K. Winer, and D. Weaire, *Computer-generation of structural models of amorphous Si and Ge.* Physical Review Letters, 1985. 54(13): p. 1392-1395.**
43. **Yakobson, B.I., *Mechanical relaxation and "intramolecular plasticity" in carbon nanotubes.* Applied Physics Letters, 1998. 72(8): p. 918-920.**
44. **Dumitrica, T., M. Hua, and B.I. Yakobson, *Symmetry-, time-, and temperature-dependent strength of carbon nanotubes.* Proceedings of the National Academy of Sciences of the United States of America, 2006. 103(16): p. 6105-6109.**
45. **Zhang, S. and T. Zhu, *Atomic geometry and energetics of carbon nanotube necking.* Philosophical Magazine Letters, 2007. 87(8): p. 567-574.**
46. **Sun, Y.M., G.E. Beltz, and J.R. Rice, *Estimates from atomic model of tension shear coupling in dislocation nucleation from a crack-tip.* Materials Science and Engineering A, 1993. 170(1-2): p. 67-85.**
47. **Bulatov, V.V., et al., *Parameter-free modelling of dislocation motion: the case of silicon.* Philosophical Magazine A, 2001. 81(5): p. 1257-1281.**
48. **Vineyard, G.H., *Frequency factors and isotope effects in solid state rate processes.* Journal of Physics and Chemistry of Solids, 1957. 3(1-2): p. 121-127.**
49. **Balamane, H., T. Halicioglu, and W.A. Tiller, *Comparative-study of silicon emipirical interatomic potentials.* Physical Review B, 1992. 46(4): p. 2250-2279.**
50. **Kang, K. and W. Cai, *Brittle and ductile fracture of semiconductor nanowires - molecular dynamics simulations.* Philosophical Magazine, 2007. 87: p. 2169-2189.**
51. **Argon, A.S., *Mechanics and physics of brittle to ductile transitions in fracture.* Journal of Engineering Materials and Technology-Transactions of the ASME, 2001. 123(1): p. 1-11.**
52. **Serebrinsky, S., E.A. Carter, and M. Ortiz, *A quantum-mechanically informed continuum model of hydrogen embrittlement.* Journal Of The Mechanics And Physics Of Solids, 2004. 52(10): p. 2403-2430.**
53. **Muhlstein, C.L., E.A. Stach, and R.O. Ritchie, *A reaction-layer mechanism for the delayed failure of micron-scale polycrystalline silicon structural films subjected to high-cycle fatigue loading.* Acta Materialia, 2002. 50(14): p. 3579-3595.**
54. **Zhu, T., et al., *Stress-dependent molecular pathways of silica-water reaction.* Journal of the Mechanics and Physics of Solids, 2005. 53(7): p. 1597-1623.**
55. **Ogata, S., et al., *Environmental effects of H2O on fracture initiation in silicon: A hybrid electronic-density-functional/molecular-dynamics study.* Journal Of Applied Physics, 2004. 95(10): p. 5316-5323.**

5. NANOSCALE FRACTURE MECHANISMS IN GRAPHENE AND TAILORING THE SIZE TO AVERT FRACTURE

5.1 Nanoscale fracture mechanisms in graphene

A study on the fracture mechanisms in graphene has also been performed. Experiments [1-3] and theoretical studies [4-10] on carbon nanotubes (CNTs), the rolled counterpart of graphene, have suggested that the deformation of the sp^2 carbon structures at high loads may take two *distinct* routes: cleavage brittle fracture or plastic flow, with active mechanisms mediated by temperature. At low temperatures, brittle fracture *via* bond breaking, which often involves strain-mediated formation of large open-ring structures [6], prevails. At elevated temperatures, however, plastic deformation dominates. The latter proceeds by nucleation and motion of Stone–Wales (SW) defects [11], a 5/7–7/5 dislocation dipole formed via rotation of a C–C bond by about 90^o. Recent experiments at high temperatures (~2000 ^oC) showed significant elongation and necking of stretched CNTs, providing strong experimental evidence for the SW-mediated plastic behavior. Nucleation of SW defects may also be promoted by tensile strain. *ab initio* studies showed that homogeneous nucleation of SW defects becomes energetically favorable when the tensile strain exceeds ~5-6% for armchair tubes [7,12] and ~12% for zigzag tubes [128]. It was also predicted that tensile strain also lowers the kinetic barrier for the nucleation of SW defects and subsequent 5/7 dislocation gliding.

To model a long crack that extends self-similarly in model I loading, we adopt a size-reduced model consisting of a small circular-shaped domain cut from a crack tip, as shown in *Figure* 1. The domain size is chosen such that its outer boundary falls in the *K*-dominant zone. . For the initial configuration, all the atoms in the graphene sheet are positioned according to the crack-tip asymptotic solution at the specified stress intensity factor K_I^{app} (where the subscript superscript denotes mode-I loading) with the origin at the center of the sheet (shown in *Figure* 1):

$$\begin{Bmatrix} u_x \\ u_y \end{Bmatrix} = \frac{K_I^{\text{app}}}{2\mu}\sqrt{\frac{r}{2\pi}}\left(\kappa - \cos\theta\right)\begin{Bmatrix} \cos(\theta/2) \\ \sin(\theta/2) \end{Bmatrix} \qquad \textbf{(1)}$$

where r and θ are defined with the origin *O* being at the center of the first bond of the crack tip (not shown in *Figure* 1); μ is the shear modulus and $\kappa = (3-\nu)/(1+\nu)$.

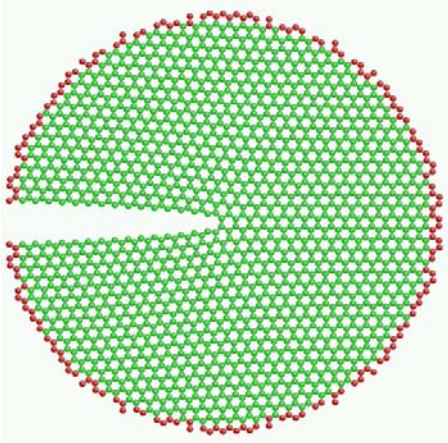

Figure 1. A size-reduced semi-infinite crack model in a monolayer graphene stressed by a local *K*-field. Atoms at the outer boundary (red) are held fixed, while the remaining atoms (green) are set free. The origin is set at the center of the first bond at the crack tip.

For a cracked monolayer graphene shown in *Figure* 2a (crack tip zoom-in view of *Figure* 1), besides the apparent cleavage fracture via crack-tip bond breaking (*Figure* 2b), another thermally active atomic mechanism in graphene sheet is bond-rotation induced plasticity. While bond rotation may occur for all the highly stretched bonds around the crack tip at elevated temperatures, we found that the rotating the bonds in the vicinity of the crack tip (indicated in *Figure* 2a by rotation arrows), is thermodynamically favorable, as suggested by a direct energy minimization at a relative high load. Rotating these two bonds forms two 5/7 dislocations (*Figure* 2c), each residing on one side of the crack surfaces and bridged by the crack-tip bond. We also found that rotating this specific bond is kinetically favorable than rotating any other bond in the system. We systematically compute the activation energy barriers (AEBs) for these two mechanisms at various loads near the Griffith load, thereby determining the kinetically favorable fracture mode.

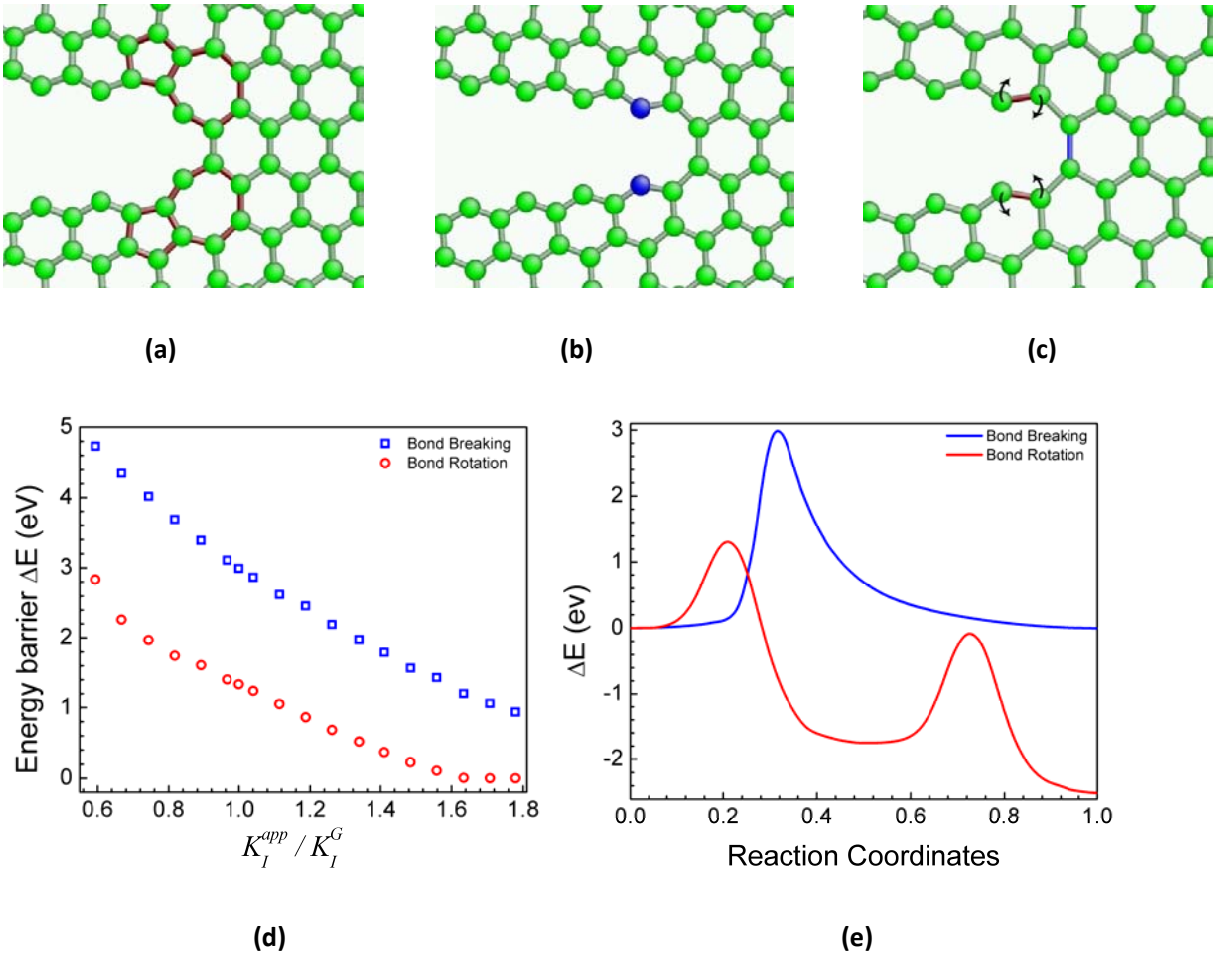

Figure 2. Kinetics of two competing atomic processes at the crack tip. Event (a)→(b): crack extension by cleavage bond breaking at the crack tip. Event (a) → (c): the red-colored bonds in *Figure* 2(a) are rotated by about 90°, forming a pair of 5/7 dislocations residing on each side of the crack surfaces and bridged by the crack-tip bond. (d) The minimum energy paths of the two competing mechanisms at the Griffith load clearly show that dislocation nucleation by bond rotation is both kinetically and energetically favorable. (e) Load-dependent activation energy barrier. For load range studied, the activation energy barrier for bond rotation is consistently 1-2eV lower.

From the transition state theory, these two fracture processes are "rare" events, which are not directly accessible to typical molecular dynamic (MD) simulations due to the time-scale constraints. To overcome the time-scale limitation of MD simulations, we perform reaction pathway sampling nudged elastic band (NEB) method to determine the minimum energy paths (MEPs) for

these two competing mechanisms. In our NEB calculations, the initial path is represented by 10 equally spaced intermediate replicas connected by elastic springs. Nudged relaxation of the elastic band via the projected velocity Verlet method yields a discrete MEP. For the 2D atomic monolayer, the MEP is a continuous path in a 2*N* dimensional configuration space (where *N* is the number of free atoms) among which the atomic forces are zero at any point in the 2*N*-1 dimensional hyperplane perpendicular to the path. The calculations are considered to be converged when the force on each replica perpendicular to the path is less than 0.05eV/Å. A continuous MEP is generated by polynomial fitting of the discrete MEP. AEBs against bond breaking (Fig 2 (a)→ (b)) and bond rotation (Fig 2 (a)→ (c)) can be then extracted for the saddle points on the MEPs.

Figure 2(d) plots the representative MEPs for these two competing mechanisms at the Griffith load, which clearly show that bond rotation is both energetically and kinetically favorable. In the MEP calculations, we treat the nucleation of the pair of dislocation as a sequential rather than a simultaneous barrier-overcoming process since the former is kinetically more feasible. Figure 2(e) plots the AEBs of these two mechanisms at various applied *K*-loads normalized by the Griffith load. In the load range studied, the AEBs for bond rotation are consistently 1-2eV lower than those for cleavage bond breaking. Therefore, bond rotation is kinetically favorable.

In conclusion, we show that the fracture of a monolayer graphene can involve an alternating sequence of bond rotation and bond breaking under the quasi-static loadings around the Griffith limit of fracture. Such a fracture mode is kinetically preferred. The presence of bond-rotation between two consecutive bond-breaking events delays the kinetic rate of fracture, but is unable to alter the brittle nature of the fracture of graphene at room temperature. The delay of crack extension is two-fold: besides the time duration involved in overcoming the dislocation nucleation between two consecutive bond breaking events, the presence of the dislocation pair causes an additional delay for each bond breaking because of the increased AEBs. The dislocation-mediated fracture mechanism sheds light on possible controllable modifications of monolayer graphene to achieve guided crack propagation.

5.2 Tailoring the size to avert fracture in strained graphene nanoribbons

The mechanical deformation and confinement effect by system size are the prospective methods to control the electronic properties of graphene nanoribbon through band-gap engineering. When these two methods are applied, mechanical stability can arise due to their interplay. Large deformation and/or system size may lead to fracture. In this section, we use the fracture mechanics approach to determine the strain limits for tuning the electric properties of graphene nanoribbons without fracture. Our study identifies a critical condition under which the mode I fracture in graphene could be suppressed.

5.2.1 Introduction

Graphene, a single layer of carbon atoms, is one of the most promising materials for electronic devices at nanoscale, due to its remarkable electronic properties [13-15]. In addition to being a good conductor, an exciting opportunity of graphene is that the high-performance electronic devices could be fabricated by using the band-gap engineered graphene [16-18].

To explore its applications in electronic devices, methods of controlling the energy band-gap have been studied from both the theoretical and experimental standpoints, including (i) mechanical deformation [19-22]; (ii) and confinement effect on the carriers by system size [17]. The interaction between the mechanical and electrical properties in graphene, or the so called strain engineering, has various applications [22-23]. It could transform a metallic nanotube into a semiconducting one or vice versa [24-26]. On the other hand, an experiment shows the confinement effect of carriers in a quasi-one-dimensional system (i.e., a graphene nanoribbon) could open the energy gap [17]. Conductance is reduced linearly by decreasing the size of graphene nanoribbons [17]. However, the mechanical stability often arises during the implementation of these methods, owing to the applied load and system size. Although recent research identifies pristine graphene as one of the strongest materials with the fracture strain up to 25% and nearly 1TGpa Young's modulus [27], the presence of cracks significantly reduces its tolerance of rupture [28-29]. Therefore, a study of the limits of these two methods is necessary for utilizing the unusual electronic properties of graphene.

The present section describes a method to determine the critical conditions, which can avert fracture during the tuning of graphene energy band-gap by tailoring the applied strain and/or system size. For the strained graphene with a pre-existing crack, further fracture would always be prevented

if the loading and geometrical conditions fall within the safe zone in our diagram. The result is consistent with existing experimental observations [30].

5.2.2 Model description

Our model is formulated in terms of fracture mechanics basing on the Griffith's criteria of fracture [145]. Crack-like defects are assumed to pre-exist in a square graphene nanoribbon. To tune the band gap, graphene dimension *d* and applied strain ε_{app} are used as control variables in experiments. We ask whether the pre-exist crack will cause fracture. The elastic energy in graphene will decrease when the crack length increases. The reduction of the elastic energy in a system normalized by unit area, which is the unit length in a 2D-system of graphene, is defined as the energy release rate,

$$G = Z\varepsilon_{app}^2 Y d \qquad (2)$$

where Y is Young's modulus, ε_{app} is applied strain and *d* is system size, *Z* is a dimensionless coefficient. Equation (2) indicates that *G* is proportional to *d* and to the square of ε_{app}. Along with the reduction of elastic energy, the surface energy increases with increasing crack length. The crack could not advance if

$$G \leq 2\gamma \qquad (3)$$

where γ is the edge energy, not surface energy since graphene is a 2D system. The competition between the energy release rate and the edge energy governs the cracking behavior. Since γ and Y are material constants, inequality (3) gives a critical condition relating the control variables ε_{app} and *d*:

$$\varepsilon_{app} \approx \sqrt{\frac{4}{Y}\frac{\gamma}{d}} \sim d^{-1/2} \qquad (4)$$

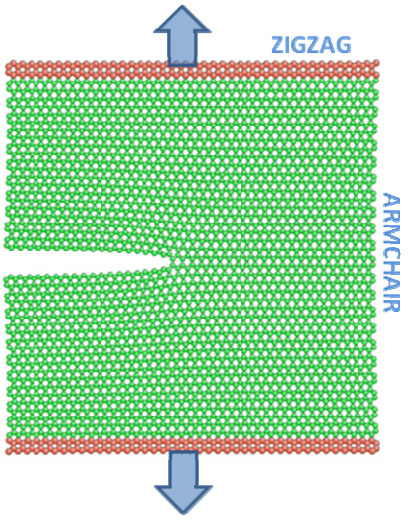

Figure 3. Nanoscale fracture in a 10nm×10nm graphene under 7% applied strain. Crack length is 4.5 nm. External strain is applied by fixing two layers of atoms at top and bottom (red ones).

To quantitatively examine the condition proposed in equation (4), atomistic simulation is implemented. Fifteen square graphene ribbons are calculated, ranging from 10nm×10nm (figure 3) to 24nm×24nm. The number of carbon atoms is from 4k to 20k. Each system is stretched by fixing two layers of atoms at the top and bottom (red atoms in figure 3). Strain is applied from 1% to 10%. The carbon atoms are connected by the localized and directional covalent bonds, which promotes the lattice trapping effect [32-33]. By utilizing this effect, we are capable of controlling the size of crack for energetic analysis. In each graphene ribbon, the carbon bonds along the crack path are broken one by one to generate the fractured structure until the athermal limit, where the energy barrier of breaking a bond is not big enough to trap the corresponding cracked configuration. The system energy at each crack length is calculated. Suppose the crack length a=x·a_0, and a_0 is the lattice spacing. Then the energy release rate G can be calculated according to:

$$G(a) = G(x \cdot a_0) \approx \frac{E_{xa_0} - E_{(x-1)a_0}}{a_0}, \quad x = 1, \ldots, \left\lfloor \frac{d}{a_0} \right\rfloor \qquad (5)$$

where E_{xa_0} is the system energy when the crack length is a=x·a_0.

In our simulations, an analytical bond-order potential is used to describe the covalent C-C interaction [34]. The Young's modulus and Poisson's ratio are 0.84TPa and 0.149, respectively [35],

within a reasonable range of the experimental data [27]. The predicted ideal strain of fracture is 30% for a zigzag oriented pristine graphene, which is comparable to the experimental result of 25% [27].

5.2.3 Results and discussion

In directional bonded materials, the crack extension typically involves different competing mechanisms [35-36]. A sequence of bond breaking and bond rotation at a crack tip are found during fracture of monolayer graphene [35]. The coexistence of these mechanisms will affect the edge energy density. In reality, edge energy density should involve the combined contributions from bond breaking and bond rotation. Since the work from bond breaking (~1eV) is much larger than the one from bond rotation (~0.1eV) [35], we just use the former as a first approximation. The edge energy density is 3.1J/m for the zigzag edge (figure1) and 3.5J/m for armchair. The lower edge energy density indicates a higher probability of cracking along the corresponding edge direction. Hence, we only consider the cracking along the zigzag edge here.

As shown in figure 4d, reducing the applied strain or system size will decrease the energy release rate. For a 20nm graphene under 5% applied strain (black line), the energy release rate is higher than the surface energy, indicating a thermodynamic pReferences of fracture extension. If we reduce the external strain to 4% (blue line), or change the system size to 16nm (green line), the maximum energy release rate will be reduced to below surface energy. Hence, under these conditions, a pre-crack will not extend, irrespective of crack length. This is consistent with equation (2) and inequality (3).

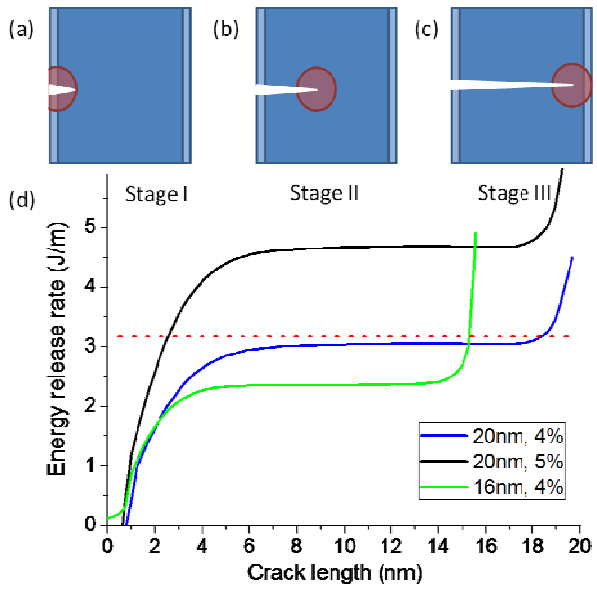

Figure 4. Curves of energy release rate. (d) Reduce system size *d* and square of applied strain ε_{app} will decrease energy release rate. (a)~(c) Consider crack extension is equivalent to move a stripe of material from system's right boundary to its left boundary. The three stages in curve energy release rate can be explained by crack-tip stress magnification.

In our results, the shape of every energy release rate curve can be divided into three stages (e.g. curves in figure 4d): (I) increase at the beginning, (II) remain nearly flat, and (III) increase again at the end. The three stages of *G* are understandable and illustrated in figure 4a~c. The extension of a crack could be considered as moving a stripe of material (strips in figure 4a~c) from the system's right boundary to its left. Then strain is relaxed and new surface is created. Because of the crack induced stress magnification, the density of strain energy is higher around the crack tip (red area in figure 4a~c). At stage one, the crack is small. After moving from the right boundary to the left boundary a part of "relaxed material" is still within the red area (figure 4a). The strain energy is not fully released and it yields a small *G*. Along with crack extension, the red portion in "relaxed" stripe decreases, more strain energy is relaxed, so that we observe an increase of energy release rate. In the second stage, no red area is involved. The plateau (figure 4b) arises because the strain energy release is ~$\varepsilon_{app}^2 Yd$, which is nearly constant. When the crack is so long that red area touches the right boundary of system, stage three is achieved (figure 4c). A stripe of material with the partially red area will be fully relaxed. Because the ratio of the red area in the strained stripe increases along with crack growth, the

energy release rate goes up. However, because the size of stage III is relatively small (on the order of a few a_0), we only consider stages I and II which dominate the energy release rate curve.

To show the limit on external conditions on applied ε_{app} and system size *d*, a phase diagram is plotted in figure5. ε_{app} changes from 2% to 8%, and L is from 10nm to 20nm. For each (ε_{app}, *d*), energy release rate curve as in figure 2d are calculated. Then the maximal energy release rate in stage I and II is picked out. If it's smaller than edge energy density, then we know that no matter of the length of a crack, it will always arrest and fracture will not happen. Hence, we say that particular (ε_{app}, *d*) is safe. If for certain (ε_{app}, *d*) the maximal energy release rate is larger than edge energy density, we classify it into unsafe area. The boundary between safe and unsafe areas is highlight by a bold contour curve in figure 5. At the boundary, the maximal energy release rate is equal to energy density of zigzag edge. With smaller applied strain ε_{app} or system size *d*, energy release rate reduces. It will be thermodynamically unfavorable to fracture. Hence the safe area is at the left-below corner. All the contour curves follows the relation reveal in equation (4) that applied strain is proportional to the inverse of square-root of system size: $\varepsilon_{app} \sim d^{-1/2}$. The difference between them is a scaling factor which depends on the parameter *G/Y*.

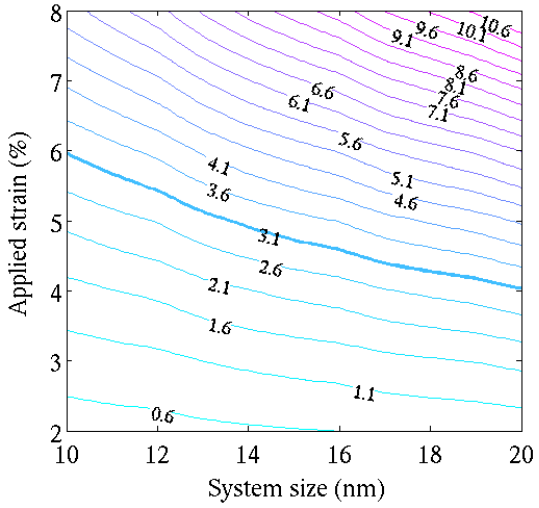

Figure 5. Map of maximal energy release rate contours. Crack will always arrest if the external condition of (ε_{app}, *d*) is below the critical boundary (bold blue line). Contour curves follow the relationship in equation (3) that $\varepsilon_{app} \sim d^{-1/2}$ with difference of a scaling parameter.

More generally, the relationship in equation (4) that $\varepsilon_{app} \sim d^{-1/2}$ is also applicable in metal shear band propagation. Similar to crack extension, a shear band can only propagate when the strain energy released by propagation is larger than the energy increment of shear band. For a metal cylinder with radius r, the strain energy reduction is $\pi r^2 \varepsilon_{app}^2 Yd/2$, and shear-band energy increases $\pi r^2 \Gamma$. Γ is shear band energy density. By analogy with crack propagation, the critical condition for shear band propagation is decided by $\pi r^2 \varepsilon_{app}^2 Yd/2 \approx \pi r^2 \Gamma$. Hence,

$$\varepsilon_{app} \approx \sqrt{\frac{2}{Y}\frac{\Gamma}{d}} \sim d^{-1/2} \qquad (5)$$

5.2.4 Concluding remarks

Our study reveals that it is possible to avert crack extension by tailoring the system size. A critical condition is given, under which the fracture could be suppressed. By using graphene as a model material, our theoretical analysis of the load and size effects is verified through atomistic simulations.

In addition, this work is useful for the band-gap engineering of graphene. The sample size and applied strain are control parameters for tuning the electrical properties of graphene in experiments. The critical condition given here represents the limit of tuning band gap without fracture.

References

1. **Huang, J.Y., et al., *Atomic-scale imaging of wall-by-wall breakdown and concurrent transport measurements in multiwall carbon nanotubes.* Physical Review Letters, 2005. 94(23).**
2. **Huang, J.Y., et al., *Superplastic carbon nanotubes - Conditions have been discovered that allow extensive deformation of rigid single-walled nanotubes.* Nature, 2006. 439(7074): p. 281-281.**
3. **Huang, J.Y., F. Ding, and B.I. Yakobson, *Dislocation dynamics in multiwalled carbon nanotubes at high temperatures.* Physical Review Letters, 2008. 1(3).**
4. **Terdalkar, S., J.J. Rencis, and S. Zhang, *Atomic fracture mechanisms of monolayer graphene.* 2008.**
5. **Zhang, S. and T. Zhu, *Atomic geometry and energetics of carbon nanotube necking.* Philosophical Magazine Letters, 2007. 87(8): p. 567-574.**
6. **Zhang, S.L., et al., *Mechanics of defects in carbon nanotubes: Atomistic and multiscale simulations.* Physical Review B, 2005. 71(11).**
7. **Nardelli, M.B., B.I. Yakobson, and J. Bernholc, *Brittle and ductile behavior in carbon nanotubes.* Physical Review Letters, 1998. 81(21): p. 4656-4659.**
8. **Dumitrica, T., T. Belytschko, and B.I. Yakobson, *Bond-breaking bifurcation states in carbon nanotube fracture (vol 118, pg 9485, 2003).* Journal of Chemical Physics, 2003. 119(2): p. 1281-1281.**
9. **Dumitrica, T., M. Hua, and B.I. Yakobson, *Symmetry-, time-, and temperature-dependent strength of carbon nanotubes.* Proceedings of the National Academy of Sciences of the United States of America, 2006. 103(16): p. 6105-6109.**
10. **Dumitrica, T. and B.I. Yakobson, *Strain-rate and temperature dependent plastic yield in carbon nanotubes from ab initio calculations.* Applied Physics Letters, 2004. 84(15): p. 2775-2777.**
11. **Stone, A.J. and D.J. Wales, *Theoretical-Studies of Icosahedral C60 and Some Related Species.* Chemical Physics Letters, 1986. 128(5-6): p. 501-503.**
12. **Zhang, P.H., P.E. Lammert, and V.H. Crespi, *Plastic deformations of carbon nanotubes.* Physical Review Letters, 1998. 81(24): p. 5346-5349.**
13. **Castro Neto, A.H., et al., *The electronic properties of graphene.* Reviews of Modern Physics, 2009. 81(1): p. 109-162.**
14. **Geim, A.K. and K.S. Novoselov, *The rise of graphene.* Nature Materials, 2007. 6(3): p. 183-191.**
15. **Geim, A.K., *Graphene: Status and Prospects.* Science, 2009. 324(5934): p. 1530-1534.**
16. **Barone, V., O. Hod, and G.E. Scuseria, *Electronic structure and stability of semiconducting graphene nanoribbons.* Nano Letters, 2006. 6(12): p. 2748-2754.**
17. **Han, M.Y., et al., *Energy band-gap engineering of graphene nanoribbons.* Physical Review Letters, 2007. 98(20).**
18. **Avouris, P., Z.H. Chen, and V. Perebeinos, *Carbon-based electronics.* Nature Nanotechnology, 2007. 2(10): p. 605-615.**
19. **Gui, G., J. Li, and J.X. Zhong, *Band structure engineering of graphene by strain: First-principles calculations.* Physical Review B, 2008. 78(7).**
20. **Guinea, F., M.I. Katsnelson, and A.K. Geim, *Energy gaps and a zero-field quantum Hall effect in graphene by strain engineering.* Nature Physics, 2010. 6(1): p. 30-33.**
21. **Pereira, V.M. and A.H.C. Neto, *Strain Engineering of Graphene's Electronic Structure.* Physical Review Letters, 2009. 103(4).**

22. **Cocco, G., E. Cadelano, and L. Colombo, *Gap opening in graphene by shear strain.* Physical Review B, 2010. 81(24).**
23. **Sazonova, V., et al., *A tunable carbon nanotube electromechanical oscillator.* Nature, 2004. 431(7006): p. 284-287.**
24. **Minot, E.D., et al., *Tuning Carbon Nanotube Band Gaps with Strain.* Physical Review Letters, 2003. 90(15): p. 156401.**
25. **Heyd, R., A. Charlier, and E. McRae, *Uniaxial-stress effects on the electronic properties of carbon nanotubes.* Physical Review B, 1997. 55(11): p. 6820.**
26. **Yang, L., et al., *Band-gap change of carbon nanotubes: Effect of small uniaxial and torsional strain.* Physical Review B, 1999. 60(19): p. 13874.**
27. **Lee, C., et al., *Measurement of the elastic properties and intrinsic strength of monolayer graphene.* Science, 2008. 321(5887): p. 385-388.**
28. **Zhao, H. and N.R. Aluru, *Temperature and strain-rate dependent fracture strength of graphene.* Journal of Applied Physics, 2010. 108(6).**
29. **Pugno, N.M. and R.S. Ruoff, *Quantized fracture mechanics.* Philosophical Magazine, 2004. 84(27): p. 2829-2845.**
30. **Volkert, C.A., A. Donohue, and F. Spaepen, *Effect of sample size on deformation in amorphous metals.* Journal of Applied Physics, 2008. 103(8).**
31. **Lawn, B.R., *Fracture of Brittle Solids.* 1993.**
32. **Zhu, T., J. Li, and S. Yip, *Atomistic characterization of three-dimensional lattice trapping barriers to brittle fracture.* Proceedings of the Royal Society a-Mathematical Physical and Engineering Sciences, 2006. 462(2070): p. 1741-1761.**
33. **Thomson, R., C. Hsieh, and V. Rana, *Lattice trapping of fracture cracks.* Journal of Applied Physics, 1971. 42(8): p. 3154-&.**
34. **Pettifor, D.G. and I.I. Oleinik, *Bounded Analytic Bond-Order Potentials for sigma and pi Bonds.* Physical Review Letters, 2000. 84(18): p. 4124.**
35. **Terdalkar, S.S., et al., *Nanoscale fracture in graphene.* Chemical Physics Letters, 2010. 494(4-6): p. 218-222.**
36. **Huang, S., et al., *Mechanics of nanocrack: Fracture, dislocation emission, and amorphization.* Journal of the Mechanics and Physics of Solids, 2009. 57(5): p. 840-850.**

6. ATOMISTIC MECHANISMS OF LITHIUM INSERTION IN AMORPHOUS SILICON

Understanding the lithium-silicon alloying behavior is essential to achieving maximum charge capacity in the negative electrodes of lithium-ion batteries. Our atomistic simulations show that in amorphous silicon with a disordered network structure, inserted lithium atoms can find equilibrium positions in the interstices of big rings. Alternatively, lithium is incorporated into the network by the destruction and reformation of smaller rings. These atomic-level mechanisms are characterized using the network topology measure of ring statistics, which are correlated to the lithiation responses of silicon electrodes. The results reveal the influence of lithium concentrations on the electro-chemical-mechanical behavior of silicon. Implications on the reversibility and dynamics of the lithiation process are discussed.

6.1. Introduction

Rechargeable lithium-ion batteries are currently the preferred form of electrical energy storage devices [1-2]. They can deliver high energy density (~210Whkg^{-1}; 650Whl^{-1}) with long life cycle. Their recent and potential applications include portable electronic devices, cordless power tools, and electric vehicles. Silicon is being considered as an anode material for Li-ion batteries because it has the highest known theoretical charge capacity (4,200mAhg^{-1}) [3-8].

However, Si anodes often suffer from pulverization and capacity fading. This is caused by the large volume changes of Si (~300%) upon Li insertion/extraction close to its theoretical charge/discharge limit. This issue is particularly significant when the Si electrodes are subject to high-rate charging or discharging, which is highly desirable but often induces a non-uniform distribution of Li in Si. The resulting large incompatible deformation between areas of different Li contents tends to initiate fracture, leading to the electro-chemical-mechanical failure of Si electrodes [9-11]. Are there new ways to optimize the charge capacity of Si anodes while preventing failures? To address this question, understanding the Li-Si alloying behavior is essential, requiring fundamental research that goes beyond empirical battery cell studies.

Metastable amorphous glass is formed when the crystallization of intermediate compounds is frustrated [73]. When reacted with Li, Si crystals yield solid-state amorphous phases at low temperature, but crystalline phases at high temperature (415°C) [12]. The formation of amorphous Li_xSi alloys, where *x* denotes the ratio of Li to Si, has been experimentally observed at room-temperature in the electrochemical reactions of Li with Si thin films [4], nanoparticles [5] and nanowires [6]. In principle, amorphous Li_xSi avoids the formation of coherent boundaries between coexisting crystalline phases of different Li concentrations. This can mitigate the buildup of incompatible strains (and thus internal stresses) in Si electrodes so as to improve the cycling performance of batteries. In addition, a variety of Si nanostructure morphologies has been explored to enable Si to perform well as anodes [5-7], as it is supposed that the nanometer size scale can facilitate strain relaxation, enhance flaw tolerance [13], shorten diffusion paths, and increase surface area of Si to better react with Li.

As a fundamental step towards understanding the Li-Si alloying behavior, here we report an atomic-level study of Li insertion in amorphous Si (*a*-Si). The structures and energetics of Li-Si alloys are computed quantum-mechanically by using the molecular orbital theory [159]. Detailed analyses of the ring geometry and statistics are related to various electro-chemical-mechanical characteristics of Li reactions with *a*-Si. They are found to depend sensitively on the local Li concentration. The results provide an atomistic basis for further study of the dynamic alloying processes and electrochemically-driven solid state amorphization between Li and Si.

6.2. Methods

The *a*-Si structures are generated from diamond-cubic Si crystal by using an activation-relaxation technique (ART) [15]. As a computationally efficient approach, ART focuses on simulating the activated events of escaping the basins of attraction in the energy landscape, i.e., they jump over the barriers that separate different local energy minima. ART can be used to avoid the bias on structural evolution that underpins the fast cooling rate in the melt-and-quench molecular dynamics method [16]. To speed up calculations, the *a*-Si structures are first created by using the empirical Stillinger-Weber [17] interatomic potential and then further relaxed by the Molecular Orbital PACkage (MOPAC 2009) with the AM1 method.

We adopt the protocols developed by Chevrier and Dahn [18-19] for modeling the lithium insertion and extraction. The lithium atoms are randomly inserted into *a*-Si one at a time until X = 4. After the insertion of each Li atom, the system is fully relaxed under periodic boundary conditions; this involves the relaxation of the internal atomic coordinate, supercell size and shape. The lithium extraction process is similarly modeled. Starting from pure *a*-Si, we have repeated the insertion-extraction cycle several times, and found that that the electro-mechanical responses of volume expansion and electrical potential will reach a steady state after about three cycles.

To determine the electrical potential, we note that neglecting the entropy contributions [18-19], the free energy of the system can be approximated by the potential energy, which is a function of atomic coordinates at zero temperature. Then the electrical potential of the Li_xSi structure vs Li/Li^+, in units of electron volts, is calculated by $V = -(dE_{LixSi}/dx - E_{Li})$, where is the potential energy of the Li_xSi structure divided by the number of Si atoms in the system, and E_{Li} is the energy of a single Li atom in amorphous Li. To obtain the average responses for comparison with experimental measurements, the potential and volume are averaged over the calculation results of six statistically independent *a*-Si structures at the respective steady states. The averaging method that we used is the Savitzky–Golay smoothing filter with the main advantage of preserving features of the distribution such as relative maxima, minima and width, which are usually 'flattened' by other techniques (like moving averages, for example) [20].

6.3. Results and discussion

The starting amorphous structure in our calculations has 20 Si atoms. The supercell volume is 428$Å^3$, corresponding to a typical density of *a*-Si, 2212 kg/m^3 [21]. While one would like to use a larger starting system, we note that after Li insertions, the amorphous Li_xSi alloy at its charging limit involves about four times more atoms. This limits the size of the starting state because of the computational cost associated with a large number of calculations, which are necessary for averaging the voltage-composition responses and for analyzing the statistics of amorphous states. To validate the use of such a small starting system, we have generated *a*-Si with various sizes, and verified that it well represents the bulk behavior in terms of providing similar structural characteristics of the short- and medium-range order. The former can be characterized by radial and angular distribution functions

(RDFs and ADFs), and the latter by ring statistics. As shown in *Figure* 1, RDF has a narrow nearest-neighbor peak, while the peak of ADF centers around 109°, characteristic of tetrahedral Si bonding. These features in RDF and ADF, which are consistent with previous modeling results [21-22], indicate that the local atomic environments of *a*-Si are similar to those of atoms in the crystalline phase, as typically found in the solid-like amorphous covalent structure with a continuous random network [17].

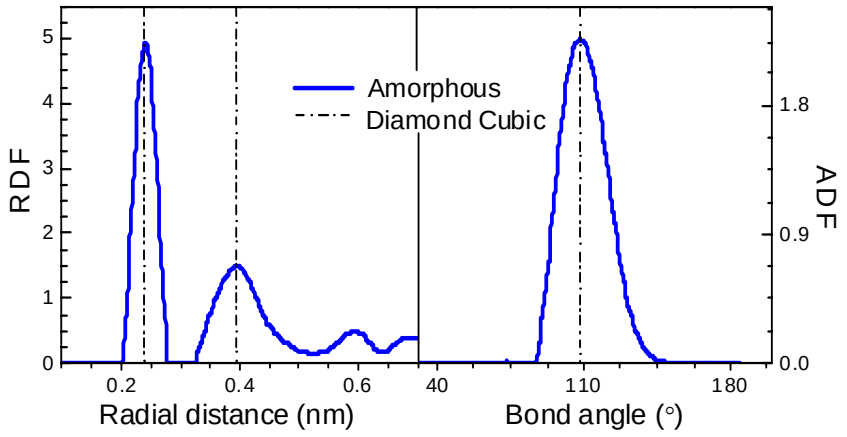

Figure 1. Comparison of the amorphous and diamond cubic crystals of Si based on radial and angular distribution functions (RDFs and ADFs).

The incorporation of Li into *a*-Si induces two kinds of structural changes that dominate at low and high Li concentrations, respectively: insertion in the interstitial hole of big rings and incorporation into the network by the destruction and reformation of small rings. We find that when the Li to Si ratio, *x*, is less than about 0.8, the added Li typically resides in the centers of the big rings after structural relaxation. This can be seen in *Figure* 2(a) and (b), showing an 8-membered ring of Si (highlighted in green) before and after the insertion of one Li (in red), respectively. In this case, the big Si ring encloses a large open space, and its center provides an energetically favorable interstitial site. After Li insertion, the Si-Si bonds in the ring belt do not break, but the Li atom forms new bonds with the surrounding Si atoms in the belt, causing a small adjustment of the ring geometry. Furthermore, the addition of this Li divides the big 8-membered ring into several smaller rings (three 3-membered,

one 4-membered and one 5-membered rings). Consequently, the fraction of big rings in the system decreases with increasing *x*.

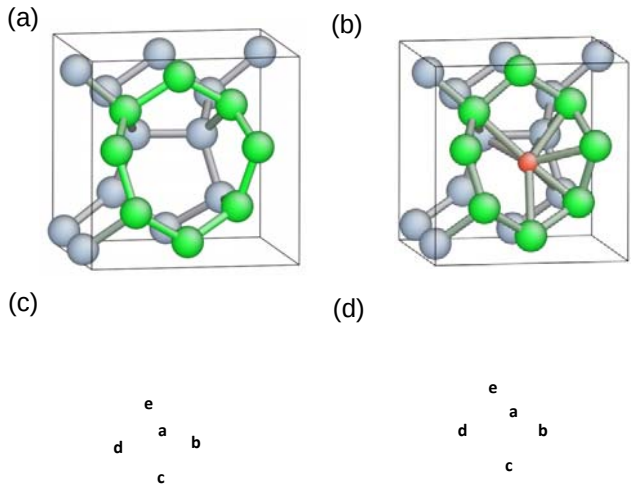

Figure 2. Atomic structures of lithiated *a*-Si. Large and small spheres represent Si and Li, respectively. (a) and (b) Before and after the interstitial insertion of a Li atom (red) in an 8-membered ring of Si when *x* = 0. (c) and (d) Incorporation of Li into the network through breaking bonds (in red) and reformation when *x* = 1.2.

Figures 2(c) and (d) show the representative structures before and after the addition of one Li atom (in red) when *x* > 0.8. Because of the paucity of big rings, the added Li has to typically react with surrounding small rings. It pushes the nearby atoms away so as to create a larger local free volume for its incorporation into the amorphous network. In conjunction with large atomic displacements of surrounding atoms, the local ring structure is reconfigured, involving both bond breaking and formation. For example, prior to the Li addition, the length of a homopolar bond between Li atoms *e* and *b* in *Figure* 2(c) is 2.69 Å. It is close to the equilibrium Li-Li bond length of 2.65 Å in the crystalline phase of $Li_{15}Si_4$ from density functional theory calculations [23]. With the addition of a Li atom (red) in *Figure* 2(d), both Li atoms *e* and *b* form new homopolar bonds with the inserted Li, while the bond between *b* and *e* is broken, with the separation increased to 4.05 Å. Evidently, the impact of Li

insertion on the local ring structure involves the destruction of one or a few small rings with the concomitant reformation of several similar sized (3 or 4-membered) small rings.

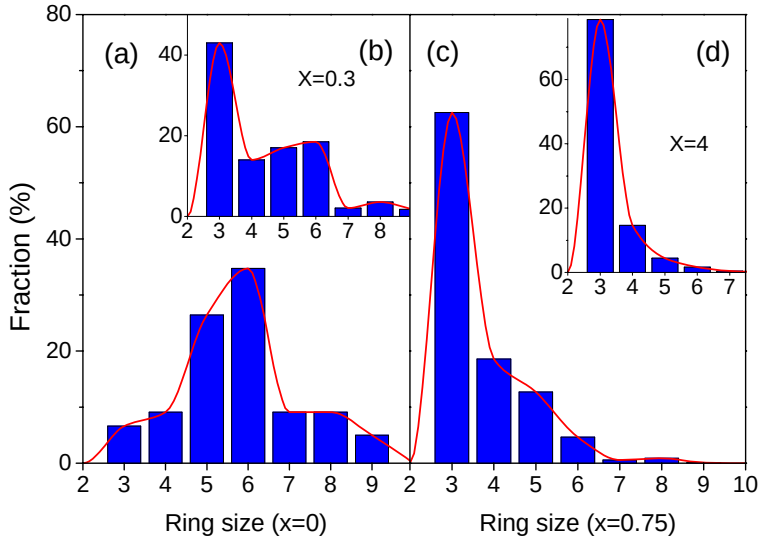

Figure 3. Histogram of the distribution of ring size (i.e., the number of members in the ring) in lithiated *a*-Si with different ratios of Li to Si, *x*. The fitting curve (in red) is plotted to guide eyes.

The foregoing atomic-level structural changes associated with Li insertion can be correlated to the evolution of ring statistics, which measure the medium-range order of amorphous network structures. We use Dijkstra's shortest path algorithm [24], implemented in MATLAB, and the ring counting method developed by Franzblau [25]. As shown in *Figure* 3(a), the ring fraction in the initial structure of *a*-Si ($x = 0$) exhibits a single peak at the 6-membered ring. Similar to the 8-membered ring shown in *Figure* 2, this kind of big 6-membered ring provides a large open space to accommodate the interstitially inserted Li. Figure 3(b) indicates that with increasing *x*, a peak of small 3-membered rings develops, while that of 6-membered rings diminishes. This change is understandable by noting the earlier observation that interstitially added Li often divides the big ring into several smaller rings. Moreover, we show in *Figure* 3(c) that when *x* is increased to around 0.8, the system consists dominantly of 3-membered rings with a single peak. Recall that in *Figure* 2(d), a further addition of Li causes the reconstruction of local ring structures when $x > 0.8$. This can be correlated to *Figure* 3(d)

showing an increase of the single peak of 3-membered rings. Finally, we note that a small percentage of large rings always retain even when *x* approaches its theoretical limit. This arises because some large rings counted in the statistics correspond to the case of small rings running along the belt of the big ring [26]. These small rings occupy the open space enclosed by the ring belt. As a result, such large rings could survive because there is little room to facilitate Li insertion.

Figure 4 shows the calculated volume and voltage versus Li composition curves, which are in accord with experimental measurements of lithiated *a*-Si [27-28]. The slope of the volume-composition curve corresponds to the volume increase per Li insertion, equivalent to the so-called partial molar volume of Li, Ω. Incidentally, Ω is a key parameter in the coarse-grained continuum model of diffusion-induced stress and cracking [9-11]. As seen from *Figure* 4, Ω is small and non-linear (the numerical fitting gives $\Omega = (0.57X^2 - 0.04X + 1.18)$ Å^3 per Li) when $X < 0.8$ (indicated by the green dashed line), while Ω is large and nearly a constant ($\Omega \approx 17.4$Å^3/atom $\approx 1.1 \times 10^{-5}$ m^3/mol) as $X \geq 0.8$. This trend can be correlated to the foregoing analyses revealing two kinds of structural changes that dominate at low and high Li concentrations, respectively: Li interstitial insertion and incorporation into the network. In the former case, the interstitial hole can well accommodate the inserted Li, so that the induced volume expansion is relatively small. This is in contrast to the latter case where the Li incorporation occurs through network reconstruction, causing a larger volume expansion. Furthermore, the higher voltage at small *x* is related to the dominant response of bond formation between Li and Si in the ring belt, while the reduced voltage at larger *x* is attributed to the increased energy cost associated with bond breaking and stretching manifested as the increased volume expansion.

To provide an accurate description of bond rupture and formation under different electro-chemical environments, it is essential to include quantum chemistry in the mechanics calculation [29-33]. Figure 5 shows the evolution of bonding environment by ADF curves and Coulson charge of silicon. At initial state x=0 (Figur5a), pure silicon systems have a peak in ADF curve at 110^o, which indicates directionally bonded material system. Along with the increase of concentration x, the peak at 110^o vanishes and the peak at 60^o rises. This implies that material transfers to an ionic bonding system. By examining Coulson charge of atoms, we find that Li atom always contains positive 0.5e. The charges on silicon atom depend on its local environments. As shown in figure 5b, if the more Li atoms a silicon atom is surrounded by, the more negative charge it may carry. Hence, the process of

lithiation can be considered as a procedure that system changes from directionally bonded to ionic bonded, and from brittle to ductile.

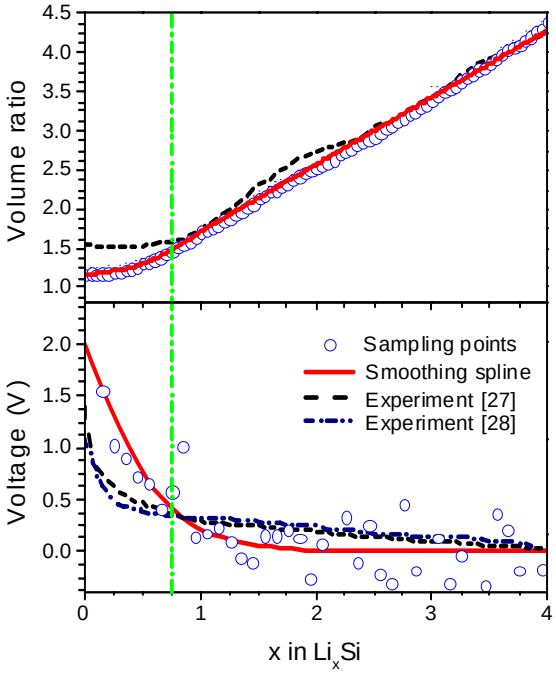

Figure 4. Comparison of the theoretical predictions and experimental measurements [27-28] of the electro-mechanical response of lithiated *α*-Si. (a) Ratio of the current and initial volume versus Li fraction *x*; (b) voltage versus Li fraction. The red solid line represents the statistical average using the Savitzky–Golay smoothing filter [20] as discussed in section 2.

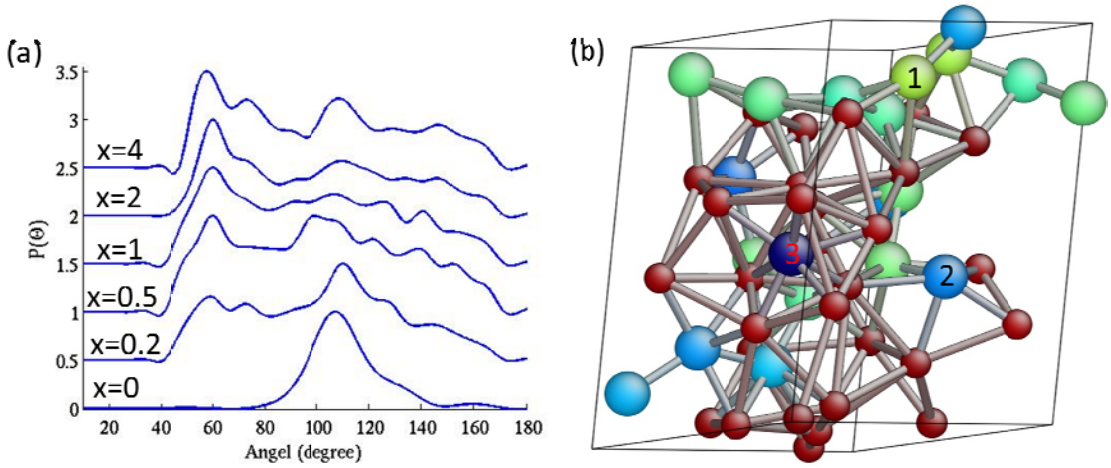

Figure 5. Evolution of bonding environments of lithiated silicon. (a) ADF of lithiated silicon under different concentration x; (b) The Coulson charge of silicon: -0.4e for #1 atom, -1.1e for #2 atom, -1.7e for #3 atom and +0.5e for lithium atoms.

6.4. Concluding remarks

In summary, the present study reveals the atomic structure, volume and voltage responses of lithiated *a*-Si. The results reinforce the notion that the Li-Si alloying behavior and associated properties, including the network topology characteristics of ring statistics, are sensitive to the local Li concentration [16]. Our work provides an atomistic rational of the relatively small volume expansion when the lithium fraction is less than about 0.8. This effect arises because of the limited dilatational effect associated with the insertion of lithium atoms that mostly reside in the energetically favorable sites of interstitial holes in the open network structure of Si. Since such small volume expansion has an intrinsic atomistic structural basis, it may have implications for reducing the stress buildup and thereby improving the reversibility of charging and discharging processes by controlling the extent of lithiation.

While the work focuses on the static aspects of lithiation, it also has implications on the dynamic processes of Li-Si mixing and electrochemically-driven solid state amorphization. Consider, as an example, Li diffusion in *a*-Si that underlies the aforementioned processes. It is generally recognized that diffusion in amorphous materials is controlled by a distribution of energy minima and activation barriers associated with a disordered network. This has been revealed, for example, in the study of

oxidation of Si [34-35] and hydrolysis of silica [32]. The present analyses of Li insertion in *a*-Si and, in particular, the calculated ring statistics suggest a simplified view of the energy landscape governing the Li diffusion and mixing in *a*-Si. Namely, the interstitial holes represent the deep sites (i.e., valleys) in the energy landscape, and the network incorporation sites correspond to the shallow sites. The deep and shallow sites can be, respectively, related to the 6-membered and 3-membered rings that peak in the ring distribution function at different *x* values (*Figure* 3). While the deep sites may play an important role in the volume and voltage changes during lithiation, the rate of Li diffusion is likely to be governed by the shallow sites with low activation barriers between neighboring shallow ones and by their percolation in the disordered network. A mechanistic study of the dynamic lithiation process would be highly desirable via a multiscale model that incorporates the above insights, e.g., by coupling the atomistic barriers, network topology and kinetic Monte-Carlo sampling, as implemented in the Si oxidation simulation [35], or a fully coupled stress-diffusion model in continuum level [36]. This is important for understanding the electrochemical alloying, and could have implications on improving the energy density and cycle reversibility of Li-ion batteries.

References

1. **Tarascon, J.M. and M. Armand, *Issues and challenges facing rechargeable lithium batteries.* Nature, 2001. 414(6861): p. 359-367.**
2. **Tarascon, J.M., *Key challenges in future Li-battery research.* Philosophical Transactions of the Royal Society A, 2010. 368(1923): p. 3227-3241.**
3. **Beaulieu, L.Y., et al., *Colossal reversible volume changes in lithium alloys.* Electrochemical and Solid State Letters, 2001. 4(9): p. A137-A140.**
4. **Limthongkul, P., et al., *Electrochemically-driven solid-state amorphization in lithium-silicon alloys and implications for lithium storage.* Acta Materialia, 2003. 51(4): p. 1103-1113.**
5. **Graetz, J., et al., *Nanocrystalline and thin film germanium electrodes with high lithium capacity and high rate capabilities.* Journal of the Electrochemical Society, 2004. 151(5): p. A698-A702.**
6. **Chan, C.K., et al., *High-performance lithium battery anodes using silicon nanowires.* Nature Nanotechnology, 2008. 3(1): p. 31-35.**
7. **Song, T., et al., *Arrays of Sealed Silicon Nanotubes As Anodes for Lithium Ion Batteries.* Nano Letters, 2010. 10(5): p. 1710-1716.**
8. **Chandrasekaran, R., et al., *Analysis of Lithium Insertion/Deinsertion in a Silicon Electrode Particle at Room Temperature.* Journal of the Electrochemical Society, 2010. 157(10): p. A1139-A1151.**
9. **Huggins, R.A. and W.D. Nix, *Decrepitation model for capacity loss during cycling of alloys in rechargeable electrochemical systems.* Ionics, 2000. 6: p. 57-63.**
10. **Bhandakkar, T.K. and H.J. Gao, *Cohesive modeling of crack nucleation under diffusion induced stresses in a thin strip: Implications on the critical size for flaw tolerant battery electrodes.* International Journal of Solids and Structures, 2010. 47(10): p. 1424-1434.**
11. **Hu, Y.H., X.H. Zhao, and Z.G. Suo, *Averting cracks caused by insertion reaction in lithium-ion batteries.* Journal of Materials Research, 2010. 25(6): p. 1007-1010.**
12. **Wen, C.J. and R.A. Huggins, *CHEMICAL DIFFUSION IN INTERMEDIATE PHASES IN THE LITHIUM-SILICON SYSTEM.* Journal of Solid State Chemistry, 1981. 37(3): p. 271-278.**
13. **Zhu, T. and J. Li, *Ultra-strength Materials.* Progress in Materials Science, 2010. 55: p. 710-757.**
14. **Dewar, M.J.S., et al., *THE DEVELOPMENT AND USE OF QUANTUM-MECHANICAL MOLECULAR-MODELS .76. AM1 - A NEW GENERAL-PURPOSE QUANTUM-MECHANICAL MOLECULAR-MODEL.* Journal of the American Chemical Society, 1985. 107(13): p. 3902-3909.**
15. **Barkema, G.T. and N. Mousseau, *Event-based relaxation of continuous disordered systems.* Physical Review Letters, 1996. 77(21): p. 4358-4361.**
16. **Shenoy, V.B., P. Johari, and Y. Qi, *Elastic softening of amorphous and crystalline Li-Si Phases with increasing Li concentration: A first-principles study.* Journal of Power Sources, 2010. 195(19): p. 6825-6830.**
17. **Stillinger, F.H. and T.A. Weber, *Computer-simulation of local order in condensed phases of silicon.* Physical Review B, 1985. 31(8): p. 5262-5271.**
18. **Chevrier, V.L. and J.R. Dahn, *First Principles Model of Amorphous Silicon Lithiation.* Journal of the Electrochemical Society, 2009. 156(6): p. A454-A458.**
19. **Chevrier, V.L. and J.R. Dahn, *First Principles Studies of Disordered Lithiated Silicon.* Journal of the Electrochemical Society, 2010. 157(4): p. A392-A398.**

20. **Savitzky, A. and M.J.E. Golay, *SMOOTHING + DIFFERENTIATION OF DATA BY SIMPLIFIED LEAST SQUARES PROCEDURES.* Analytical Chemistry, 1964. 36(8): p. 1627-&.**
21. **Demkowicz, M.J. and A.S. Argon, *High-density liquidlike component facilitates plastic flow in a model amorphous silicon system.* Physical Review Letters, 2004. 93(2): p. 025505.**
22. **Mousseau, N. and G.T. Barkema, *Activated mechanisms in amorphous silicon: An activation-relaxation-technique study.* Physical Review B, 2000. 61(3): p. 1898-1906.**
23. **Kubota, Y., et al., *Crystal and electronic structure of Li15Si4.* Journal of Applied Physics, 2007. 102(5): p. 053704.**
24. **Dijkstra, E.W., *A note on two problems in connexion with graphs.* Numerische Mathematik, 1959. 1: p. 269-271.**
25. **Franzblau, D.S., *COMPUTATION OF RING STATISTICS FOR NETWORK MODELS OF SOLIDS.* Physical Review B, 1991. 44(10): p. 4925-4930.**
26. **Caravati, S., M. Bernasconi, and M. Parrinello, *First-principles study of liquid and amorphous Sb2Te3.* Physical Review B, 2010. 81(1): p. 014201.**
27. **Beaulieu, L.Y., et al., *Reaction of Li with alloy thin films studied by in situ AFM.* Journal of the Electrochemical Society, 2003. 150(11): p. A1457-A1464.**
28. **Baggetto, L., et al., *On the electrochemistry of an anode stack for all-solid-state 3D-integrated batteries.* Journal of Power Sources, 2009. 189(1): p. 402-410.**
29. **Ogata, S., et al., *Environmental effects of H2O on fracture initiation in silicon: A hybrid electronic-density-functional/molecular-dynamics study.* Journal Of Applied Physics, 2004. 95(10): p. 5316-5323.**
30. **Carter, E.A., *Challenges in modeling materials properties without experimental input.* Science, 2008. 321(5890): p. 800-803.**
31. **Buehler, M.J., *Atomistic Modeling of Materials Failure*. 2008: Springer.**
32. **Zhu, T., et al., *Stress-dependent molecular pathways of silica-water reaction.* Journal of the Mechanics and Physics of Solids, 2005. 53(7): p. 1597-1623.**
33. **Buehler, M.J. and S. Keten, *Colloquium: Failure of molecules, bones, and the Earth itself.* Reviews of Modern Physics, 2010. 82(2): p. 1459-1487.**
34. **Mott, N.F., *ON THE OXIDATION OF SILICON.* Philosophical Magazine B, 1987. 55(2): p. 117-129.**
35. **Bongiorno, A. and A. Pasquarello, *Multiscale modeling of oxygen diffusion through the oxide during silicon oxidation.* Physical Review B, 2004. 70(19): p. 195312.**
36. **Gao, Y.F. and M. Zhou, *Strong stress-enhanced diffusion in amorphous lithium alloy nanowire electrodes.* Journal of Applied Physics, 2011. 109(1).**

7. LITHIATION INDUCED PLASTIC DEFORMATION IN ELECTRODE NANO-PARTICLES AND NANO-WIRES

A viscoelastic-plastic model at continuum level is developed in this chapter. In lithiated material, the total strain is a summation of chemical strain, elastic strain and plastic strain: $\dot{\varepsilon}_{ij}^{total} = \dot{\varepsilon}_{ij}^{chemical} + \dot{\varepsilon}_{ij}^{elastic} + \dot{\varepsilon}_{ij}^{plastic}$. Chemical strain is induced by the insertion of lithium and it is not isotropic for lithiation of crystals, namely $\dot{\varepsilon}_{ij}^{chemical} = \boldsymbol{\beta}_{ij}\dot{c}$, where the direct component of $\boldsymbol{\beta}_{ij}$ is different. The constitutive law of elastic strain follows $\dot{\varepsilon}_{ij}^{elastic} = \boldsymbol{S}_{ijkl}(\boldsymbol{c})\dot{\sigma}_{kl}$, where the matrix of elastic constants of compliance $\boldsymbol{S}_{ijkl}(\boldsymbol{c})$ depends on the concentration of lithium [1]. For the plastic response of lithiated silicon and tin-based material, we assume the plastic strain follows the J_2 flow rule.

In this chapter, we discuss the elastic-plastic behaviors of nano-particle and nano-wire during lithiation and assume isotropic responses. In reality, the anisotropy of crystalline material can have significant effects as observed in experiments. This is studied in chapter 8 to correlate with experimental observations. In addition, coated nano-wires, such as tin-oxide coated by carbon and aluminum, are studied by both experiments and modeling, in order to understand how to control the diffusion induced deformation. The application of elastic-plastic model described in this chapter involves different materials , geometries and interfaces between the nanowire and coating, as further discussed in chapter 9.

7.1 Introduction

Nano-particles and nano-wires are being extensively studied as the basic building blocks of electrodes for lithium ion batteries (LIBs) [2-7]. To achieve a higher energy density, silicon, tin and their alloys have been considered as a replacement for graphite as the anode material in LIBs [8-9]. One critical issue associated with the use of Si- and Sn-based electrodes is the large volume change associated with lithium insertion and extraction, ~ 310% for Si and ~ 240% for SnO_2. This can cause fracture and eventually pulverization of electrodes, thus limiting the lifetime of LIBs. To prevent

fracture, an essential step is to understand how the stresses generate and evolve in lithiated particles and wires.

Recent experimental measurements [10] show that plastic yielding occurs in lithiated Si. The *In situ* TEM experiments [7] reveal that during lithiation of crystalline Si and SnO_2 nanowires, a well-defined lithiation reaction front can be identified to separate the Li-poor and Li-rich phases. While various theoretical models have been developed to analyze the lithium diffusion and stress state in lithiated particles and wires [11-20], no study has simultaneously considered both plastic yielding and coexistence of the two Li phases. We report in this Letter a theoretical model accounting for both factors.

7.2 Method and model description

To provide a direct physical appreciation of the stress states in the presence of coexisting Li-poor and Li-rich phases, we show, in *Figure* 1, the history of a representative material element *A* in a spherical particle; the related discussion is also applicable to a cylindrical wire. In *Figure* 1, spherically symmetric configurations are used to represent the progressive lithiation process. The lithiation reaction front is modeled as a sharp interface between the shrinking pristine core (white) and growing lithiated shell (grey). The latter is assumed to be fully lithiated with nearly constant lithium concentration. This essentially means that Li diffusion is extremely fast in the lithiated shell, and the propagation of the reaction front is the rate limiting step, as hinted by experimental measurements of the linear time dependence of the reaction front migration distance. It follows that the electrochemically induced strain should mainly generate near the core-shell interface. In this Letter the strain associated with lithium insertion is of electrochemical origin, called the lithiation strain. And it is accommodated by subsequent elastic-plastic deformation, as dictated by the stress equilibrium of deformable bodies. In a first approximation, we assume the lithiation strain being dilatational and equal in all directions, e.g., (r, θ, φ) directions in a spherical coordinate system.

Figure 1(a) shows that in the early stage of lithiation, element *A* is located within the pristine core and away from the reaction front. As lithiation takes place at the reaction front, the newly lithiated material at the front tends to move in the outward radial direction. This arises because there are larger areas in the hoop direction at larger radial distances, such that the lithiation-induced

volume expansion can be better accommodated with lower stresses generated. This outward displacement results in hydrostatic tension in element *A*, as represented by stage (a) of the $\sigma_\theta - t$ curve in *Figure* 1(d). As the reaction front sweeps through element *A*, a large dilatational lithiation strain is created at *A*. Due to the constraint of surrounding materials, local compressive stresses develop, such that element *A* sequentially undergoes tensile elastic unloading, compressive elastic loading, and compressive plastic yielding in the hoop direction. This stress history is schematically represented by stage (b) in *Figure* 1(d). Interestingly, as the reaction front continues to move toward the center, the newly created lithiation strain at the front tends to further displace element *A* in the outward radial direction and simultaneously stretches it in the hoop directions (both θ and φ). As a result, element *A* experiences compressive elastic unloading, tensile elastic loading and tensile plastic yielding, corresponding to stage (c) in *Figure* 1(d). It is important to note that tensile plastic flow in the surface layer could cause morphological instability and fracture of electrode particles and wires during lithium insertion.

To gain further insights into the stress development during lithiation, we have simulated the co-evolving processes of lithium diffusion and stress generation. The time evolution of the two Li phases is modeled by using a non-linear diffusion model. The concentration of Li, *c*, is governed by the standard diffusion equation. It is normalized by the Li concentration at the fully lithiated state, such that *c* varies between 0 to 1. To capture the co-existence of the Li-poor and Li-rich phases, we assume that the diffusivity *D* is non-linearly dependent on *c*. Note that our diffusion simulations mainly serve to generate a sequence of core-shell structures for the stress analyses, rather than provide a precise description of the dynamic lithiation process. To this end, we take a simple non-linear function of $D = D_0\left[2\Omega c - 1/(1-c)\right]$, where D_0 is the diffusivity constant and Ω is tuned to control the concentration profile near and behind the reaction front. The particle is initially pristine and subjected to constant flux I_0 at the surface.

We adopt an elastic and perfectly plastic model to describe the lithiation-induced deformation. The increment of the total strain, $d\varepsilon_{ij}$, is taken to be the sum of three contributions, $d\varepsilon_{ij} = d\varepsilon_{ij}^c + d\varepsilon_{ij}^e + d\varepsilon_{ij}^p$. Here the increment of the lithiation-induced electrochemical strain, $d\varepsilon_{ij}^c$, is proportional to the increment of the normalized Li concentration, $d\varepsilon_{ij}^c = \beta_{ij} dc$, where β_{ij} represents

the lithiation expansion coefficient with non-zero direct components. The increment of the elastic strain, $d\varepsilon_{ij}^{e}$, obeys Hooke's law with two elastic constants needed, i.e., Young's modulus *E* and Possion's ratio *v*. The increment of the plastic strain, $d\varepsilon_{ij}^{p}$, obeys the classic J_2-flow rule; namely plastic yielding occurs when the von Mises equivalent stress, $\sigma_{\text{Mises}} = \sqrt{3s_{ij}s_{ij}/2}$, equals the yield strength σ_Y. Here $s_{ij} = \sigma_{ij} - \sigma_{kk}\delta_{ij}/3$ is the deviatoric stress; $d\varepsilon_{ij}^{p}$ is proportional to s_{ij} and can be determined by solving the boundary value problem. The outer surface is traction free.

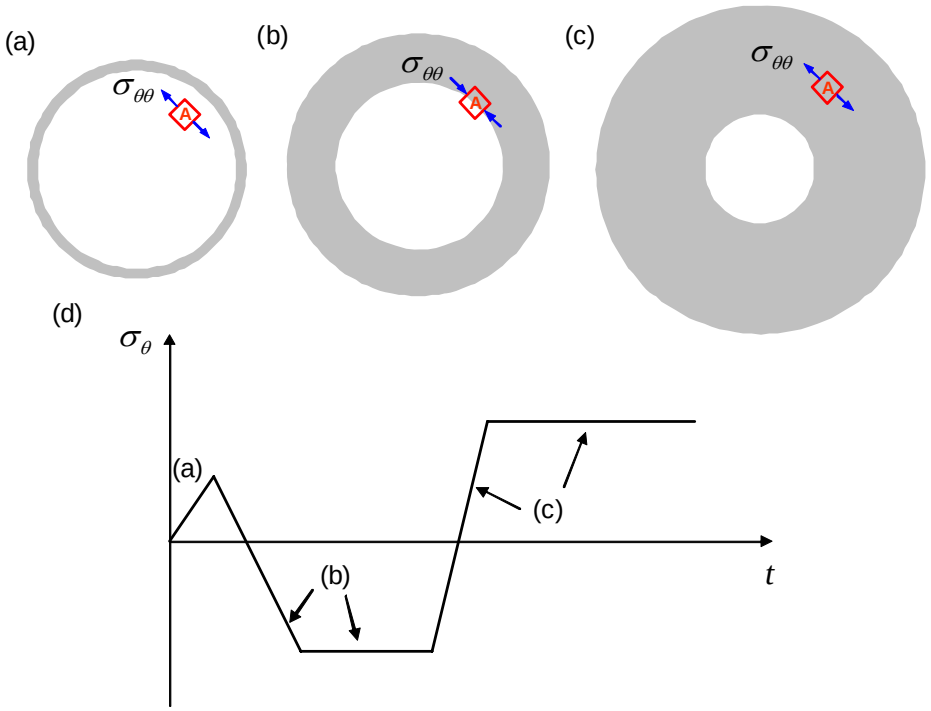

***Figure* 1 Schematics of the pristine core (white) and lithiated shell (grey) and the temporal evolution of the hoop stress $\sigma_{\theta\theta}$ in a spherical particle. (a-c) $\sigma_{\theta\theta}$ in a representative material element *A* located at various distances relative to the moving lithiation reaction front, i.e., the core-shell interface. Progressive lithiation results in a gradual expansion of the particle. (d) $\sigma_{\theta\theta}$ as a function of time *t* in element *A*.**

We numerically implement the above diffusion and elastoplastic model by using the finite element package ABAQUS 6.10. The Li and stress-strain fields are solved with an implicit, coupled temperature-displacement procedure in ABAQUS/Standard. That is, the normalized concentration is surrogated by temperature and the lithiation expansion coefficient β_{ij} is equivalently treated as the thermal expansion coefficient. The user material subroutine for heat transfer (UMATHT) is programmed to interface with ABAQUS to update diffusivities based on the current Li concentration (i.e., temperature). The Li distribution and accordingly elastic-plastic deformation are updated incrementally. The axis symmetric condition is used to reduce the computational cost. We choose the lithiation parameters typical for Si, $\beta_{11}=\beta_{22}=\beta_{33}=0.6$, $\sigma_Y=0.02E/(1-\nu)$, $\nu=0.3$. The diffusion properties are assigned to generate a numerically stable core-shell structure, $\Omega=2.1$ and $I_0=10D_0$.

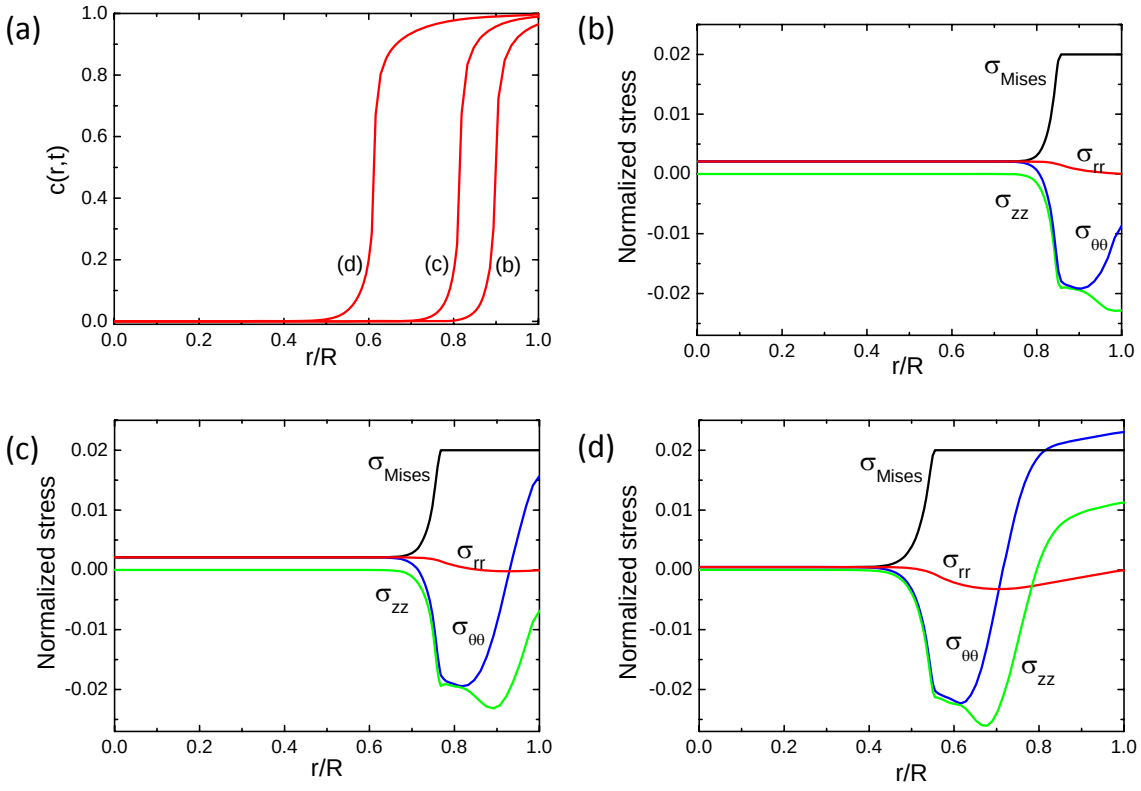

Figure 2. The Li and stress distributions in a spherical particle. (a) Li concentration c as a function of radial distance *r* at different instances, (b) → (c) → (d). Here *c* is normalized by its maximum value at

the fully lithiated state, and *r* is normalized by the current radius *R* of a partially lithiated particle (*R* increases as lithiation proceeds). (b-d) Radial distribution of stresses normalized by $E/(1-\nu)$.

7.3 Results and discussion

Figure 2 shows the calculated Li and stress distributions in a spherical particle at three different moments. In *Figure* 2(a), the Li concentration profile captures the juxtaposition of the Li-poor and Li-rich phases. The interface between the pristine core and lithiated shell can be identified at the radial distance where the Li concentration has an abrupt change. In addition, c smoothly transits to the limits of 0 and 1 near the reaction interface, thereby facilitating numerical stability. As Li continuously fluxes in from the surface, the reaction front moves toward the center. Because of the spherical symmetry, the hoop stresses $\sigma_{\theta\theta} = \sigma_{\varphi\varphi}$ and all the shear stresses vanish. Figs. 2(b-d) show the radial stress distributions, which respectively correspond to the three Li concentration profiles in *Figure* 2(a). Of particular importance is the insights gained from the combined reading of the radial distributions of $\sigma_{\theta\theta}$ and σ_{Mises} in *Figure* 2(d). Namely, the material elements at the increasing radial distance *r* experience the respective hoop stress of (hydrostatic) tension, compressive plastic yielding, elastic unloading, tensile elastic loading, and tensile plastic yielding. This spatial stress variation can be directly correlated to the schematic plot in *Figure* 1(d) showing the temporal evolution of $\sigma_{\theta\theta}$ at a fixed material element.

We have similarly simulated the lithiation responses in a cylindrical wire. In this case, the plane strain condition is assumed, considering that the lithiation strain mainly occurs near the core-shell interface which is subjected to the clamping constraints from less deformed materials in front of and behind the interface. Figure 3 shows the calculated Li and stress distributions in the wire. Compared to *Figure* 2, while most essential features of the stress evolution are similar, there is one notable difference. In the case of the particle, the radial distributions of σ_{Mises} and $\sigma_{\theta\theta}$ in *Figure* 2(d) indicate that a sandwiched deformation state can develop in the lithiated shell with an elastic layer in between two plastic layers; the one near the reaction front is compressively yielded, and another one

close to surface experiences tensile yielding. In contrast, Figs. 3(b-d) indicate that the lithiated shell in the wire, once yielded, remains fully plastic as lithiation proceeds. The different yielding response can be attributed to the fact that the spherical symmetry in the particle imposes a strong constraint on the hoop stresses, requiring $\sigma_{\theta\theta} = \sigma_{\varphi\varphi}$, while the axial stress σ_{zz} in the wire can adapt to the changes of other normal stress components.

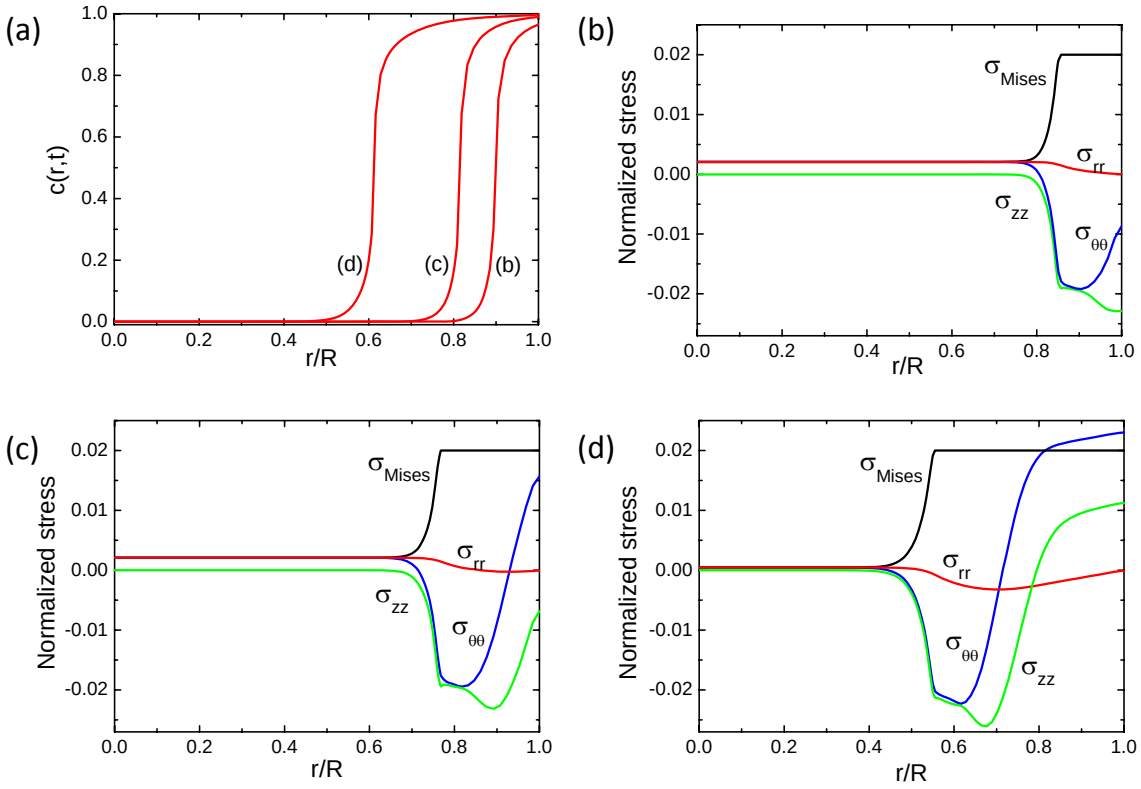

Figure 3. Same as Fig.2 except for a lithiated cylindrical wire.

It is generally recognized that during *delithiation* the tensile hoop stress $\sigma_{\theta\theta}$ should naturally arises due to the constraint experienced by the delithiated material element that tends to contract. However, it is somewhat unexpected to find that during *lithiation* of both particles and wires, the tensile hoop stress $\sigma_{\theta\theta}$ can also develop, even attaining the plastic yielding. As discussed earlier, this response results from the continuous outward displacement of materials in the outer layer of the

lithiated shell, driven by the internal volume expansion at the lithiation reaction front that progressively moves toward the center.

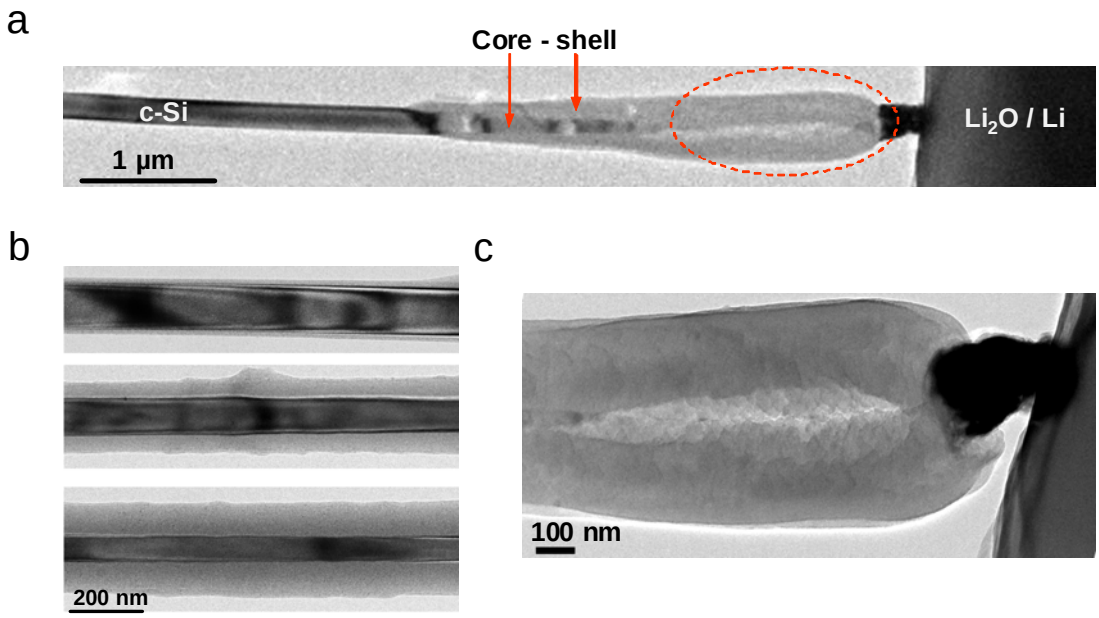

***Figure* 4. *In situ* TEM images of a partially lithiated nanowire. (a) A crystalline Si (c-Si) nanowire is in contact with a lithium metal, whose surface is covered with Li_2O. Subjected to an applied voltage, Li ions flow in from the right end and diffuse to the left. (b) Time-elapsed snapshots showing the shrinking Si core (black) and growing lithiated shell (grey). (c) Zoom-in image of the circled area in (a), showing the formation of surface crack due to tensile plastic flow in the lithiated outer layer of the wire.**

Our recent experiment of lithiation of single nanowire electrodes provides a support to the present model of the lithiation-induced plastic deformation in particles and wires. The *In situ* TEM image of *Figure* 4(a) shows a snapshot of a partially lithiated Si nanowire, where the lithiation starts at the right end and prorogates to the left. *Figure* 4(b) reveals the time evolution of the coexisting crystalline core (black) and lithiated shell (grey) in the wire. Notice that in *Figure* 4(a) the cross-sections at different axial positions can be viewed as the intermediate lithiation responses of a given cross section at different times. The right part of this partially lithiated wire, along with the zoom-in

image of *Figure* 4(c), shows the formation of the surface crack in the late stage of lithiation of a cross section. Our detailed numerical simulations of this lithiation process, reported elsewhere, indicate that the surface crack can develop due to the tensile plastic flow of the surface layer.

7.4 Conclusion

In summary, we have analyzed the stress development in lithiated particles and wires by accounting for both plastic yielding and coexistence of the two Li phases. A key finding is that tensile plastic flow can arise in the lithiated shell even during lithium insertion. This tensile flow response is driven by the progressive electrochemical reaction, and can consequently trigger the morphological instability near the surface that may lead to fracture of electrode particles and wires. To gain essential physical insights, our model invokes various simplified assumptions. In the future, it is worthwhile to evaluate the impact of various factors, such as anisotropic properties of crystalline phases (e.g., diffusivity, electrochemically-induced lithiation strain) [17]; fully coupled stress-diffusion relation [21] lithium concentration-dependent mechanical properties (e.g., Young's Modulus, yield strength) [1]; viscoelastic, viscoplastic, strain hardening behaviors; coupling between diffusivity and stress [22], etc. From the battery design standpoint, insights gained may help control and mitigate the lithiation-induced deformation and fracture, thereby enabling the design of better batteries.

References

1. **Shenoy, V.B., P. Johari, and Y. Qi, *Elastic softening of amorphous and crystalline Li-Si Phases with increasing Li concentration: A first-principles study.* Journal of Power Sources, 2010. 195(19): p. 6825-6830.**
2. **Bruce, P.G., B. Scrosati, and J.M. Tarascon, *Nanomaterials for rechargeable lithium batteries.* Angewandte Chemie-International Edition, 2008. 47(16): p. 2930-2946.**
3. **Meethong, N., et al., *Electrochemically Induced Phase Transformation in Nanoscale Olivines Li1-xMPO4 (M = Fe, Mn).* Chemistry of Materials, 2008. 20(19): p. 6189-6198.**
4. **Magasinski, A., et al., *High-performance lithium-ion anodes using a hierarchical bottom-up approach.* Nature Materials, 2010. 9(4): p. 353-358.**
5. **Chan, C.K., et al., *High-performance lithium battery anodes using silicon nanowires.* Nature Nanotechnology, 2008. 3(1): p. 31-35.**
6. **Song, T., et al., *Arrays of Sealed Silicon Nanotubes As Anodes for Lithium Ion Batteries.* Nano Letters, 2010. 10(5): p. 1710-1716.**
7. **Huang, J.Y., et al., *In Situ Observation of the Electrochemical Lithiation of a Single SnO2 Nanowire Electrode.* Science, 2010. 330(6010): p. 1515-1520.**
8. **Kasavajjula, U., C.S. Wang, and A.J. Appleby, *Nano- and bulk-silicon-based insertion anodes for lithium-ion secondary cells.* Journal of Power Sources, 2007. 163(2): p. 1003-1039.**
9. **Todd, A.D.W., et al., *Tin-based materials as negative electrodes for Li-ion batteries: Combinatorial approaches and mechanical methods.* International Journal of Energy Research, 2010. 34(6): p. 535-555.**
10. **Sethuraman, V.A., et al., *In situ measurements of stress evolution in silicon thin films during electrochemical lithiation and delithiation.* Journal of Power Sources, 2010. 195(15): p. 5062-5066.**
11. **Christensen, J. and J. Newman, *Stress generation and fracture in lithium insertion materials.* Journal of Solid State Electrochemistry, 2006. 10(5): p. 293-319.**
12. **Zhang, X.C., W. Shyy, and A.M. Sastry, *Numerical simulation of intercalation-induced stress in Li-ion battery electrode particles.* Journal of the Electrochemical Society, 2007. 154(10): p. A910-A916.**
13. **Cheng, Y.T. and M.W. Verbrugge, *Evolution of stress within a spherical insertion electrode particle under potentiostatic and galvanostatic operation.* Journal of Power Sources, 2009. 190(2): p. 453-460.**
14. **Deshpande, R., Y.T. Cheng, and M.W. Verbrugge, *Modeling diffusion-induced stress in nanowire electrode structures.* Journal of Power Sources, 2010. 195(15): p. 5081-5088.**
15. **Tang, M., et al., *Model for the Particle Size, Overpotential, and Strain Dependence of Phase Transition Pathways in Storage Electrodes: Application to Nanoscale Olivines.* Chemistry of Materials, 2009. 21(8): p. 1557-1571.**
16. **Burch, D. and M.Z. Bazant, *Size-Dependent Spinodal and Miscibility Gaps for Intercalation in Nanoparticles.* Nano Letters, 2009. 9(11): p. 3795-3800.**
17. **Tang, M., W.C. Carter, and Y.M. Chiang, *Electrochemically Driven Phase Transitions in Insertion Electrodes or Lithium-Ion Batteries: Examples in Lithium Metal Phosphate Olivines.* Annual Review of Materials Research, 2010. 40: p. 501-529.**

18. **Woodford, W.H., Y.M. Chiang, and W.C. Carter, *"Electrochemical Shock" of Intercalation Electrodes: A Fracture Mechanics Analysis.* Journal of the Electrochemical Society, 2010. 157(10): p. A1052-A1059.**
19. **Chandrasekaran, R., et al., *Analysis of Lithium Insertion/Deinsertion in a Silicon Electrode Particle at Room Temperature.* Journal of the Electrochemical Society, 2010. 157(10): p. A1139-A1151.**
20. **Zhao, K.J., et al., *Inelastic hosts as electrodes for high-capacity lithium-ion batteries.* Journal of Applied Physics, 2011. 109: p. 016110**
21. **Gao, Y.F. and M. Zhou, *Strong stress-enhanced diffusion in amorphous lithium alloy nanowire electrodes.* Journal of Applied Physics, 2011. 109(1).**
22. **Haftbaradaran, H., et al., *Continuum and atomistic models of strongly coupled diffusion, stress, and solute concentration.* Journal of Power Sources, 2011. 196(1): p. 361-370.**

8. ANISOTROPIC EXPANSION, DIFFUSION AND SELF-SPLITTING OF SILICON NANOWIRE ELECTRODES IN LITHIUM ION BATTERIES

8.1 Introduction

Silicon, due to its highest energy capacity, is being extensively studied as a most promising anode material in lithium ion battery (LIB). Silicon possesses the highest specific capacity among all materials (4200 mAh·g^{-1} for $Li_{22}Si_5$), over an order of magnitude higher than that of the carbon used in current LIBs. However, Si experiences a ~300% volume expansion after full lithiation, and the large volume change during cycling causes fracture and pulverization, leading to capacity fading [1-17]. As discussed in chapter 6 and 7, the morphological changes and mechanical failure of lithiated Si limits its electrochemical performance in LIBs. The underlying microscopic mechanisms are presently unknown, thus preventing the implementation of Si as anode materials for radically improving the energy capacity of LIBs.

For the first time, the surprisingly large anisotropic expansion of Si nanowires during electrochemical lithiation is directly video-recorded by Dr. Jianyu Huang at Sandia National Laboratories through *in situ* experiments. This anisotropic lithiation response was entirely unexpected, and it leads to important morphological and mechanical consequences, including the development of a remarkable dumbbell-shaped cross section, and even self-splitting behaviors. The mechanism underlying the sub-division of nanowire electrodes may also be responsible for the development of sponge-like morphology in bulk Si electrodes upon cycling [2-4]. This mechanical fracture mode is very unique, and our analysis highlights the critical role of electrochemically induced plastic deformation during its initiation. How cracks initiate and evolve during cycling remains unclear. A fundamental understanding of the plastic deformation and fracture mechanisms in lithiated Si may help develop strategies to mitigate the large expansion and crack formation during cycling, thus paving the way for the application of Si as a high energy density electrode in LIBs [18-20].

8.2 *In situ* observations

Recently, our collaborator Dr. Jianyu Huang at Sandia national lab reports a creation of a nanoscale all-solid electrochemical cell inside a transmission electron microscope (TEM) - consisting of a single Si nanowire anode, a Li_2O solid electrolyte, and a bulk Li metal cathode - enabling real-time observation of the structure evolution of electrodes during electrochemical reactions.

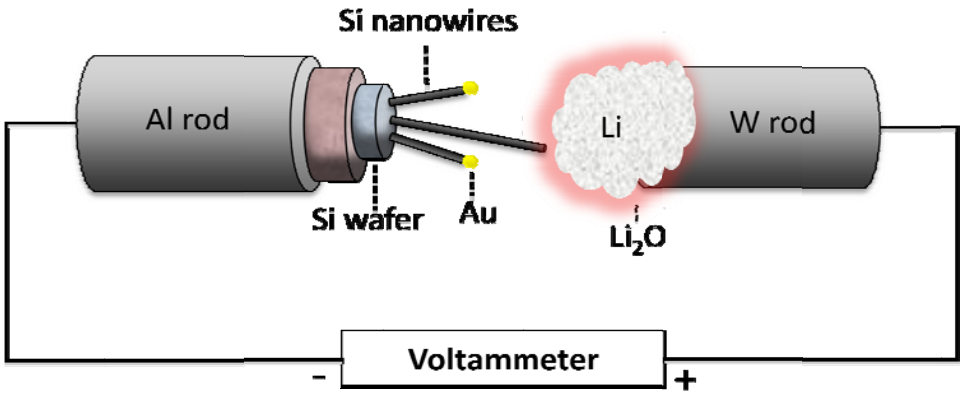

Figure 1. Crack formation during lithiation of a Si nanowire. (a) Schematic illustration of the in-situ experimental setup for an all-solid electrochemical device for Si lithiation tests.

Figure 1 shows the schematic illustration of their experimental setup. Lithium metal is loaded as the Li source and References electrode. Whenever silicon nanowires touch the lithium, a half battery is built up. Lithiation then occurred in the silicon nanowires and the whole procedure of reaction is recorded by their *in situ* TEM. A reaction front (pointed out by red arrows in Figs. 2) propagates progressively along the longitudinal axis of the nanowire. In the meantime, lithiation also occurs along the radial direction, from the surface to the core, leading to the formation of a thick shell with an unreacted crystalline Si (*c*-Si) core. The *c*-Si core exhibited a tapering shape, with its diameter shrinking continuously from the reaction front towards the point of initial contact, while length of the tapering shape is about three time of nano-wire radius. At the point the *c*-Si core disappeared, i.e. the Si was fully lithiated, a nanocrack formed (*Figure* 2e). This crack continues to grow as the lithiation front progresses further along the wire (Figs. 2f-2i).

Figure 2. Crack formation and propagation in the center of a Si nanowire during the lithiation. Arrows point out the reaction fronts. (b) Pristine silicon nanowire contacting Li_2O/Li. (c-e) Lithiation via a core-shell manner. As the reaction front propagated towards the nanowire base, lithiation proceeded from the surfaces towards the center of the nanowire. A *c*-Si core was visible at this stage. Note that the Au cap was deformed/lithiated. (f-j) Crack evolution in the center of the nanowire. The length of the crack increased quickly in the initial stage, but finally stayed at 1760 nm.

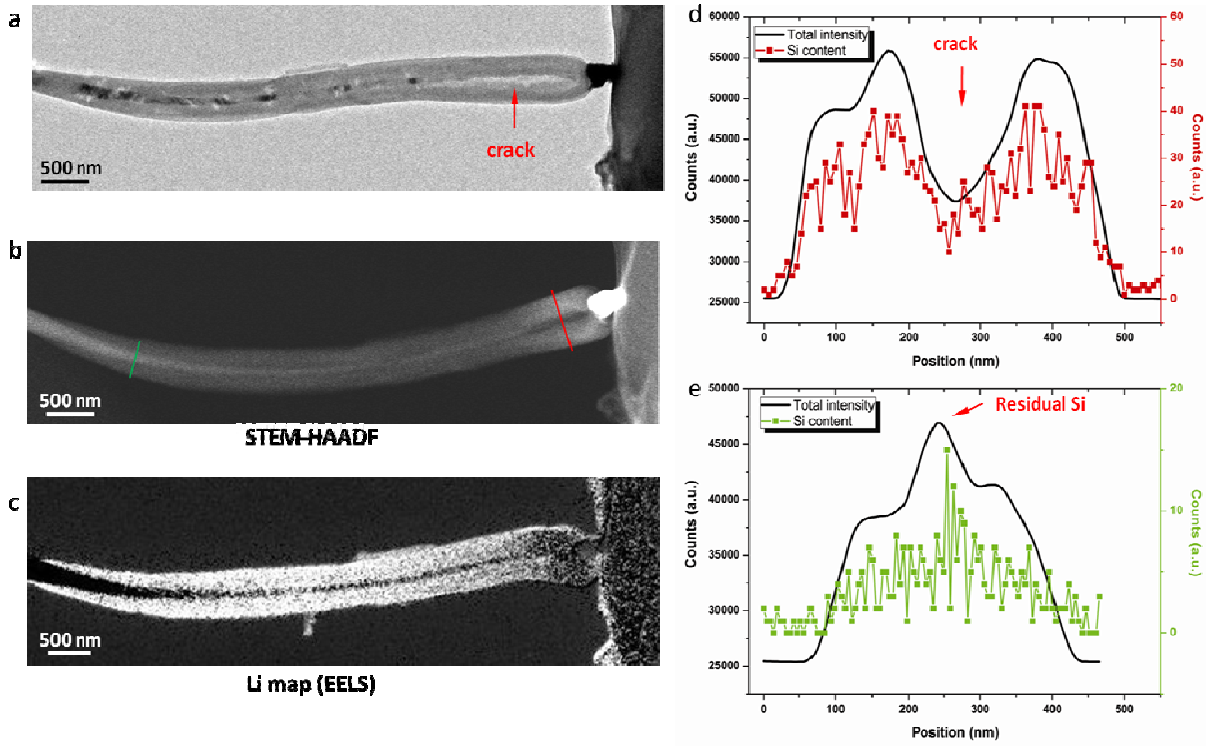

Figure 3. Structure characterization of the lithiated and cracked silicon nanowire. (a) Conventional TEM image of the lithiated Si nanowire. The crack showed bright contrast. (b) STEM-HAADF image of the nanowire. The crack showed dark contrast, indicating less material (lower average *Z*) present. The STEM image was collected with a camera length of 120 mm. (c) Lithium map by EELS showing the lithium distribution in the $Li_{15}Si_4$ shell. Note the *c*-Si show dark contrast, indicating less or no lithium. The mapping was obtained using a spectrum imaging technique in Digital Micrograph. The energy window was from 40 to 80 eV, and the step was 3 eV. (d-e) Line scans along the red and green lines in (b), respectively, showing the total intensity profile which is proportional to the sample mass-thickness (dark lines in g and h), and Si-K_α EDX intensity profile (red and green lines in g and h, respectively), confirming the presence of a crack (d) and a residual *c*-Si core (e) from the lithiated nanowire.

Meanwhile, the speed of reaction is measured. The front migration distance *L* is found to be approximately linear with respect to the reaction time $L \propto t$ (*Figure* 2j), indicating the kinetics of lithiation is likely controlled by short-ranged processes near the reaction front (interfacial diffusion and reaction, adjacent plastic flow), not by long-ranged diffusive transport along the wire. This is in

sharp contrast to the $L \propto t^{1/2}$ behavior found in the lithiation of SnO_2 nanowires using an ionic liquid electrolyte in-situ electrochemical cell setup [18]. This difference suggest that the lithiation kinetics of nanowires could be long-range diffusion controlled or short-range reaction controlled. It is not generic but instead highly dependent on the material system.

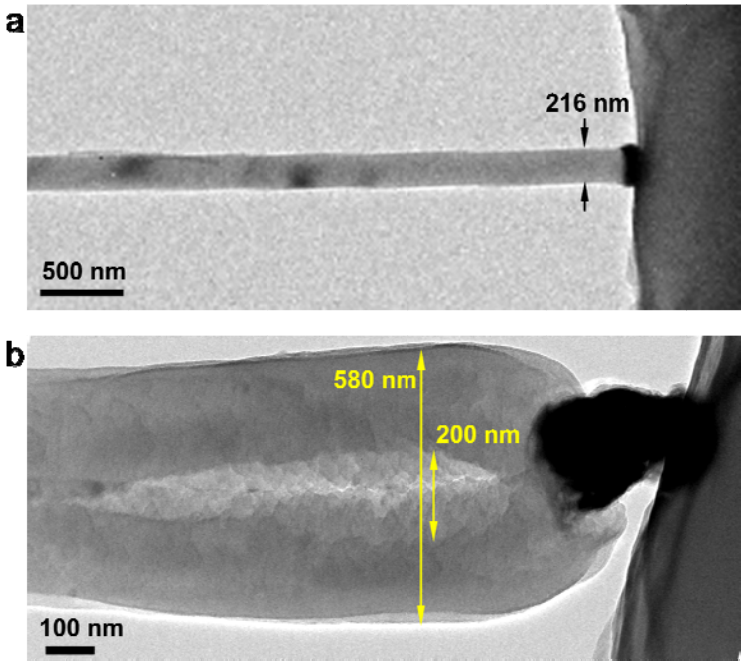

Figure 4. Self-splitting of a nanowire from the central crack during lithiation. Closer views of the joints where the nanowire was split into two sub-wires. The yellow arrows mark the splitting directions and the central crack.

The concentration of lithium along the silicon nanowires is also examined. The electron diffraction pattern (EDP) from the lithiated segment of the nanowire confirmed the formation of a polycrystalline $Li_{15}Si_4$ (*c*-$Li_{15}Si_4$) phase mixed with amorphous Li_xSi (*a*-Li_xSi), consistent with previous reports [14,21-23]. There was a residual *c*-Si core near the reaction front and the left end of the crack (*Figure* 3a), which was consistent with the scanning transmission electron microscopy - high angle annular dark field (STEM-HAADF) image (*Figure* 3b) showing the Z-contrast (Z: atomic number) of the nanowire. In the central dark region, Si was depleted and there was less mass than in the bright regions, confirming the formation of a crack in the center of the nanowire. Figure 2f shows an electron energy loss spectroscopy (EELS) map of Li, confirming the presence of Li in the lithiated shell of the

nanowire. Figures 3d and 3e show line scans across the crack (red line in Figs. 3b, 2d) and the partially lithiated part (green line in Figs. 3b, 3e) of the nanowire, respectively. The crack was revealed by an intensity dip in both the Z-contrast intensity (black line in *Figure* 3d) and the Si-K_α (1.7 keV) energy-dispersive X-ray spectroscopy (EDX) intensity (red trace in *Figure* 3d). In contrast, Figure 3e indicates that average Z was significantly lower in the $Li_{15}Si_4$ shell than the *c*-Si core.

Figure 5. Anisotropic expansion of Si nanowire during lithiation. (a-b) Tilting series images showing cross-sections of a lithiated and a pristine Si nanowire, respectively, showing the cross-section changed from the initial circular shape (b) to a dumbbell shape after lithiation (a).

Figure 4 shows a more detailed structural characterization of lithiated silicon nanowire as in figure 2. A very large "diameter" change was observed along this viewing direction. The "diameter" increases from 216 nm to 580 nm (i.e., ~170% diameter elongation) with an obvious crack in the center of the nanowire. Such large change in "diameter" implies an over 600% volume expansion, if cylindrical shape of the lithiated nanowire is assumed. To understand the anomalous expansion, the

nanowire is rotated to see the exact shape of cross section after lithiation. A series of images taken at different tilts revealed the dumbbell morphology of the lithiated nanowire (*Figure* 5a), in contrast to the circular cross-section of the pristine nanowires (*Figure* 5b). Detailed measurements show that the lithiated nanowire exhibits less expansion when viewed along the [110] zone axis. Observations on other nanowires confirmed the same anisotropic expansion: the diameter expands by ~ 170% along <110> but less than 20% along <111> directions.

Although the tapering shape of reaction front and crack at nano-wire surface along longitudinal direction are successfully predicted by our model described in chapter 7, mysteries remain, such as the stress state inside nanowires, reasons for dumbbell-shaped cross section and why crack is always perpendicular to [110] direction. We therefore modeled Li diffusion coupled to elasto-plastic deformation with anisotropic effect.

8.3 Model description

We have performed both three-dimensional (3D) and two-dimensional (2D) simulations to explore the effects of lithiation on the morphology changes and fracture in Si nanowires. To simulate the development of the core-shell structure, we implemented a Li diffusion model with the Li concentration-dependent free energy. Such an energy needs to have double wells for capturing the coexisting states of pristine Si (i.e., the ratio of Li to Si $x \approx 0$) and fully lithiated Si ($x \approx 3.75$, corresponding to the $Li_{15}Si_4$ phase). Note that our simulations mainly serve to generate a sequence of core-shell structures for the mechanics analyses of deformation and fracture, rather than providing a precise description of the mechanisms of the dynamic lithiation process. To this end, we simply employed the regular solution model with a double-well free energy of the form

$$f = \Omega c(1-c) + \left[c \ln c + (1-c)\ln(1-c)\right] \qquad \textbf{(1)}$$

where *c* denotes the normalized Li concentration, i.e., the actual Li concentration divided by the Li concentration in the fully lithiated state ($x = 3.75$). In Eq. (1) the single parameter Ω controls the equilibrium concentrations at the minimum of the two wells. We took $\Omega = 3$, so that $c = 0.07$ for pristine Si and $c = 0.93$ for fully lithiated Si. It follows that the diffusivity, *D*, was taken to be non-

linearly dependent on *c*, i.e., $D = -D_0 c d^2 f / dc^2 = D_0\left[2\Omega c - 1/(1-c)\right]$**, where** D_0 **is the diffusivity constant. Moreover, in order to account for the influence of crystalline Si, the Li diffusivity was assumed to be orientation-dependent. Among the non-zero direct components of diffusivity,** D_{ij}**, our numerical experiments indicated that** D_{11} **in the [**$1\,\bar{1}\,0$**] direction should be about 100 times** D_{22} **in the [**$11\,\bar{1}$**] direction. As detailed later, such anisotropic diffusivities play a critical role in the formation of the dumbbell-shaped cross section.**

We adopted an elastic and perfectly plastic model to describe the lithiation-induced deformation. The increment of the total strain, $d\varepsilon_{ij}$**, is taken to be the sum of three contributions[S5],**

$$d\varepsilon_{ij} = d\varepsilon_{ij}^{c} + d\varepsilon_{ij}^{e} + d\varepsilon_{ij}^{p} \qquad \textbf{(2)}$$

In Eq. (2), the increment of the lithiation-induced chemical strain, $d\varepsilon_{ij}^{c}$**, is proportional to the increment of the normalized Li concentration,** $d\varepsilon_{ij}^{c} = \beta_{ij} dc$**. Here** β_{ij} **represents the expansion coefficient with non-zero direct components, and they are controlled by the atomic processes near the lithiation reaction front and are expected to be anisotropic for lithiation of *c*-Si. Since a mechanistically-based assignment of** β_{ij} **is beyond the scope of this work, we performed numerical experiments to determine** β_{ij} **by adjusting** β_{ij} **to give a close fit of the measured geometry of fully lithiated Si nanowires. By this procedure, we obtained** $\beta_{11} = 150\%$ **in <110>,** $\beta_{22} = 40\%$ **in <111>, and** $\beta_{33} = 0$ **in <112> directions.**

In Eq. (2), the increment of the elastic strain, $d\varepsilon_{ij}^{e}$**, obeys Hooke's law,** $d\varepsilon_{ij}^{e} = \left[(1+\nu) d\sigma_{ij} - \nu d\sigma_{kk}\delta_{ij}\right]/E$**, where *E* is Young's modulus and *v* is Possion's ratio,** $\delta_{ij} = 1$ **when** $i = j$**,** $\delta_{ij} = 0$ **otherwise, and the repeated index means summation. Our elasticity model accounts for the Li concentration-dependent *E* and *v*; for fully lithiated Si,** $E = 80$**GPa,** $\nu = 0.28$**, and for pristine Si,** $E = 30$**GPa,** $\nu = 0.24$**; both *E* and *v* linearly vary between the two limits as suggested by recent first-principles calculations [24].**

In Eq. (2), the increment of the plastic strain, $d\varepsilon_{ij}^{p}$**, was assumed to obey the classic J_2-flow rule; namely plastic yielding occurs when the von Mises equivalent stress,** $\sigma_{eq} = \sqrt{3 s_{ij} s_{ij} / 2}$**, equals the**

yield stress σ_Y. Here $s_{ij} = \sigma_{ij} - \sigma_{kk}\delta_{ij}/3$ is the deviatoric stress; $d\varepsilon_{ij}^{p}$ is proportional to s_{ij} and can be determined by solving the boundary value problem.

We numerically implemented the above diffusion and elastic-plastic model by using the finite element package ABAQUS 6.10. The 3D simulation can well capture the overall wire deformation and development of the tapering core-shell structure, while the 2D cross-sectional simulation (with fine meshes) enables the quantification of geometry of a fully lithiated nanowire, which is consistent with experimental measurements. The Li and stress-strain fields were incrementally updated using an implicit coupled temperature-displacement procedure in ABAQUS/Standard [203]. Specifically, the lithiation-induced strain was simulated by a thermal strain approach. That is, the normalized concentration was surrogated by temperature and the expansion coefficient β_{ij} was equivalently treated as the thermal expansion coefficient. The user material subroutine for heat transfer (UMATHT) was programmed to interface with ABAQUS for updating diffusivities based on the current Li concentration (i.e., temperature). The Li distribution was then updated and so was the increment of the elastic-plastic deformation. In order to numerically stabilize the large distortions at both the reaction front and growing neck, small rate sensitivity was used by assigning the exponent of 500 for the over-stress power law model of rate-dependent viscoplasticity [25].

In the 2D cross-sectional simulations, the plane-strain condition was assumed on the basis of the negligible axial deformation observed in experiments. We used the 4-node plane strain element with thermally coupled quadrilateral, bilinear displacement and temperature (CPE4T). The in-plane boundary conditions were taken as a constant Li concentration ($c=1$) and zero tractions at the outer boundary. Utilizing the symmetry condition, one quarter of the wire was modeled to reduce the computation cost. For 3D simulations, the Li surface flux was prescribed at one end of the wire and a skin layer was additionally attached to the wire surface. To mimic the fast Li diffusion at the surface, the Li diffusivity in this skin layer was 300 times that in the bulk. The simulation of development of the core-shell structure (Movie S8) agrees with *In situ* TEM observations. In addition, the 3D simulation of distributions of the Li concentration and stresses are consistent with the results from 2D cross-sectional simulations. Such a close correlation can be understood by noting that our double-well free energy model (Eq. 1) essentially forces the normalized Li concentrations to be close to either zero (pristine Si) or one (fully lithiated Si). As a consequence, the in-plane diffusion in 3D simulations

occurs mostly under the condition of a fully-lithiated surface, which is the boundary condition in 2D simulations. Both our 2D and 3D simulations well captured the main features of the morphology changes in experiments.

8.4 Results and discussion

To understand the cracking of the lithiated nanowire, a first priority is to know the stress state inside the nanowire. We modeled Li diffusion coupled to elasto-plastic deformation (*Figure* 6a). The diffusion was described by a Li concentration-dependent free energy with double wells, at Li/Si ratios, *x*, of $x \approx 0$ and $x = 3.75$, respectively. Figure 6b shows the simulated Li distribution in the wire, demonstrating the progressive development of the three-dimensional tapered *c*-Si core (*Figure* 6c). Note that in the (112) cross section, the lithiation reaction front (i.e., the core-shell interface) moves faster in the $[1\bar{1}0]$ direction than the $[11\bar{1}]$ direction. This arises because the apparent Li diffusivity was taken to be 100 times larger in $[1\bar{1}0]$ than $[11\bar{1}]$ (achieving best agreement with the experimentally observed cross-section shape). As a result of the large diffusion anisotropy, the shrinking *c*-Si core evolves into the $[11\,\bar{1}]$-elongated shape (*Figure* 6d), consistent with experimental observation (*Figure* 7).

The progressive lithiation can readily cause the buildup of high stresses, leading to plastic deformation [26]. In a first approximation, we adopted an elastic - perfectly plastic model [27] with a yield stress of 3 GPa. Our simulations clearly show the lithiation-induced anisotropic expansion, plastic flow of the lithiated shell and onset of necking instability, leading to the formation of a dumbbell-shaped cross section. Figure 7 lists the simulated cross-sectional geometry of a fully lithiated wire, in close agreement with experimental measurements. Figure 6e shows the contour of the von Mises stress (red indicates attainment of the plastic yield stress) at a post-necking stage. In *Figure* 3, the formation of surface cracks was observed at the cross section with full lithiation, where the Si core just disappeared. To explain this fracture mode, we note that the present necking instability is driven by the *internal* expansion associated with lithiation of the Si core. Because of the absence of the external load, the resultant force at any plane of the wire has to be zero, such that both the tensile and compressive stresses must coexist. Figure 6f confirms such mechanics principle by showing the distribution of the stress component normal to the nanowire axis, σ_{11}, at a typical post-

necking deformation stage; on a central x_2 - x_3 plane (x_1 = 0). The stress is tensile near the surface indent and compressive in the Si core (Figs. 9c and d). The former tends to drive the growth of the neck and facilitate the initiation of a surface crack, while the latter resists this crack initiation. As lithiation proceeds, the *c*-Si core is reduced, leading to diminishment of the region of compressive stress. The vanishing region of compressive stress near the center of the wire allows the unstable growth of the indent that progresses to form cracks and may eventually lead to a splitting of the wire.

Our numerical models suggest that anisotropic lithium diffusion likely plays a critical role in the formation of the dumbbell-shaped cross section (*Figure* 8). Of particular note is the influence of the Li diffusivity anisotropy. Figure 8 shows that an increase of such anisotropy can promote the elongation of the shrinking Si core in the [$11\bar{1}$] direction, which is fundamentally needed to facilitate the necking instability. If the diffusivity of lithium in [110] direction is not significantly smaller than it in [111] direction, such as $D_{[111]}=0.2D_{[110]}$, no tapering at the surface. Hence, the necking instability is consequently suppressed (Fig 8b). Specifically, in References to the coordinate system in *Figure* 5a, let us focus on the lithiated shell near the apex of the cross section. If the thickness of such a shell, measured in the x_2 direction of [$11\bar{1}$], can increase significantly with x_1, it will generate a large variation of the outward surface displacement, which increases with x_1. As a result, the top surface will gradually become flat and slightly indented. The ensuing local stress concentration at the indent facilitates the onset of a necking instability. Further post-necking deformation can lead to the formation of the observed dumbbell-shaped cross section. The physical origin of such large diffusion anisotropy for Li is not well understood, but it is expected to be controlled by interfacial processes.

Figure 6. Simulated Li and stress distributions in a [112]-oriented Si nanowire. (a) 3D simulation of a progressively lithiated nanowire (i.e., the Li flux is prescribed at the front end), showing the development of the dumbbell-shaped cross section along the longitudinal direction. The contour indicates the normalized Li concentration, *c*, defined as the actual Li concentration divided by the Li concentration in the fully lithiated state (*x* = 3.75). (b) The wire is cut to expose the Li distribution in the ($11\,\bar{1}$) cross section, showing the tapered Si core structure, which is consistent with the TEM image of (c). (d) The Li distribution, *c*, in the (112) cross section at a representative post-necking stage, showing the [$11\,\bar{1}$]-elongated Si core. The black circle indicates the initial cross section of the pristine Si nanowire. (e) Corresponding distribution of the von Mises equivalent stress, $\sigma_{eq} = \sqrt{3\sigma_{ij}\sigma_{ij}/2}$; the areas in red are plastically yielded. (f) Schematic of neck growth along the longitudinal direction of the nanowire. The front cross section shows the distribution of the normal stress component, σ_{11}. At the plane of $x_1 = 0$, σ_{11} is tensile near the surface indent and compressive in the center, the diminishing of central compression with increasing indent facilitates unstable necking growth (indicated by white lines) that can progress to form cracks.

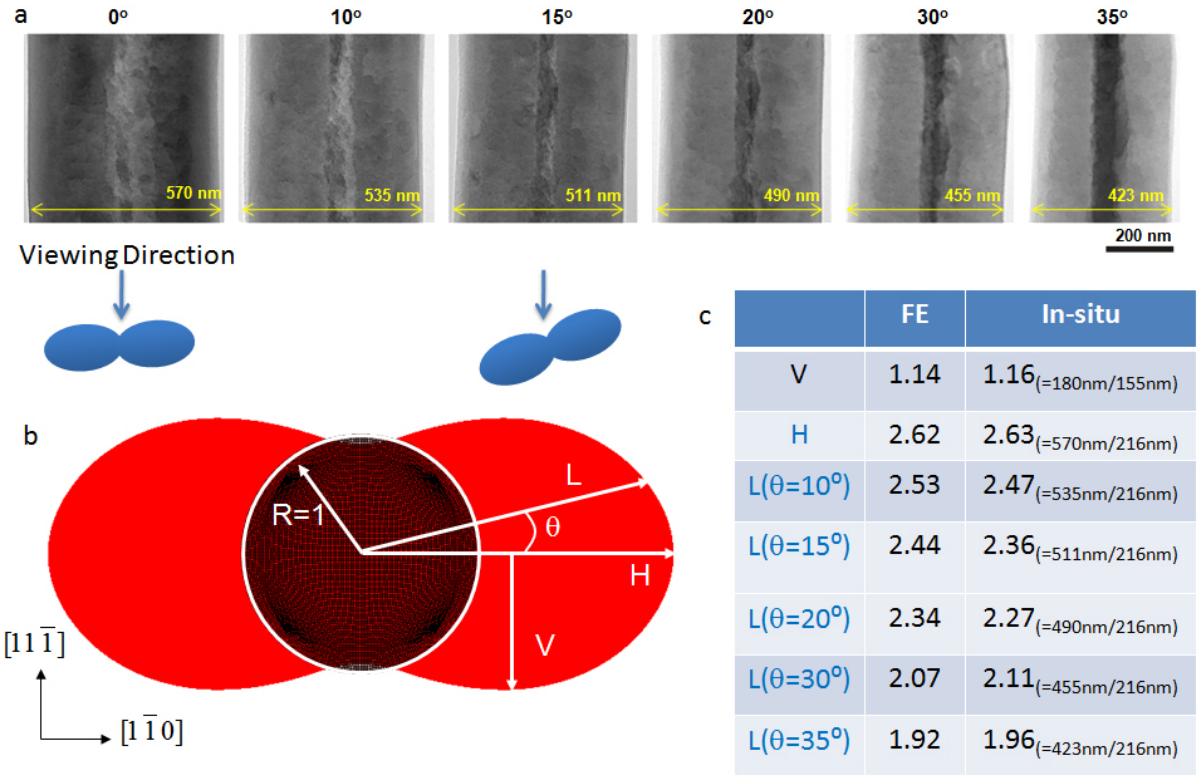

c

	FE	In-situ
V	1.14	$1.16_{(=180nm/155nm)}$
H	2.62	$2.63_{(=570nm/216nm)}$
L(θ=10°)	2.53	$2.47_{(=535nm/216nm)}$
L(θ=15°)	2.44	$2.36_{(=511nm/216nm)}$
L(θ=20°)	2.34	$2.27_{(=490nm/216nm)}$
L(θ=30°)	2.07	$2.11_{(=455nm/216nm)}$
L(θ=35°)	1.92	$1.96_{(=423nm/216nm)}$

Figure 7. Comparison of the cross-sectional geometry between experiment and simulation. (a) TEM images of the wire viewed from the side at different tilt angles. Because of the dumbbell-shaped cross section, the width of the wire, measured from the 2D projected view, changes with the viewing angle. Notice that the width of the Si core (in dark grey) increases with the viewing angle; this indicates that the cross section of the Si core has an elliptical shape. (b) The simulated cross section of a fully lithiated nanowire, showing the anisotropic volume expansion and final dumbbell cross section after full lithiation. The initial cross section of a pristine Si nanowire is represented by the circle enclosing the finite element mesh and it is superposed to highlight the morphological changes. (c) Quantitative comparison of the cross-sectional geometry between finite element method simulation and in-situ TEM measurement. The overall error is less than 4%.

Meanwhile, the physical origin of the necking instability can be revealed by analyzing the elastic-plastic deformations of the surface layer near the apex of the cross section. Upon lithiation, a compressive hoop stress first develops in this layer, due to the circumferential constraint on volume expansion (Figs. S8a, S8b). This is followed by the compressive plastic yielding with a further increase

of the local Li concentration. The layer becomes fully lithiated after the passing of the reaction front. As lithiation proceeds, the volume expansion at the lithiation front displaces the materials behind it in the outward radial direction and simultaneously stretches them in circumferential directions. As a result, the surface layer sequentially undergoes *compressive elastic unloading*, *tensile elastic loading* and *tensile plastic yielding* (Figs. 6e, 6f and Figs. 9c, 9d). This is reminiscent of the deformation sequence at the crack tip under cyclic mechanical load. It should be emphasized that the tensile plastic flow is only a necessary condition of a necking instability. Our simulations clearly show the non-uniform surface displacement near the apex of the cross section during the pre-necking deformation, mainly caused by the lithiation strain in the [$11\bar{1}$] direction and promoted by the [$11\bar{1}$]-elongated Si core (Figs. 7a, 6d). Consequently, the surface near the apex gradually becomes flat and slightly indented. Driven by the progressive lithiation of the Si core, further expansion of the lithiated shell causes the onset of a necking instability around the surface indent, followed by neck growth and formation of the dumbbell-shaped cross section, consistent with experimental observation.

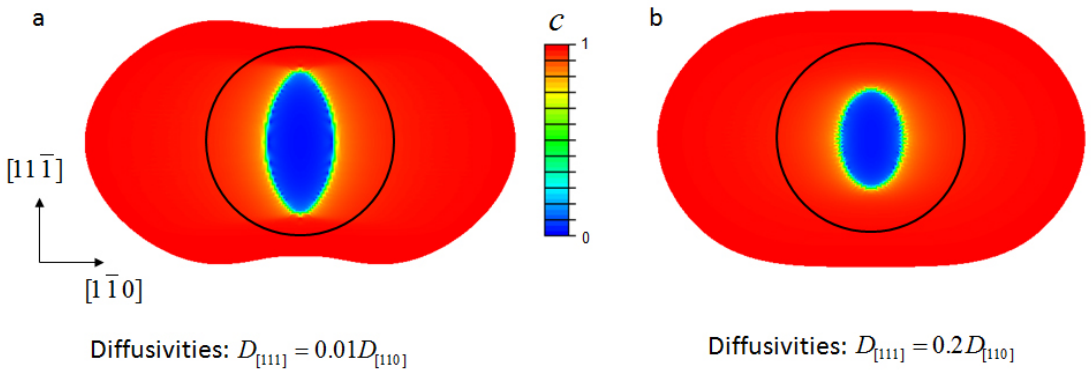

Figure 8. Comparison of the cross-sectional geometry between experiment and simulation. (a) TEM images of the wire viewed from the side at different tilt angles. Because of the dumbbell-shaped cross section, the width of the wire, measured from the 2D projected view, changes with the viewing angle. Notice that the width of the Si core (in dark grey) increases with the viewing angle; this indicates that the cross section of the Si core has an elliptical shape. (b) The simulated cross section of a fully lithiated nanowire, showing the anisotropic volume expansion and final dumbbell cross section after full lithiation. The initial cross section of a pristine Si nanowire is represented by the circle enclosing the finite element mesh and it is superposed to highlight the morphological changes.

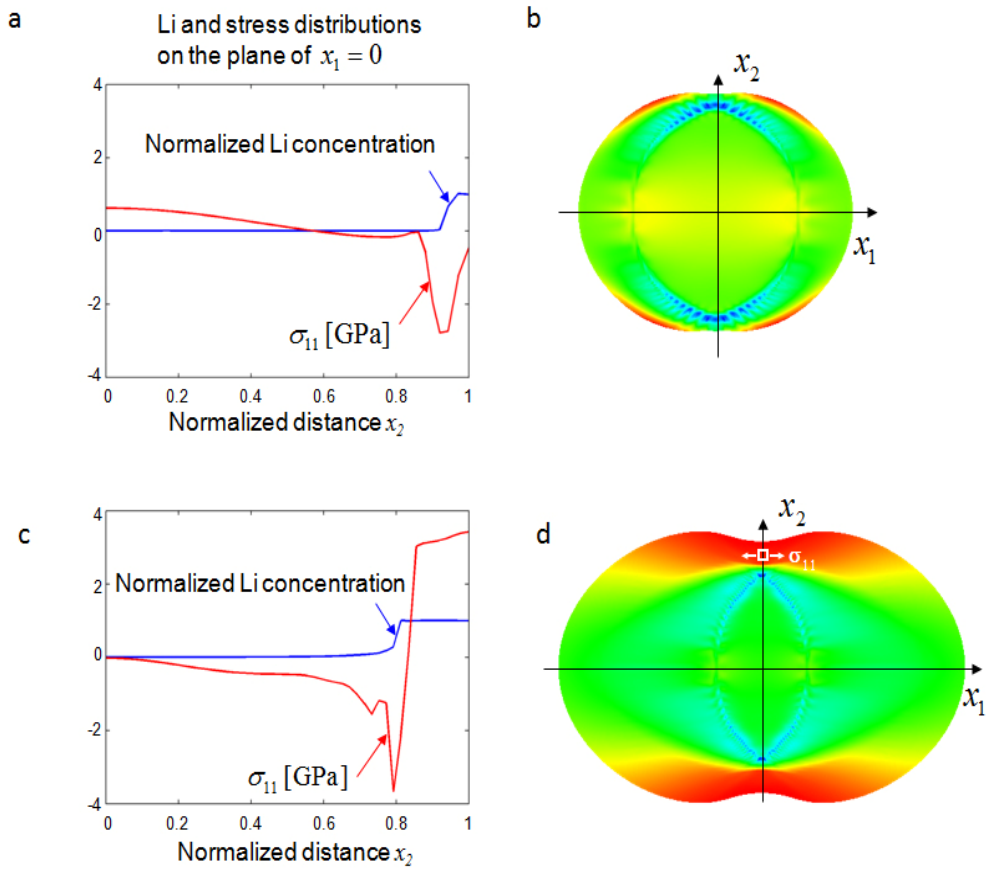

Figure 9. Distributions of Li and normal stress σ_{11} on the $x_2 - x_3$ plane at different deformation stages. (a-b) In the pre-necking stage, the lithiation reaction front (i.e. the region where the normalized Li concentration jumps from zero to one) is close to the surface, and σ_{11} is compressive near the surface and tensile in the center. (c-d) In the post-necking stage, the reaction front moves towards the center; σ_{11} becomes tensile near the surface and compressive throughout the center.

We note that similar interface-mediated anisotropic responses have been widely observed in both oxidation and wet etching of *c*-Si [28-29]. Understanding its mechanistic basis requires a systematic study of lithiation reactions, accounting for factors such as the interfacial reactive layer [30], the bond density and states near the interface [28], stress effects on reaction and diffusivity [31], etc. In addition, to capture the anisotropic expansion of the wire, we have also taken the anisotropic lithiation-induced strain, i.e., 150% in $[1\,\bar{1}\,0]$ and 40% in $[11\,\bar{1}]$ at the lithiation limit of *x* = 3.75. This

anisotropic response can be similarly governed by the interfacial reaction, requiring further study for revealing its mechanistic origin [32].

8.4 Conclusion

***in situ* TEM experiments by Dr. Jianyu Huang have revealed that the large volume expansion as Si converts to $Li_{15}Si_4$ occurs in a highly anisotropic fashion in free-standing nanowires of <112> growth directions, resulting in a dumbbell-shaped wire. A finite element model, based on our theoretical framework presented in chapter 7, is utilized to explain the experimental observations and predict the lithiation-induced fractures. Anisotropic diffusion and expansion play important roles in this system. Despite extensive plastic flow in the lithiated materials, very large stresses nonetheless developed inside the nanowire, leading to cracking or even self-splitting of a single nanowire into two sub-wires. This unusual microstructural and morphological evolution is dependent on the electrochemical driving force for lithiation. Lastly, this system exhibits linear kinetics for initial lithiation, in sharp contrast to the parabolic lithiation kinetics observed in SnO_2 nanowires, suggesting that the lithiation reaction in silicon is controlled by reaction front involved with two phases, which is not limited by the long-range diffusion of Li ions at this length scale.**

References

1. **Beaulieu, L.Y., et al., *Colossal reversible volume changes in lithium alloys.* Electrochemical and Solid State Letters, 2001. 4(9): p. A137-A140.**
2. **Chan, C.K., et al., *High-performance lithium battery anodes using silicon nanowires.* Nature Nanotechnology, 2008. 3(1): p. 31-35.**
3. **Kasavajjula, U., C.S. Wang, and A.J. Appleby, *Nano- and bulk-silicon-based insertion anodes for lithium-ion secondary cells.* Journal of Power Sources, 2007. 163(2): p. 1003-1039.**
4. **Cui, L.F., et al., *Crystalline-Amorphous Core-Shell Silicon Nanowires for High Capacity and High Current Battery Electrodes.* Nano Letters, 2009. 9(1): p. 491-495.**
5. **Park, M.H., et al., *Silicon Nanotube Battery Anodes.* Nano Letters, 2009. 9(11): p. 3844-3847.**
6. **Zhang, Q., et al., *Lithium Insertion In Silicon Nanowires: An ab Initio Study.* Nano Letters, 2010: p. 3243-3249.**
7. **Teki, R., et al., *Nanostructured Silicon Anodes for Lithium Ion Rechargeable Batteries.* Small, 2009: p. 2236-2242.**
8. **Limthongkul, P., et al., *Electrochemically-driven solid-state amorphization in lithium-metal anodes.* Journal of Power Sources, 2003: p. 604-609.**
9. **Limthongkul, P., et al., *Electrochemically-driven solid-state amorphization in lithium-silicon alloys and implications for lithium storage.* Acta Materialia, 2003. 51(4): p. 1103-1113.**
10. **Chevrier, V.L., J.W. Zwanziger, and J.R. Dahn, *First principles study of Li-Si crystalline phases: Charge transfer, electronic structure, and lattice vibrations.* Journal of Alloys and Compounds, 2010. 496(1-2): p. 25-36.**
11. **Ng, S., et al., *Highly reversible lithium storage in spheroidal carbon-coated silicon nanocomposites as anodes for lithium-ion batteries.* Angewandte Chemie-International Edition, 2006: p. 6896-6899.**
12. **Key, B., et al., *Real-Time NMR Investigations of Structural Changes in Silicon Electrodes for Lithium-Ion Batteries.* Journal of the American Chemical Society, 2009. 131(26): p. 9239-9249.**
13. **Beattie, S.D., et al., *Si electrodes for li-ion batteries - A new way to look at an old problem.* Journal of the Electrochemical Society, 2008. 155(2): p. A158-A163.**
14. **Larcher, D., et al., *Recent findings and prospects in the field of pure metals as negative electrodes for Li-ion batteries.* Journal of Materials Chemistry, 2007: p. 3759-3772.**
15. **Tarascon, J.M. and M. Armand, *Issues and challenges facing rechargeable lithium batteries.* Nature, 2001. 414(6861): p. 359-367.**
16. **Zhou, S., X.H. Liu, and D.W. Wang, *Si/TiSi2 Heteronanostructures as High-Capacity Anode Material for Li Ion Batteries.* Nano Letters, 2010. 10(3): p. 860-863.**
17. **Huggins, R.A. and W.D. Nix, *Decrepitation model for capacity loss during cycling of alloys in rechargeable electrochemical systems.* Ionics, 2000. 6: p. 57-63.**
18. **Huang, J.Y., et al., *In Situ Observation of the Electrochemical Lithiation of a Single SnO2 Nanowire Electrode.* Science, 2010. 330(6010): p. 1515-1520.**
19. **Yamamoto, K., et al., *Dynamic Visualization of the Electric Potential in an All-Solid-State Rechargeable Lithium Battery.* Angewandte Chemie-International Edition, 2010. 49(26): p. 4414-4417.**
20. **Chiang, Y.M., *Building a Better Battery.* Science, 2010. 330(6010): p. 1485-1486.**

21. **Obrovac, M.N. and L. Christensen, *Structural changes in silicon anodes during lithium insertion/extraction.* Electrochemical and Solid State Letters, 2004. 7(5): p. A93-A96.**
22. **Obrovac, M.N. and L.J. Krause, *Reversible cycling of crystalline silicon powder.* Journal of the Electrochemical Society, 2007. 154(2): p. A103-A108.**
23. **Hatchard, T.D. and J.R. Dahn, *In situ XRD and electrochemical study of the reaction of lithium with amorphous silicon.* Journal of the Electrochemical Society, 2004. 151(6): p. A838-A842.**
24. **Shenoy, V.B., P. Johari, and Y. Qi, *Elastic softening of amorphous and crystalline Li-Si Phases with increasing Li concentration: A first-principles study.* Journal of Power Sources, 2010. 195(19): p. 6825-6830.**
25. ***ABAQUS/Standard 6.10, User's Manual.* SIMULIA, Providence, R.I., 2010.**
26. **Sethuraman, V.A., et al., *In situ measurements of stress evolution in silicon thin films during electrochemical lithiation and delithiation.* Journal of Power Sources, 2010. 195(15): p. 5062-5066.**
27. **Zhao, K.J., et al., *Inelastic hosts as electrodes for high-capacity lithium-ion batteries.* Journal of Applied Physics, 2010, in press. 108(7).**
28. **Seidel, H., et al., *Anisotropic etching of crystalline silicon in alkaline-solutions .1. Orientation dependence and behaviro of passivation layers.* Journal of the Electrochemical Society, 1990. 137(11): p. 3612-3626.**
29. **Wu, B.Q., A. Kumar, and S. Pamarthy, *High aspect ratio silicon etch: A review.* Journal Of Applied Physics, 2010. 108(5).**
30. **Mott, N.F., et al., *Oxidation of silicon* Philosophical Magazine B, 1989. 60(2): p. 189-212.**
31. **Haftbaradaran, H., et al., *Continuum and atomistic models of strongly coupled diffusion, stress, and solute concentration.* Journal of Power Sources, 2011. 196(1): p. 361-370.**
32. **Hsueh, C.H. and A.G. Evans, *Oxidation-induced stress and some effects on the behavior of oxide-films.* Journal of Applied Physics, 1983. 54(11): p. 6672-6686.**

9. CONTROLLING THE LITHIATION INDUCED STRAIN AND CHARGING RATE IN NANOWIRE ELECTRODES BY COATING

As discussed in chapter 7 and 8, one major roadblock in the development of high-capacity lithium-ion batteries (LIB) is the fracture of electrodes, leading to capacity loss. Such failure is initiated by the large volume expansion associated with lithium ion insertion into the electrode materials. The battery community has been long searching for strategies to mitigate these adverse effects. Many methods have been proposed to address this problem by *externally* adding a buffer material to adapt the volume change of the active electrode material, but little has been done to *internally* modify the charging behavior of the electrode material itself.

Recently, it is reported that applying a thin layer of carbon or aluminum coating onto individual tin oxide nanowires has significant effect on improving electrode performance. As a result, there was no excess stress thus any dislocation cloud near the reaction front. This is different with our previous knowledge during the lithiation of tin oxide nanowires without coating. The external coatings can change, rather than adapt, the large volume change during lithiation. This is significant because it provides a simple yet efficient way to control the lithiation-induced-strain (LIS). This method is also general similar effects have been demonstrated when the coating material was changed from carbon to aluminum. Besides the confinement effect, the conductive carbon or aluminum coating layers also enhance the charging rate by ~ 10 times compared to that of SnO_2 nanowires without any coating. This is due to improved electronic conductivity which is highly desirable for high-power applications.

9.1 Introduction

The advanced battery system is critically important for a wide range of applications, from portable electronics to electric vehicles [1]. Lithium ion batteries (LIBs) are presently the best performing one, but they cannot meet requirements for more demanding applications due to limitations in capacity, charging rate and reliability [2-9]. One leading cause of those limitations is the lithiation-induced-strain (LIS) in electrodes, resulting in high stress and fracture [10-12]. Here we

report that by utilizing the coating strategy, both the charging rate and LIS of SnO_2 nanowire electrodes can be altered dramatically. The carbon or aluminum coated nanowires can be charged about 10 times faster than the non-coated ones. Intriguingly, the radial expansion of the coated nanowires was completely suppressed, resulting in enormously reduced tensile stress at the reaction front, as evidenced by the lack of formation of dislocations. These improvements were attributed to the effective electronic conduction and mechanical confinement of the coatings. Our work demonstrates that nanoengineering the coating enables the simultaneous control of electrical and mechanical behaviors of electrodes, pointing to a promising route for building better LIBs.

Operating a LIB depends critically on a concord transport of electrons and ions through multi-components of the battery and the mechanical stability of the system during charging and discharging. Cathodes and anodes materials used for LIBs are mostly intrinsic poor electron conductors [13-14]. It is a common practice to incorporate conductive materials, such as carbon [15-18], into the electrode to improve the electrical conductance [19-20]. However, consequences of such a coating on other key aspects of lithiation related mechanisms have never been studied in a controlled fashion [21-22]. It is far from clear how such a conductive coating layer will affect the electrochemically induced mechanical behavior, which is a critical factor limiting the capacity and reliability in LIBs.

To achieve better mechanical robustness and power performance, coating is used as a simultaneous control of lithiation strain and charging rate. Recently, our collaborator Dr. Jianyu Huang's group report an in situ nano-battery study of the dramatic effect of carbon and aluminum coating on both the lithiation rate and mechanical confinement associated with the electrochemically induced volume changes in a model system of SnO_2 nanowire.

9.2 In situ experiment observations

The in situ experiment is performed by our collaborator Dr. Jianyu Huang from Sandia national lab. A schematic illustration of the carbon coated SnO_2 single nanowire battery is shown *Figure* 1. A few SnO_2 nanowires were attached to an aluminum (Al) rod with conductive silver epoxy, while a bulk $LiCoO_2$ film on an Al foil served as the cathode. One drop of the ionic liquid electrolyte [ILE, 10 wt% lithium bis (trifluoromethylsulfonyl) imide (LiTFSI) dissolved in 1-butyl-1-methylpyrrolidinium bis

(trifluoromethylsulfonyl) imide ($P_{14}TFSI$)] was placed on the surface of $LiCoO_2$ film as the electrolyte [23]. A constant potential of -3.5 V was applied to the SnO_2 nanowire against $LiCoO_2$ upon charging [24].

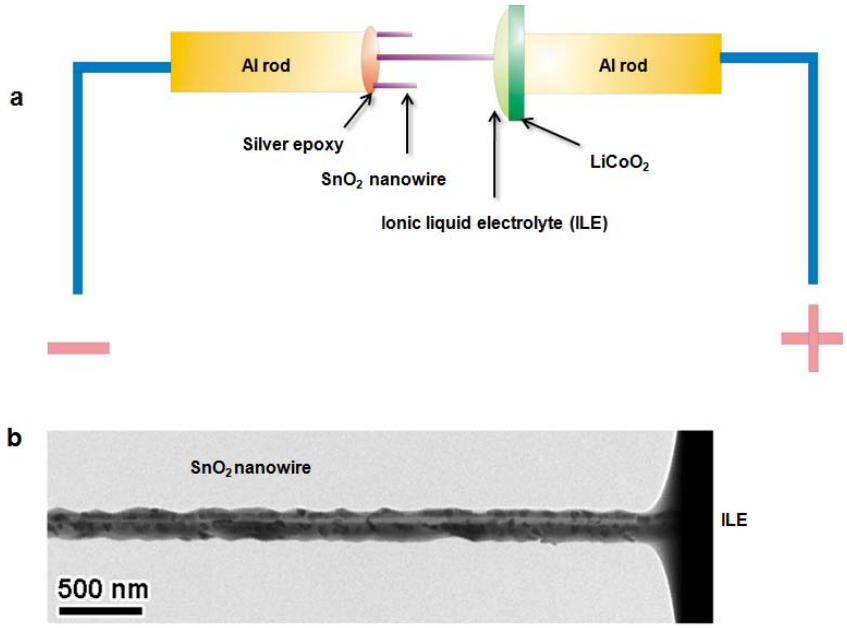

Figure 1. (a) Schematic illustration of the *in situ* experimental setup. SnO_2 nanowires were attached to an Al rod and manipulated to approach the ionic liquid electrolyte (ILE) placed on a bulk $LiCoO_2$ cathode. (b) TEM image showing a SnO_2 nanowire contacting the ILE.

Figure 2 shows the morphological evolution of a SnO_2 nanowire without carbon coating during charging. The pristine SnO_2 nanowire was initially straight and uniform in diameter (*Figure* 2a). As the reaction fronts (marked by the red triangles) propagated from the right to the left, the SnO_2 nanowire swelled and bent (Figs. 2a-2j). The overall structural evolution of the pristine SnO_2 was reported in detail in a previous publication [23], which was characterized by a total volume expansion of ~ 240% with ~ 45% radial and ~ 60% axial elongation, respectively. The charging process was very slow, and the reaction front migrated at an average speed of ~ 0.6 nm/s. Figures 1k-1p show the typical microstructure change of a SnO_2 nanowire during lithiation. The pristine SnO_2 nanowire was single crystalline (Figs. 2k-2m), which turned to grey-contrasted amorphous (*Figure* 2n) after lithiation. The electron diffraction pattern (EDP) from the lithiated part confirmed the formation of Li_2O, Sn and Li_xSn phases (*Figure* 2p). The lithiation should proceed in two steps: (1) $4Li^+ + SnO_2 + 4e^- \rightarrow 2Li_2O + Sn$; and

(2) $Sn + x\ Li^+ + x\ e^- \leftrightarrow Li_xSn$ ($0 \leq x \leq 4.4$). The volume expansion after lithiation was obvious in both the axial

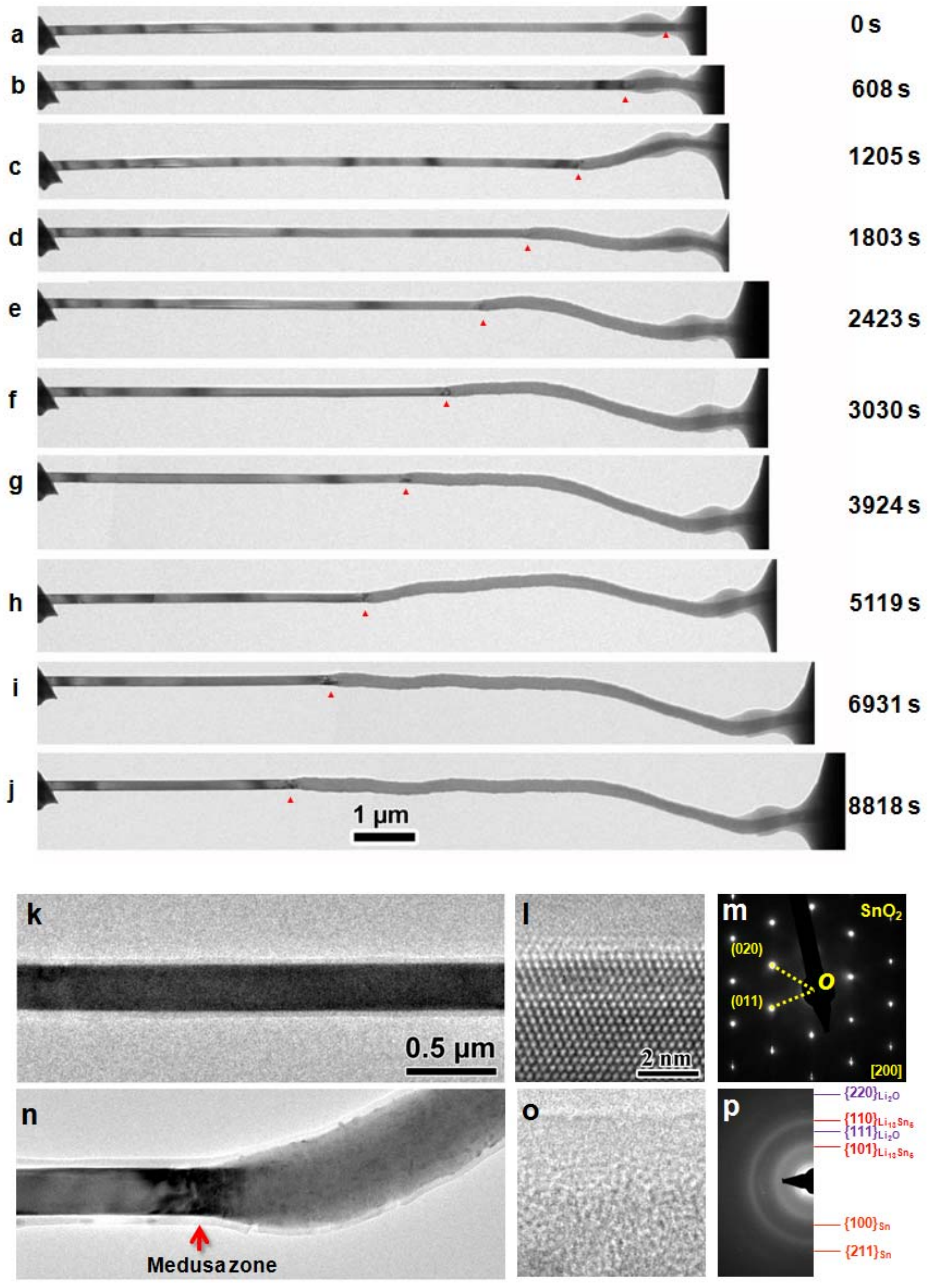

Figure 2. Charging behavior of SnO_2 nanowires without carbon coating. (a-j) Morphology evolution of a SnO_2 nanowire during charging. As the reaction front (marked by red triangles) passed by, the originally straight nanowire swelled and expanded in both radial and axial directions. The reaction

fronts were heavily strained. (k-m) Microstructure of a pristine SnO_2 nanowire showing single crystal nature. (n-p) Microstructure of the same SnO_2 nanowire after lithiation.

and radial directions (Figs. 2a-2j, 2n). As long as the radial expansion was obvious, a Medusa zone with a high density of dislocations was observed in the reaction front due to the high local stress (*Figure* 2n) which developed due to the large mismatch between the reacted and non-reacted segments of the nanowire.[23]

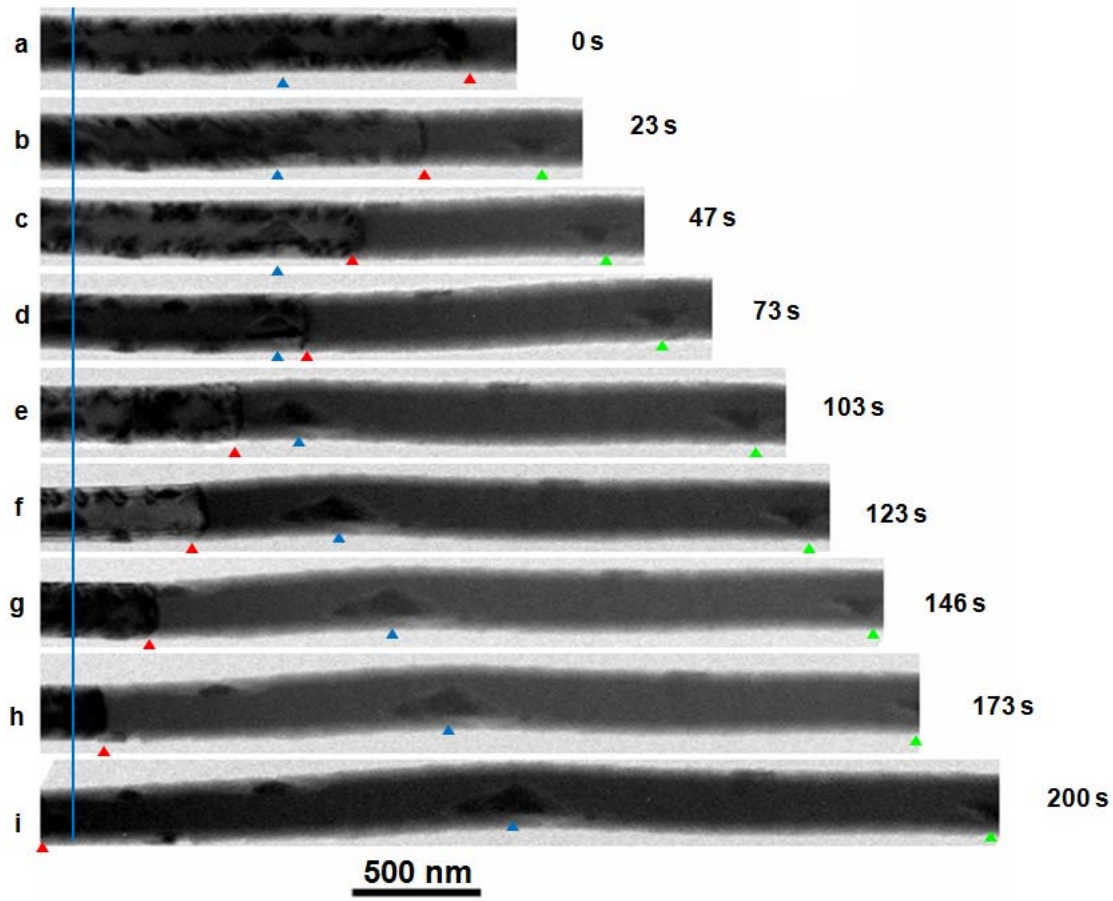

Figure 3. Charging behavior of a carbon-coated SnO_2. The red triangles mark the reaction fronts, while the blue and green triangles mark the two Sn particles' positions, indicating ~ 100% elongation during lithiation.

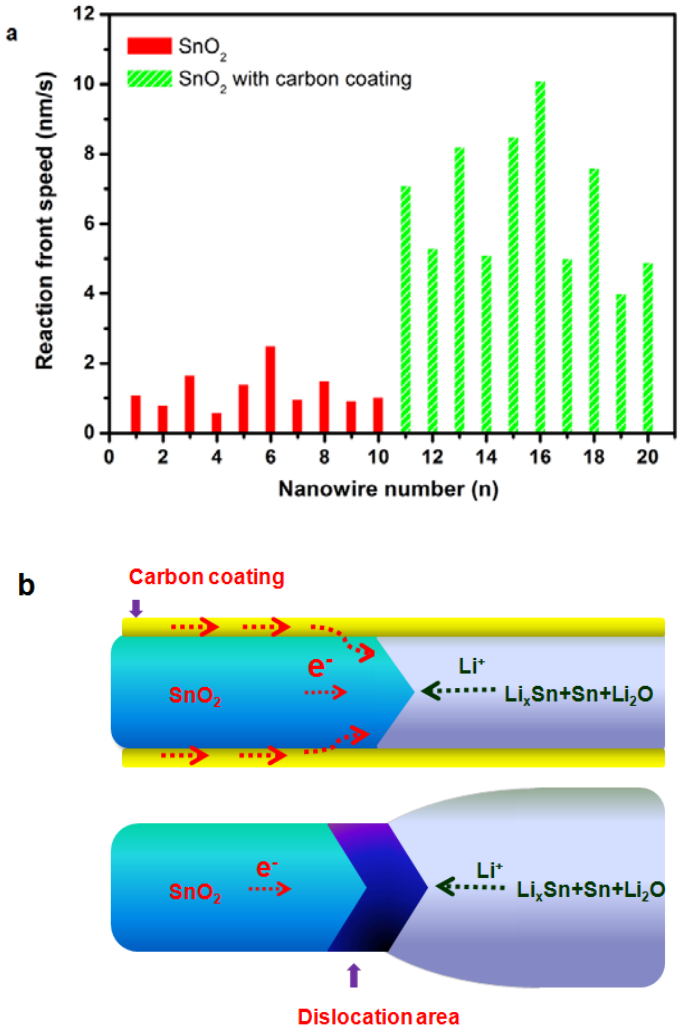

Figure 4. Comparison of charging speed and lithiation mechanism between the C-coated and pristine SnO_2 nanowires. (a) Statistics of the reaction front migration speeds. (b) Lithiation mechanisms. The carbon coating provided additional and predominant channels for electron transport, enhancing the charging rate. It also defined the volume expansion to occur exclusively along the longitudinal direction.

The lithiation behavior of a carbon-coated SnO_2 nanowire was significantly different from the one in the non-coated nanowires. Figures 3a-i show the lithiation process of a carbon coated SnO_2 nanowire. It is seen that no detectable radial expansion occurred, but the nanowire did elongate by ~ 160%. This is in contrast to the lithiation of non-coated nanowires, in which both radial expansion (~45%) and axial elongation (~60%) occurred. Furthermore, the reaction fronts (marked by red

triangles) did not have any visible dislocations (Figs. 3a-3c), which was again in contrast to the non-coated SnO_2 nanowire, in which a Medusa zone containing high density of dislocations was always presented (*Figure* 1n). Evidenced by the position change of a particle attached to the surface of the nanowire (marked by the blue triangles), the elongation of the nanowire pushed the lithiated part into the ILE. The reaction front migrated at a speed of 7.7 nm/s, which is about ten times higher than that without carbon coating.

Figure 4a compares the lithiation rates of the carbon-coated and pristine SnO_2 nanowires. On average, the reaction front of the carbon coated nanowires moved ten times faster than that of the non-coated SnO_2 nanowires. The effects of a carbon layer on SnO_2 charging include: (1) higher electron transport thus faster lithiation (*Figure* 3b); and (2) suppressed radial expansion and exclusive elongation. As a result of the latter, no dislocation cloud was seen for the carbon-confined SnO_2 nanowires (*Figure* 4b).

9.3 Model description

We used a similar model as described in chapter 7 and chapter 8 that the mechanisms of diffusion and deformation. Diffusion is derived from a Li concentration-dependent free energy, which has double wells for capturing the coexisting states of pristine and fully lithiated phases.

$$f = \Omega c(1-c) + \left[c\ln c + (1-c)\ln(1-c)\right] \qquad \textbf{(1)}$$

where *c* denotes the normalized Li concentration, i.e., the actual Li concentration divided by the Li concentration in the fully lithiated state. Deformation is the sum of three contributions,

$$d\varepsilon_{ij} = d\varepsilon_{ij}^{c} + d\varepsilon_{ij}^{e} + d\varepsilon_{ij}^{p} \qquad \textbf{(2)}$$

In Eq. (2), the increment of the lithiation-induced chemical strain, $d\varepsilon_{ij}^{c}$, is proportional to the increment of the normalized Li concentration, $d\varepsilon_{ij}^{c} = \beta_{ij} dc$. Here β_{ij} represents the expansion coefficient with non-zero direct components, and $\beta_{rr} = 45\%$, $\beta_{\theta\theta} = 45\%$, and $\beta_{zz} = 60\%$. The lithiation-induced strain in carbon coating is much smaller and was considered negligible (zeros for β_{ij}).

One significant modification is employed for coated tin-oxide nanowires. To accommodate the large volume expansion in the coated wire, the lithiated material was extruded out of the stress-free end of the thin-walled cylindrical coating. The extrusion process involved the complicated interfacial behaviors between the lithiated material and coating, e.g. large shear deformation, interfacial fracture, frictional sliding, loss of interfacial interaction between the extruded part and coating. In a first approximation, the interfacial response was simulated by using a stick-and-slip friction model implemented in ABAQUS. When the interfacial shear stress was larger than the critical value of 0.28GPa, the interface de-bonded and relative sliding occurred. The friction coefficient was taken as 1 and the fraction of characteristic surface dimension as 0.01.

More specifically, the increment of the elastic strain, $d\varepsilon_{ij}^{e}$**, in Eq. (2) obeys Hooke's law,** $d\varepsilon_{ij}^{e}=\left[(1+v)d\sigma_{ij}-vd\sigma_{kk}\delta_{ij}\right]/E$**, where *E* is Young's modulus and *v* is Possion's ratio,** $\delta_{ij}=1$ **when** $i=j$**,** $\delta_{ij}=0$ **otherwise, and the repeated index means summation. Our elasticity model dose not account for the Li concentration dependence of *E* and *v*, due to the lack of experimental quantification. We took the values of *E* and *v* from those of materials without lithiation, for SnO_2,** $E=200$ **GPa,** $\nu=0.3$**, and for diamond-like amorphous carbon coat,** $E=759$ **GPa,** $\nu=0.3$**. To simulate the axially symmetric response of the coated wire, we used the 4-node axisymmetric element with thermally coupled quadrilateral, bilinear displacement and temperature (CAX4T). The coating thickness was taken as 1/10th of the radius of the wire. The boundary conditions were taken as a constant Li flux at one end and zero traction at the outer boundary.**

9.4 Results and discussion

The suppression of radial expansion in the carbon coated nanowire is likely to be caused by the mechanical confinement of the surface carbon layer. To assess this constraint mechanism, we have modeled the stress buildup in the coated wire by co-evolving the Li diffusion and elasto-plastic deformation in the finite element simulation. The lithiation-induced strain was taken as 45% and 60% in the radial and axial direction, respectively, and the associated plastic deformation was assumed to obey the classic J_2-flow rule [25]. Figure 5a shows the simulated Li distribution and associated wire deformation. The simulation well captured the propagation of the lithiation reaction front in the axial

direction. It also demonstrated that due to the mechanical constraint of the carbon coating, radial expansion of the wire can be almost entirely suppressed. Moreover, in contrast to the case without coating [23], the radial tensile stress in front of the reaction front is reduced to nearly zero in the wire, while a large radial compressive stress develops behind the reaction front (*Figure* 5b). The consequence of the former stress change is to reduce the driving force, and thus the possibility, of dislocation nucleation. And that of the latter is to induce plastic flow of amorphous Li_xSn, leading to wire extrusion out of the free end of the carbon coating. Another effect of the mechanical confinement is to establish a hoop stress in the thin-walled cylindrical carbon coating. While the mechanical strength of the amorphous carbon coating is lower than that of perfect carbon nanotubes, the former can still fall between 25 ~ 90 GPa [26-27], which should be sufficient to resist against the hoop stress-induced fracture in the coating.

One key question about the carbon coating is whether it remained intact after lithiation. Figures 5c-5d show that the continuous carbon layer was broken into tiny pieces in the axial direction after charging. Those fractures occurred due to the repeated buildup of a large axial stress, σ_z^{coat}, in the thin-walled coating when lithiation proceeds. As schematically shown in *Figure* 5e, σ_z^{coat} arises mainly because of the frictional shear stress at the interface between the carbon coating and the lithiated portion of the wire which is being extruded out of the stress-free end of the coating. Assuming a constant shear stress, τ_{Y}, it is readily to show that $\sigma_z^{\text{coat}} \sim \tau_{\text{Y}} l_z / t$, where *t* is the thickness of the coat layer and l_z is the distance of the reaction front away from the stress-free end of the coating. As lithiation proceeds, l_z and accordingly σ_z^{coat}, increases. Fracture of the coating occurs in the axial direction, when σ_z^{coat} exceeds the breaking stress of the coating. Repetition of this process (i.e., the buildup of σ_z^{coat} and the fracture of the coating) left broken segments of the surface carbon layer in the downstream of the lithiation reaction front (Figs. 5d-5e).

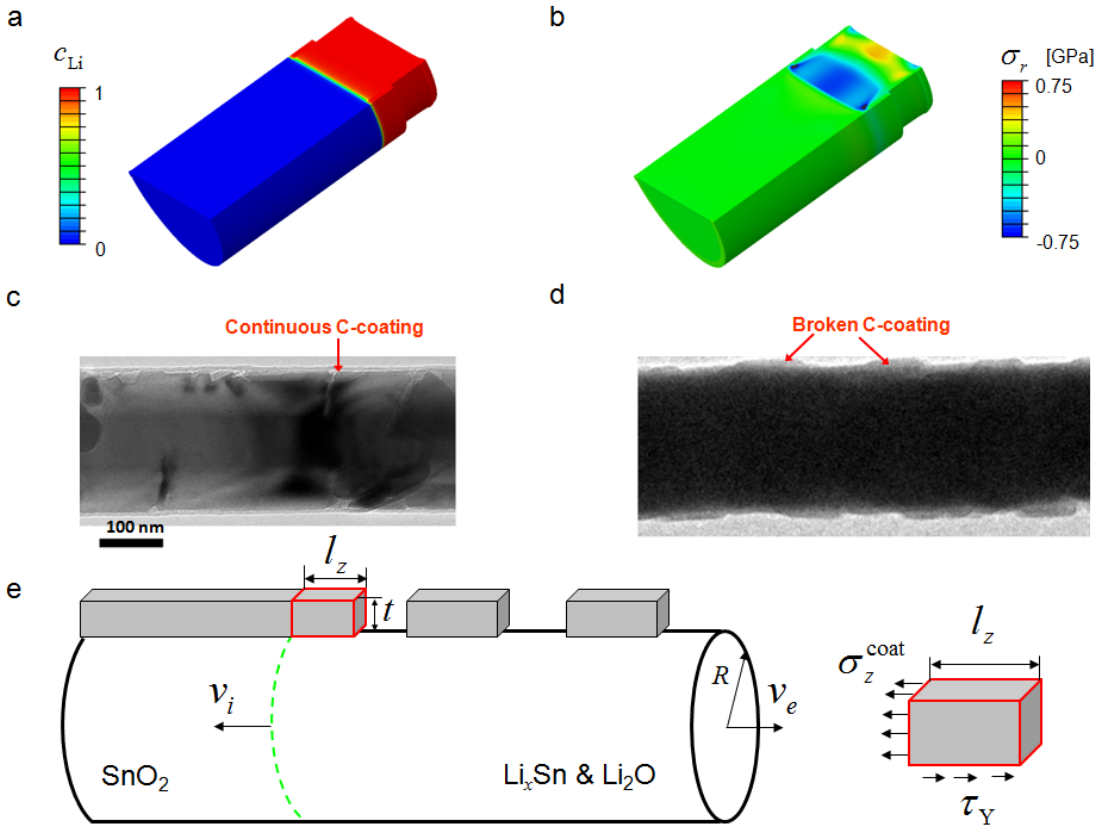

Figure 5. Simulation of Li diffusion, mechanical deformation and stress in a carbon coated SnO_2 nanowire. (a) Normalized Li concentration, C_{Li} defined as the actual Li concentration divided by the Li concentration in the fully lithiated state. The lithiation reaction front is located at the interface between pristine (blue) and lithiated (red) phases. To accommodate the volume expansion, the lithiated material is extruded out of the thin-walled cylindrical carbon coating. (b) The corresponding distribution of the radial stress σ_r. TEM images are shown for (c) the pristine SnO_2 nanowire with the continuous carbon coating and (d) the lithiated wire with the broken coating. (e) Schematic illustration of the development of the axial stress, σ_z^{coat}, in the carbon coating, leading to coat fracture. As lithiation proceeds, the reaction front moves to the left at a velocity v_i, and the lithiated materials behind the reaction front plastically flow to the right. A stress element of the coating is drawn on the side of the wire to enable a scaling analysis of σ_z^{coat}.

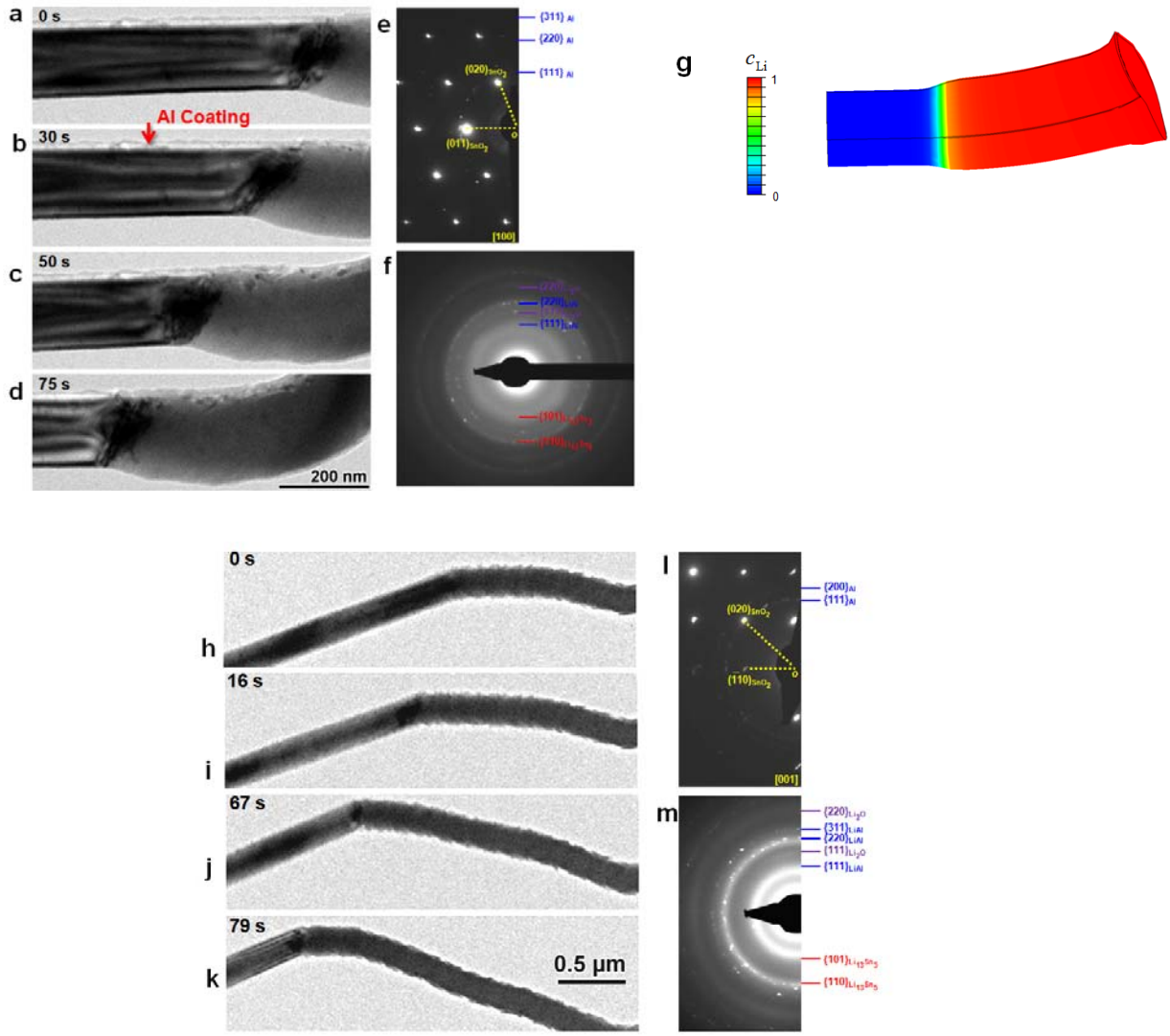

Figure 6. Lithiation behaviors of SnO_2 nanowires coated with Al layers. (a-f) Structure evolution during lithiation of a SnO_2 nanowire with one side coated with Al. The volume expansion occurred on the non-coated side but was suppressed on the coated side (a-d). (g) Simulated Li distribution and bending deformation of the partially Al-coated nanowire after lithiation. (h-m) Lithiation of a fully coated nanowire. The radial expansion was completely suppressed. The EDPs showed conversion of single-crystalline SnO_2 (e, l) to mixed amorphous phases of Sn, $Li_{13}Sn_5$ and Li_2O (f, m).

The effects of a conductive coating layer on lithiation rate enhancement and modification of shape accommodation associated with volume expansion can be extended beyond the carbon

material. As a demonstration, a 20 nm thick Al was coated onto the pristine SnO_2 nanowires and then subject to lithiation. Figures 6a-6d show the lithiation of a SnO_2 nanowire partially coated with Al on the upper side. Notably, the radial expansion took place on the side without Al coating, whereas it was suppressed on the coated side. Figure 6g shows the simulated Li distribution and deformation of the partially coated wire. It well captures the bending deformation near the reaction front, which arises because of the frictional shear stress at the interface between the coating and the lithiated wire. EDPs confirmed transformation from single-crystalline SnO_2 to a mixture of Sn, $Li_{13}Sn_5$, and Li_2O (Figs. 6f, 6m). This clearly proved that the effect of the conductive coating on facilitating the lithiation of SnO_2 nanowires. Similarly, SnO_2 nanowires with full coverage of Al coating showed enhanced charging rate (Figs. 6h-6k). The reaction front proceeded at a speed of 9 nm/s (Figs. 5h-5k). Al is a metal thus a better electron conductor than the amorphous carbon, enabling even faster lithiation rates. Similar to the case of a carbon coating, the Al coating was broken after lithiation but no radial expansion was observed.

9.5 Conclusions

In summary, it has been demonstrated that there is dramatic effects of the carbon and aluminum coatings on the lithiation behavior of individual SnO_2 nanowires. Compared to the non-coated SnO_2 nanowires, the coated SnO_2 nanowires can be charged at a rate ten times higher than that of the uncoated one due to the improved electronic conductivity. More importantly, radial expansion is completely suppressed in the coated nanowires due to the mechanical confinement of the coating layers. This study demonstrates that it is possible to simultaneously control the electrochemical reaction rate and the mechanical strain of the electrode materials through carbon or aluminum coating, opening new avenues of designing better lithium ion batteries.

References

1. **Arico, A.S., et al., *Nanostructured materials for advanced energy conversion and storage devices.* Nature Materials, 2005. 4(5): p. 366-377.**
2. **Larcher, D., et al., *Recent findings and prospects in the field of pure metals as negative electrodes for Li-ion batteries.* Journal of Materials Chemistry, 2007: p. 3759-3772.**
3. **Tarascon, J.M. and M. Armand, *Issues and challenges facing rechargeable lithium batteries.* Nature, 2001. 414(6861): p. 359-367.**
4. **Goodenough, J.B. and Y. Kim, *Challenges for Rechargeable Li Batteries.* Chemistry of Materials, 2010. 22(3): p. 587-603.**
5. **Brousse, T., et al., *Thin-film crystalline SnO2-lithium electrodes.* Journal of the Electrochemical Society, 1998. 145(1): p. 1-4.**
6. **Li, N.C., C.R. Martin, and B. Scrosati, *A high-rate, high-capacity, nanostructured tin oxide electrode.* Electrochemical and Solid State Letters, 2000. 3(7): p. 316-318.**
7. **Han, S.J., et al., *Simple synthesis of hollow tin dioxide microspheres and their application to lithium-ion battery anodes.* Advanced Functional Materials, 2005. 15(11): p. 1845-1850.**
8. **Lou, X.W., et al., *Template-free synthesis of SnO2 hollow nanostructures with high lithium storage capacity.* Advanced Materials, 2006. 18(17): p. 2325-+.**
9. **Chiang, Y.M., *Building a Better Battery.* Science, 2010. 330(6010): p. 1485-1486.**
10. **Beaulieu, L.Y., et al., *Colossal reversible volume changes in lithium alloys.* Electrochemical and Solid State Letters, 2001. 4(9): p. A137-A140.**
11. **Beaulieu, L.Y., et al., *Reaction of Li with alloy thin films studied by in situ AFM.* Journal of the Electrochemical Society, 2003. 150(11): p. A1457-A1464.**
12. **Chan, C.K., et al., *High-performance lithium battery anodes using silicon nanowires.* Nature Nanotechnology, 2008. 3(1): p. 31-35.**
13. **Chung, S.Y., J.T. Bloking, and Y.M. Chiang, *Electronically conductive phospho-olivines as lithium storage electrodes.* Nature Materials, 2002. 1(2): p. 123-128.**
14. **Kang, B. and G. Ceder, *Battery materials for ultrafast charging and discharging.* Nature, 2009: p. 190-193.**
15. **Wang, Y., H.C. Zeng, and J.Y. Lee, *Highly reversible lithium storage in porous SnO2 nanotubes with coaxially grown carbon nanotube overlayers.* Advanced Materials, 2006. 18(5): p. 645-+.**
16. **Magasinski, A., et al., *High-performance lithium-ion anodes using a hierarchical bottom-up approach.* Nature Materials, 2010. 9(4): p. 353-358.**
17. **Ng, S.H., et al., *Highly reversible lithium storage in spheroidal carbon-coated silicon nanocomposites as anodes for lithium-ion batteries.* Angewandte Chemie-International Edition, 2006. 45(41): p. 6896-6899.**
18. **Cui, L.F., et al., *Carbon-Silicon Core-Shell Nanowires as High Capacity Electrode for Lithium Ion Batteries.* Nano Letters, 2009. 9(9): p. 3370-3374.**
19. **Cheng, F., et al., *Template-directed materials for rechargeable lithium-ion batteries.* Chemistry of Materials, 2008. 20(3): p. 667-681.**
20. **Cui, L.F., et al., *Crystalline-Amorphous Core-Shell Silicon Nanowires for High Capacity and High Current Battery Electrodes.* Nano Letters, 2009. 9(1): p. 491-495.**
21. **Ravet, N., A. Abouimrane, and M. Armand, *From our readers - On the electronic conductivity of phosphoolivines as lithium storage electrodes.* Nature Materials, 2003. 2(11): p. 702-702.**

22. **Hong, J., et al.,** ***Characterization and performance of LiFePO4 thin-film cathodes prepared with radio-frequency magnetron-sputter deposition.*** **Journal of the Electrochemical Society, 2007. 154(8): p. A805-A809.**
23. **Huang, J.Y., et al.,** ***In Situ Observation of the Electrochemical Lithiation of a Single SnO2 Nanowire Electrode.*** **Science, 2010. 330(6010): p. 1515-1520.**
24. ***Atomistic States of Hydrogen in Metals*****. 2005. p. 147-302.**
25. **Zhao, K.J., et al.,** ***Inelastic hosts as electrodes for high-capacity lithium-ion batteries.*** **Journal of Applied Physics, 2011. 109: p. 016110**
26. **Espinosa, H.D., et al.,** ***Elasticity, strength, and toughness of single crystal silicon carbide, ultrananocrystalline diamond, and hydrogen-free tetrahedral amorphous carbon.*** **Applied Physics Letters, 2006. 89(7).**
27. **Fyta, M.G., et al.,** ***Insights into the fracture mechanisms and strength of amorphous and nanocomposite carbon.*** **Physical Review Letters, 2006. 96(18).**

10. SUMMARY AND RECOMMENDATIONS FOR FUTURE RESEARCH

In this thesis, significant contributions are made to understanding the chemo-mechanics of advanced materials toward efficient hydrogen storage and transportation and development of better Li-ion battery. The nano-chemo-mechanical failure problems are addressed for two green energy-carrier systems: (a) hydrogen embrittlement in the metallic containment system for hydrogen fuels under high pressure, and (b) lithiation induced stress and fracture in anode materials for lithium-ion battery, such as silicon, graphene and tin oxide.

We introduce the research background in chapter 1, and the modeling methods in chapter 2. Chapters 3 - 9 can be divided into two parts. The first part (chapter 3) presents an atomistic study of hydrogen embrittlement in metals. By using nickel as a model material, the effect of hydrogen on grain boundary decohesion is quantitatively studied. The transition from transgranular to intergranular fracture is discussed by combining the well-established valve effect and our analysis of the atomic scale effects of hydrogen embrittlement. The second part focuses on the anode materials of lithium ion battery: Chapters 4 - 6 present the atomistic study, while chapters 7 - 9 focus on the continuum level research. The nanoscale fracture mechanisms are first studied in pristine silicon (chapter 4) and graphene (chapter 5). How to avert fracture by tailoring the system size is also discussed in chapter 5. Then the chemo-mechanical effect of lithium insertion in silicon is modeled in chapter 6. We compute the volume and voltage of lithiated silicon and identify the two stages of lithiation responses. The electro-chemical origins are explained in terms of the medium-range ordering (i.e. ring statistics) of amorphous structures. In chapter 7, a continuum modeling framework is developed to characterize the stress generation in lithiated nanowires and nanoparticles, accounting for the combined effects of plastic deformation and two-phase coexistence. The applications of this framework to silicon nanowires and coated tin-oxide nanowires are presented in chapter 8 and 9, respectively. Our models successfully match the experimental results and predict how fracture initiates and evolves. Results demonstrate that it is possible to simultaneously control the electrochemical reaction rate and the mechanical strain of the electrode materials through the coating strategy, opening new avenues of designing better lithium ion batteries.

10.1 Hydrogen embrittlement

10.1.1 Summary of Chapter 3

This chapter presents a comprehensive model of hydrogen embrittlement. It quantitatively bridges the atomic structures with the weakening effect of hydrogen segregation on grain boundaries. It connects experimental measurements with the atomistic modeling and thermodynamic theory [1]. We study the embrittlement effect of hydrogen in an FCC metal of Ni. The thermodynamic limits of fast and slow fractures are considered. The reduction of work of separation for different grain boundaries due to hydrogen segregation is systematically evaluated. It is shown that the embrittlement effect by hydrogen on grain boundaries is limited; the slower the fracture process, the more significant the embrittlement effect will be. A simple kinetic analysis of hydrogen diffusion versus crack velocity shows that most fractures in reality should be close to the fast fracture limit.

We use the deltahedral packing units to characterize the atomic structures of grain boundaries. The center of each deltahedron is considered as a stable interstitial site for hydrogen adsorption. Basing on the local electron density approximation, we assume that the same deltahedron always has similar adsorption and segregation energies, no matter what type of grain boundary it belongs to. Hence, one can calculate the reduction of separation energy of a grain boundary by a simple analysis of its constitute deltahedrons and their accumulative weakening effects associated with hydrogen adsorption. The accuracy of such approximation has been verified.

The hydrogen embrittlement of grain boundaries may cause the transition of the failure mode from the ductile intergranular to brittle transgranular fracture. Such transition has been observed in experiments by Bechtle et al. [2]. The fracture mode is known to be governed by the competitions between the energy release rates and associated resistance (e.g., work of separation). Our study reveals the controlling factors of the fracture mode transition: the first is the valve effect of the plastic work on fracture that depends exponentially on the local stress at a crack tip, and the second is the geometric effect on the driving force of fracture that depends largely on the local geometry of the crack tip. In short, the first effect changes the work of separation, while the second influences the energy release rate.

10.1.2 Recommendations for future research

In reality, the hydrogen embrittlement problem is more complicated than what has been considered in this study. Results from atomistic modeling are important and necessary but cannot provide a complete solution. While the atomistic study is essential to discovering the nanoscale mechanisms, atomistically-informed finite element simulations are suggested in the future research. This will enable the modeling study on the time and length scales of experiments with retaining the atomic-scale fidelity. Specifically, the atomistically determined material rate parameters could be combined with the front-tracking finite element method (ft-FEM) [3-6] to simulate crack initiation and growth using the experimental geometries. A brief summary of the key elements of ft-FEM is as follows and can be divided into three steps: Suppose the crack-tip shape at time *t* is known, the first step is to determine the equilibrium stress distribution caused by the hydrogen diffusion and redistribution. Then, use the advancing front method [7] to generate the mesh and use the standard finite element method to solve the equilibrium stress distribution. Next, the material addition/loss due to hydrogen diffusion from the notch surface is determined at time $t + \Delta t$ based on the kinetic rate of stress-assisted hydrogen embrittlement. Finally, the References configuration is updated and a new hydrogen distribution is calculated for time $t + \Delta t$. The computation is repeated to determine the time evolution of the crack tip morphology and location. The ft-FEM has been used for simulating crack growth due to stress corrosion [5]. It well captured the mechanisms of stable notch-like growth, blunting, and unstable notch-tip sharpening, etc. Taking those simulations as a References, the study is suggested to focus on improving the electrochemical accuracy by incorporating molecular modeling results, and also by quantitative comparison with experimental measurements, e.g., the rate of crack initiation and growth at different mechanical and charging loads.

Additionally, it is necessary to extend the present coupled atomistic and thermodynamic model to address the coupling effects of hydrogen affected plasticity and decohesion for realistic 3D crack geometries on the time scale relevant to laboratory experiments [8-11]. In a real hydrogen embrittlement problem, grain boundaries are distributed in a three dimensional system with defects. Distributions of grain boundaries, grain size and defects all matter. The finite element method with cohesive elements can be utilized to study those problems for predicting the fracture mode and material behavior.

10.2 Failure mechanisms of lithiated anode materials

10.2.1 Summaries

10.2.1.1 Chapter 4

Chapter 4 presents a model of the nanoscale fracture processes in silicon, which is being intensively studied as an anode material for lithium-ion battery. Competing fracture mechanisms at a crack tip are revealed, including cleavage bond breaking, dislocation emission and amorphization by the formation of five- and seven-membered rings. We find the strain-controlled fracture depends sensitively on system size, leading to an intriguing scenario of kinetically delayed fracture with reduced system size. Moreover, the lattice trapping effect enables us to perform an atomistic analysis of the geometry and energetics of competing crack-tip processes. We demonstrate that amorphization by single bond rotation is the most favorable atomic process until the athermal limit, implying that the brittle-to-ductile transition is less likely. Further, it should be noted that at elevated temperatures, all the three crack extension mechanisms may be active, leading to a complicated, coupled crack extension process.

10.2.1.2 Chapter 5

Similar to silicon, the fracture of a monolayer graphene can involve an alternating sequence of bond rotation and bond breaking under the quasi-static loadings around the Griffith limit of fracture. Such a fracture mode is kinetically preferred. Revealing the dislocation-mediated fracture mechanism provides insights regarding how to control the fracture in monolayer graphene for guided crack propagation.

In addition to the study of fracture mechanisms, we determine the critical condition to avert fracture by tailoring the system size. Under certain conditions, the energy release rate of fracture can be proportional to system size. A relation between the applied strain and system size is given on the critical condition when extension of a crack is thermodynamically unfavorable. Our theoretical derivation is verified by atomistic simulation of a modeling material of graphene. Additionally, this work is useful for the band-gap engineering of graphene. Both the sample size and applied strain are considered as control parameters for tuning the electrical properties of graphene. The critical condition given here is the limit of tuning band-gap in term of averting fracture.

10.2.1.3 Chapter 6

In chapter 6, the lithiation induced strain (LIS) in amorphous silicon is studied by atomistic simulations. Both the volume expansion and voltage are calculated as a function of Li composition, and further compared with experimental results. A nonlinear relation between the partial molar volume and lithium concentration is found and explained basing on the analysis of ring structures and charge transfer. Two stages of llithiation behavior are identified that can be separated by the lithium fraction x=0.8. When x<0.8, inserted Li atoms fill in the open space (interstitial sites) of silicon networks. This yields large adsorption energy, high voltage and small partial molar volume. When, x>0.8, interstitial sites are filled such that lithium insertion will cause bond breaking and network reconstruction. This leads to small adsorption energy, low voltage and large volume expansion.

While the interstitial sites may play an important role in the volume and voltage changes during lithiation, the rate of Li diffusion is likely to be governed by the shallow sites with low activation barriers between neighboring shallow ones and by their percolation in the disordered network structure of silicon. Our detailed analysis reinforces the notion that the Li-Si alloying behavior and associated properties, including the network topology characteristics of ring statistics, are sensitive to the local Li concentration. The work has implications for reducing the stresses and thereby improving the reversibility of charging and discharging by controlling the extent of lithiation.

10.2.1.4 Chapter 7

Chapter 7 presents a continuum modeling framework of lithiation of nanoparticle and nanowire. Motivated by experiment observations, we describe the two phases (lithium-rich and lithium poor phases) by using a free energy from the well-known regular solution model. Basing on this free energy, a non-linear diffusivity model is derived. Diffusion and associated deformation are simulated using the finite element method. The key finding is that material at outer layers of nanoparticles and nanowires will experience compressive elastic unloading, tensile elastic loading and tensile plastic yielding, all occurring in a single lithiation process. These results are consistent with *in situ* experiment observations.

Our model is different from previous studies [12-14], in which crack can only form in the center of material during lithiation. This difference is because they either do not model the two-phase coexistence or do not consider the plastic behavior of lithiated silicon undergoing large strain. It has been shown in chapter 8 that the kinetic process of lithiation in silicon is reaction-front controlled and the two–phase coexistence is a common feature, in contrast to the model of continuous concentration distribution of lithium. Meanwhile, the tensile stress achieved in front of the reaction front is only around one third of that in the outer layers. Since the surface is more prone to defect nucleation, it is conceivable that fracture will typically initiate from the surface during lithiation. More importantly, our modeling predictions are consistent with in situ TEM observations that fracture begins from surface during lithiation (see details in chapter 8 and 9).

10.2.1.5 Chapter 8

The effect of anisotropic expansion and anisotropic diffusion is studied in silicon nanowire during lithium insertion. Interestingly, a dumbbell-shaped nanowire cross section is found by *in situ* lithiation experiments, which involves necking and cracking instabilities. Basing on the finite element simulation (chapter 7), this dumbbell shape is exactly predicted and is explained in our anisotropic model for silicon lithiation. Despite extensive plastic flow of the lithiation product, very large stresses nonetheless develop inside the nanowire, leading to cracking or even self-splitting of the single nanowire into two sub-wires. This unusual morphological evolution is dependent on the electrochemical driving force for lithiation.

Lastly, this system exhibits linear kinetics during initial lithiation, in sharp contrast to the parabolic lithiation kinetics observed in SnO_2 nanowires, suggesting that the lithiation reaction in this system is controlled by the reaction front but not limited by the long-range diffusion of Li ions. The speed of migration of reaction front is measured. The front migration distance L is found to be approximately linear with respect to the reaction time $L \propto t$, indicating the kinetics of lithiation is likely controlled by the short-range processes near the reaction front (e.g., interfacial diffusion, reaction, and plastic flow), rather than by the long range diffusive transport along the wire. In the meantime, the concentration of lithium along the silicon is also examined. The electron diffraction pattern (EDP) from the lithiated segment of the nanowire confirmed the formation of a polycrystalline $Li_{15}Si_4$ (c-$Li_{15}Si_4$) phase mixed with amorphous Li_xSi (a-Li_xSi), consistent with previous reports. These

two observations lend a direct support to our assumption made in chapter 7 that lithiation is a reaction front-controlled process with two-phase coexistence.

10.2.1.6 Chapter 9

To better control the lithiation induced strain (LIS) and improve the cyclic performance of lithium ion battery, we study the nanowire electrodes with carbon and metal coatings. Dramatic effects of coatings on the lithiation behavior of individual SnO_2 nanowires are demonstrated by experiments. Compared to the non-coated case, the coated SnO_2 nanowires can be charged at a rate ten times higher than that of the uncoated one due to the improved electronic conductivity. More importantly, radial expansion is completely suppressed in the coated nanowires due to the mechanical confinement of the coating layers. This study demonstrated that it is possible to simultaneously control the electrochemical reaction rate and the mechanical strain of the electrode materials through carbon or aluminum coating, opening new avenues of designing better lithium ion batteries.

10.2.2 Recommendations for future research

One important objective in the current research of lithiation induced strain is to prevent the cyclic fading of capacity, which is often caused by mechanical failures. We ask whether it is possible to take the advantage of high capacity while control the lithiation induced strain at the same time. This requires a deeper understanding of lithiation behaviors, especially under large stress and strain. Since both plastic flow and surface response can play critical roles in the fracture of nanostructured electrode materials, it is necessary to compute the plastic yielding properties and surface energy of anode material, which provide a basis of predicting the failures of anode material during lithiation and delithiation cycles.

In addition to material properties, failure mechanisms of anode are also unknown. Both cavitation and fracture are observed recently. But the underlying mechanisms are still not well understood. In chapter 6 we show that the brittle and ductile fracture responses are dependent on the nature of atomic bonding, i.e., ceramic versus metallic, and covalent versus ionic. Furthermore,

the failure mode, including fracture, fatigue and creep, may be significant at difference stages during cycles of charging and discharging. The in situ TEM experiment is a powerful means of finding when, where and how failure happens. But it also has its own limitation. If failure happens slowly or after a number of charging-discharging cycles, in situ TEM may not be able to capture it due to the time scale limitation. Then, other ex situ measurements and atomistic modeling will be helpful. In addition, the phenomenon of electrical-chemically driven solid state amorphization is little studied at the nanoscale [15, 16], despite the related continuum models [17-19] as well as earlier works by the amorphous metal community [20]. The process of solid state amorphization of silicon is only conceptually understood. In future research, quantitative studies are recommended.

Finding the high capacity electrode materials, including alloys and nanostructured materials [15, 21, 22], is necessary and important to build better lithium ion battery. Researches on germanium and tin-based materials are recommended [23]. Although silicon has great capacity and relatively cheap, its LIS and conductivity are poor. A promising route is to use the silicon alloys with reduced LIS and enhanced conductivity. Meanwhile, nanostructured materials should be further explored, such as nanotube, coated nanowire and nanosponge with high porosity [13]. Geometrically designed composite nanostructures could provide confinement on deformations while promote conductivity at the same time. However, they may also generate other mechanical problems, such as mismatch strain between different components during lithiation or delithiation. Further study of those aspects is required.

As a relatively new research area, many puzzles and unknowns need to be resolved for building better lithium ion battery. Accurate measurements and in situ experiments, integrated with mechanistic modeling, are essential to advance our fundamental understanding of the electro-chemical-mechanical behaviors of battery materials.

References

1. Rice, J.R. and J.S. Wang, *EMBRITTLEMENT OF INTERFACES BY SOLUTE SEGREGATION.* Materials Science and Engineering a-Structural Materials Properties Microstructure and Processing, 1989. 107: p. 23-40.
2. Bechtle, S., et al., *Grain-boundary engineering markedly reduces susceptibility to intergranular hydrogen embrittlement in metallic materials.* Acta Materialia, 2009. 57(14): p. 4148-4157.
3. Hillig, W.B. and R.J. Charles, *Surfaces, stress-dependent surface reactions, and strengths*, in *High-Strength Materials*, V.F. Zackay, Editor. 1964, Wiley, New York. p. 682-705.
4. Chuang, T.J. and E.R. Fuller, *Extended Charles-Hillig Theory For Stress-Corrosion Cracking Of Glass.* Journal Of The American Ceramic Society, 1992. 75(3): p. 540-545.
5. Tang, Z., A.F. Bower, and T.J. Chuang, *Numerical simulations of the growth and deflection of a stress-corrosion notch on the interface between two reactive solids.* International Journal Of Fracture, 2004. 127(1): p. 1-20.
6. Rice, J.R. and T.J. Chuang, *Energy Variations in Diffusive Cavity Growth.* Journal of the American Ceramic Society, 1981. 64(1): p. 46-53.
7. Peraire, J., et al., *Adaptive Remeshing for Compressible Flow Computations.* Journal of Computational Physics, 1987. 72(2): p. 449-466.
8. Zhu, T., J. Li, and S. Yip, *Atomistic study of dislocation loop emission from a crack tip.* Physical Review Letters, 2004. 93: p. 025503.
9. Zhu, T., J. Li, and S. Yip, *Atomistic configurations and energetics of crack extension in silicon.* Physical Review Letters, 2004. 93: p. 205504.
10. Warner, D.H., W.A. Curtin, and S. Qu, *Rate dependence of crack-tip processes predicts twinning trends in f.c.c. metals.* Nature Materials, 2007. 6: p. 876–881.
11. Song, J., M. Soare, and W.A. Curtin, *Testing continuum concepts for hydrogen embrittlement in metals using atomistics.* 2009, submitted.
12. Cheng, Y.T. and M.W. Verbrugge, *Evolution of stress within a spherical insertion electrode particle under potentiostatic and galvanostatic operation.* Journal of Power Sources, 2009. 190(2): p. 453-460.
13. Gao, Y.F. and M. Zhou, *Strong stress-enhanced diffusion in amorphous lithium alloy nanowire electrodes.* Journal of Applied Physics, 2011. 109(1).
14. Zhao, K.J., et al., *Inelastic hosts as electrodes for high-capacity lithium-ion batteries.* Journal of Applied Physics, 2011. 109(1).
15. Chan, C.K., et al., *High-performance lithium battery anodes using silicon nanowires.* Nature Nanotechnology, 2008. 3(1): p. 31-35.
16. Huang, R. and J. Zhu, *Silicon nanowire array films as advanced anode materials for lithium-ion batteries.* Materials Chemistry and Physics, 2010. 121(3): p. 519-522.
17. Meethong, N., et al., *Electrochemically Induced Phase Transformation in Nanoscale Olivines Li1-xMPO4 (M = Fe, Mn).* Chemistry of Materials, 2008. 20(19): p. 6189-6198.

18. **Tang, M., W.C. Carter, and Y.M. Chiang, *Electrochemically Driven Phase Transitions in Insertion Electrodes or Lithium-Ion Batteries: Examples in Lithium Metal Phosphate Olivines.* Annual Review of Materials Research, Vol 40, 2010. 40: p. 501-529.**

19. **Tang, M., et al., *Model for the Particle Size, Overpotential, and Strain Dependence of Phase Transition Pathways in Storage Electrodes: Application to Nanoscale Olivines.* Chemistry of Materials, 2009. 21(8): p. 1557-1571.**

20. **Schwarz, R.B. and W.L. Johnson, *Formation of an Amorphous Alloy by Solid-State Reaction of the Pure Polycrystalline Metals.* Physical Review Letters, 1983. 51(5): p. 415-418.**

21. **Chevrier, V.L. and J.R. Dahn, *First Principles Studies of Disordered Lithiated Silicon.* Journal of the Electrochemical Society, 2010. 157(4): p. A392-A398.**

22. **Chevrier, V.L., J.W. Zwanziger, and J.R. Dahn, *First principles studies of silicon as a negative electrode material for lithium-ion batteries.* Canadian Journal of Physics, 2009. 87(6): p. 625-632.**

23. **Beaulieu, L.Y., et al., *Reaction of Li with alloy thin films studied by in situ AFM.* Journal of the Electrochemical Society, 2003. 150(11): p. A1457-A1464.**